

AN ABSTRACT OF THE DISSERTATION OF

Thomas V. Holschuh for the degree of Doctor of Philosophy in Nuclear Engineering
presented on June 16, 2017.

Title: Quantification of Reactor Kinetics Parameters during Reactor Transients using Cherenkov Light and Auxiliary Application to Nuclear Safeguards

Abstract approved: _____

Wade R. Marcum

The International Atomic Energy Agency (IAEA) is the leading organization for monitoring nuclear facilities worldwide, and the Agency's methods are constantly developing and improving in an effort to more effectively safeguard nuclear material. As such, the IAEA addresses near and long term risks in order to advance the capabilities of the IAEA inspectors to identify quantities of diverted material, known as defects. Advanced techniques enable the inspectors to decrease the uncertainty in measurements, which translates to smaller detectable defects. Recently, digital-imaging techniques for qualitative inspections of irradiated fuel using Cherenkov light measurements have advanced the Agency's ability to perform verification measurements following discharge of the fuel from power reactor facilities. However, one area that continues to be difficult for the IAEA is the non-invasive, in-core inspection of research reactors with the objective of verifying the quantity of fissile isotopes. Current techniques do not quantify the relative fissile material content and cannot characterize a reactor during operations, limiting their value for safeguards and nuclear material accountancy. Research reactors are typically smaller in size than power reactors, so identifying defects is innately more difficult. This study seeks to leverage existing optical measurement technology by assembling a new detecting method, the Cherenkov Radiation Assay for Nuclear Kinetics (CRANK) system, to identify and characterize Cherenkov light in an operating research reactor and to relate this signature to the quantity of fissile material in the reactor.

©Copyright by Thomas V. Holschuh

June 16, 2017

All Rights Reserved

Quantification of Reactor Kinetics Parameters during Reactor Transients using
Cherenkov Light and Auxiliary Application to Nuclear Safeguards

by
Thomas V. Holschuh

A DISSERTATION
submitted to
Oregon State University

in partial fulfillment of
the requirements for the
degree of
Doctor of Philosophy

Presented June 16, 2017
Commencement June 2018

Doctor of Philosophy dissertation of Thomas V. Holschuh presented on June 16, 2017

APPROVED:

Major Professor, representing Nuclear Engineering

Head of the School of Nuclear Science and Engineering

Dean of the Graduate School

I understand that my dissertation will become part of the permanent collection of Oregon State University libraries. My signature below authorizes release of my dissertation to any reader upon request.

Thomas V. Holschuh, Author

ACKNOWLEDGEMENTS

I'd like to thank everyone who has positively influenced my college career at Oregon State. I spent all my collegiate life at OSU and have never regretted my choice.

I'd like to sincerely thank my advisor, Dr. Wade Marcum, who employed me in his research group since my third year of undergrad and allowed me to transition smoothly to projects that captured my interest. He provided me with direction when I needed it as well as research options to allow me to determine my own course.

Many individuals have provided valuable additions to my dissertation research, including staff members at INL and faculty at OSU, and I'd like to thank them for the help because it was desperately needed at times. I'd also like to express gratitude to the reactor operating staff for graciously fitting my experiments into the OSTR's busy schedule.

Interactions with all undergraduate and graduate students in the OSU NSE department were beneficial in my collegiate education, but, in particular, I'd like to thank Trevor Howard, Aaron Weiss, Griffen Latimer, and Chad Nixon for allowing me to double-check numerous bad ideas with them in regards to my research, only a few of which turned out to be decent enough to pursue.

Finally, I'd like to thank my parents, Dawn and Tom, who were supportive of my interests in math and science throughout my life and viewed the pursuit of nuclear engineering, beginning with my high school internship at Sandia, as a worthwhile endeavor for my life.

TABLE OF CONTENTS

<u>Section</u>	<u>Page</u>
1 INTRODUCTION	1
1.1 Motivation	2
1.2 Objectives.....	4
1.3 Overview of Following Chapters	4
2 SURVEY OF LITERATURE.....	6
2.1 Current Safeguards Efforts.....	7
2.1.1 Nondestructive Assay Using Neutrons	10
2.1.2 Nondestructive Assay Using Photons.....	11
2.1.3 Nondestructive Assay Using Antineutrinos.....	12
2.1.4 Nondestructive Assay Using Cherenkov Light.....	13
2.1.5 Nondestructive Assay Conclusions.....	16
2.2 Methods for Determination of Reactor Kinetics Parameters	19
2.2.1 Statistical Methods.....	19
2.2.2 Computational Methods.....	21
2.2.3 Reactor Kinetics Determination Conclusions	22
2.2.4 Conclusions for Reactor Kinetics Parameters Methods.....	25
3 THEORY	26
3.1 Cherenkov Physics	26
3.1.1 Mechanism of Light Production	28
3.1.2 Computational Tools for Cherenkov Light.....	31
3.2 Reactor Kinetics	33
3.2.1 Mathematical Models of Reactor Kinetics	34

TABLE OF CONTENTS (CONTINUED)

<u>Section</u>		<u>Page</u>
3.2.2	Numerical Solutions to PRKEs.....	36
3.2.3	Reactor Pulses.....	39
3.2.4	Reactor Square Waves	46
3.2.5	Reactor Kinetics Conclusions	48
4	INSTRUMENTATION	49
4.1	Oregon State TRIGA Reactor	49
4.2	Photodiodes	53
4.3	Fiber Bundle	56
4.4	Optical Lens	59
4.5	Data Acquisition System.....	61
4.6	Programmable Light Source.....	63
4.7	Instrumentation Conclusions.....	64
5	EXPERIMENTAL METHODS.....	68
5.1	Desktop Experiments	68
5.2	OSTR Experiments	71
6	RESULTS AND OBSERVATIONS	74
6.1	Desktop Experiments	74
6.1.1	Background Light Contamination.....	74
6.1.2	Angular Offset and Stand-off Distance.....	75
6.1.3	Simulations	79
6.1.4	Transient Testing with Desktop Experiments – Square Waves.....	81

TABLE OF CONTENTS (CONTINUED)

<u>Section</u>	<u>Page</u>
6.1.5 Transient Testing with Desktop Experiments – Reactor Pulses	84
6.1.6 Desktop Experiment Conclusions.....	88
6.2 OSTR Experiments	89
6.2.1 Square Waves.....	90
6.2.2 Reactor Pulses.....	92
6.2.3 Simulations	114
6.2.4 OSTR Conclusions.....	118
7 PROLIFERATION RESISTANCE	120
7.1 Case Study – OSTR.....	124
7.2 Proliferation Resistance Summary	126
8 CONCLUSIONS.....	128
8.1 Observations.....	128
8.2 Relevance of Work.....	129
8.3 Assumptions and Limitations.....	129
8.3.1 Reactor Type	129
8.3.2 Reactivity Limitations.....	130
8.4 Future Work	130
9 BIBLIOGRAPHY	132
10 NOMENCLATURE	143
11 APPENDIX A – PD EVALUATION.....	147
12 APPENDIX B – COMPLETE ASSESSMENT OF OSTR TRANSIENTS.....	156

TABLE OF CONTENTS (CONTINUED)

<u>Section</u>	<u>Page</u>
12.2 Square Waves	156
12.3 Reactor pulses.....	161
13 APPENDIX C – SENSITIVITY ANALYSIS	
13.1 β/l Ratio	171
13.2 Proliferation Resistance	172

LIST OF FIGURES

<u>Figure</u>	<u>Page</u>
Figure 2-1: Nuclear nondestructive assay techniques.....	10
Figure 3-1: Polarization induced by a charged particle moving through matter	27
Figure 3-2. Cherenkov light intensity as a function of wavelength.....	30
Figure 3-3. View of OSTR at steady power of 1 MW.....	31
Figure 3-4: Sample Cherenkov photon yield utilized in MCNP6.	32
Figure 3-5. Comparison of PRKE solutions and FN models.....	41
Figure 3-6. Comparison of \$0.50 reactivity insertion for U-235 and Pu-239.....	47
Figure 4-1. Vertical Section of OSTR	50
Figure 4-2. OSTR Core and Adjacent Equipment	51
Figure 4-3: PDA25K GaP Photodiode.....	54
Figure 4-4. Comparison of PD Responsivity and Cherenkov spectrum.....	55
Figure 4-5. Thorlabs BF20HSMA01 fiber bundle.....	57
Figure 4-6. Thorlabs BF20HSMA01 fiber design with 7 separate fibers.....	57
Figure 4-7. Multimode Fiber Attenuation for Thorlabs BF20HSMA01	58
Figure 4-8. Thorlabs F810SMA-543 collimator.....	59
Figure 4-9. Ocean Optics COL-UV-30 collimating lens.....	60
Figure 4-10. Transmission percentage of N-SF6 and Suprasil glass	61
Figure 4-11. NI PXIe-5171R digital oscilloscope	62

LIST OF FIGURES (CONTINUED)

<u>Figure</u>	<u>Page</u>
Figure 4-12. NI PXIe-1085 chassis with sample modules.....	63
Figure 4-13. Comparison of PD, LED, and Cherenkov spectrums	64
Figure 4-14. Layout of CRANK system components.....	65
Figure 4-15. Horizontal section view of CRANK system setup at OSTR.....	66
Figure 4-16. Vertical section view of CRANK system setup at OSTR.....	67
Figure 5-1. PDA25K response to steady state current with error bars	69
Figure 5-2. M365FP1 output as function of supplied current.....	70
Figure 5-3. PDA25K response as a function of M365FP1 light intensity	71
Figure 6-1. Enclosure box for preliminary desktop experiments	75
Figure 6-2. Depiction of positioning scheme representing stand-off distance.	76
Figure 6-3. PDA25K response at 0 dB at steady light intensity for select positions..	77
Figure 6-4. Contour plot for normalized photodiode response.....	78
Figure 6-5. Normalized PD response with associated uncertainty (A-D)	79
Figure 6-6. Contour plot for normalized MCNP photon transport	80
Figure 6-7. Response of PD to square waves with different \$ values.	82
Figure 6-8. Response of PD to reactor pulses with different \$ values.....	85
Figure 6-9. Detailed view of PD response from Figure 6-8	87
Figure 6-10. PD response from \$0.80 square wave (SQ-10).....	91

LIST OF FIGURES (CONTINUED)

<u>Figure</u>	<u>Page</u>
Figure 6-11. Percent experimental uncertainty in β/l ratio using (3-35) (2σ).....	94
Figure 6-12. OSTR core excess over one month period.....	95
Figure 6-13. OSTR core excess over a one week period.....	96
Figure 6-14. Taylor expansion of FN model	99
Figure 6-15. Second and fourth order polynomial fits of P-29 near pulse peak.....	100
Figure 6-16. Comparison of P-22, P-23, and corresponding FN model	101
Figure 6-17. Comparison of P-18, P-19, and P-20 measurements.....	102
Figure 6-18. Comparison of P-22, P-23, P-24, and P-25 measurements	102
Figure 6-19. Comparison of P-26, P-27, and P-28 measurements.....	104
Figure 6-20. Comparison of P-29, P-30, and P-31 measurements.....	104
Figure 6-21. Comparison of Monday and Wednesday pulse measurements.....	106
Figure 6-22. \$2.00 pulse comparison with OSTR BOL uncertainty	107
Figure 6-23. \$2.00 pulse comparison with varying core lifetime	108
Figure 6-24. Calculation of β/l ratio with X2, Y1 pulse comparisons	109
Figure 6-25. Calculation of β/l ratio with X1, Y2 pulse comparisons	110
Figure 6-26. Calculation of β/l ratio with X2, Y2 pulse comparisons	110
Figure 6-27. Calculation of β/l ratio with X1, Y1 pulse comparisons	111
Figure 6-28. Calculation of β/l ratio with selected X1, Y1 pulse comparisons	112

LIST OF FIGURES (CONTINUED)

<u>Figure</u>	<u>Page</u>
Figure 6-29. Calculation of β/l and uncertainty with varying sample rate	113
Figure 6-30. Cherenkov photon tally in OSTR at lens position	114
Figure 7-1. CRANK System Detection Methodology	127
Figure 11-1. Calibration curve for TRIGA-like light intensities	147
Figure 11-2. Signal to Noise curve for TRIGA-like light intensities	148
Figure 11-3. PD response curve with varying LED optical power.....	148
Figure 11-4. PD response as a function of LED supplied current – 0 dB.....	149
Figure 11-5. PD response as a function of LED supplied current – 10 dB.....	150
Figure 11-6. PD response as a function of LED supplied current – 20 dB.....	150
Figure 11-7. PD response as a function of LED supplied current – 30 dB.....	151
Figure 11-8. PD response as a function of LED supplied current – 40 dB.....	151
Figure 11-9. PD response as a function of LED supplied current – 50 dB.....	152
Figure 11-10. PD response as a function of LED supplied current – 60 dB.....	152
Figure 11-11. Normalized PD response with associated uncertainty (E-H)	153
Figure 11-12. Normalized PD response with associated uncertainty (I-K)	154
Figure 11-13. Normalized PD response with associated uncertainty (AA-DD).....	154
Figure 11-14. Normalized PD response with associated uncertainty (EE-GG).....	155
Figure 12-1. Comparison of SQ-1 and SQ-2 measurements	158

LIST OF FIGURES (CONTINUED)

<u>Figure</u>	<u>Page</u>
Figure 12-2. Comparison of SQ-3 and SQ-4 measurements	159
Figure 12-3. Comparison of SQ-5, SQ-6, and SQ-7 measurements	159
Figure 12-4. Comparison of SQ-8 and SQ-9 measurements	160
Figure 12-5. Comparison of SQ-10 and SQ-11 measurements	160
Figure 12-6. Comparison of P-1 and P-2 measurements	163
Figure 12-7. Comparison of P-3 and P-4 measurements	164
Figure 12-8. Comparison of P-5, P-6, and P-7 measurements.....	164
Figure 12-9. Comparison of P-8, P-9, and P-10 measurements.....	165
Figure 12-10. Comparison of P-11, P-12, and P-13 measurements.....	166
Figure 12-11. Comparison of P-14, P-15, P-16, P-17, and P-21 measurements	166
Figure 12-12. β/l ratio measurement using FN model	167
Figure 12-13. β/l ratio measurement using 2 nd order polynomial	168
Figure 12-14. First derivative of P-12, P-13, and FN models.....	169
Figure 12-15. Block diagram of NI LabVIEW VI used for OSTR experiments	170
Figure 12-16. Front panel of NI LabVIEW VI used for OSTR Experiments.....	170

LIST OF TABLES

<u>Table</u>	<u>Page</u>
Table 2-1. Survey of Literature Summary for NDA.....	18
Table 2-2. Calculated Reactor Kinetics Survey.....	24
Table 3-1. Reactor Kinetics Parameters for OSTR LEU Core	38
Table 3-2. Calculated β/l ratios for theoretical and numerical models	43
Table 3-3. Calculated β/l ratios for modified theoretical and numerical models.....	45
Table 4-1. List of CRANK System Components and Functions	49
Table 4-2. Associated Uncertainty in β/l ratio	52
Table 4-3. Comparison of PD and PMT characteristics	54
Table 4-4. PDA25K Gain Specifications.....	56
Table 4-5. Characteristics of Thorlabs BF20HSMA01 fiber bundle	58
Table 4-6. Comparison of FOV for Thorlabs collimator and Ocean Optics lens	61
Table 6-1. Reactor kinetics values for PJ approximations from Figure 6-7	83
Table 6-2. Calculated β/l ratios for FN model and simulated reactor pulses.....	88
Table 6-3. Calculated β/l ratios for modified FN model and simulated pulses	88
Table 6-4. Record of reactor pulses with sufficient data for analysis.....	93
Table 6-5. Record of reactor pulses based on reactivity insertion and core excess....	97
Table 6-6. Calculated β/l ratio for pulses in Figure 6-28.....	112
Table 6-7. MCNP Cherenkov tally and conversion factors	116

LIST OF TABLES (CONTINUED)

<u>Table</u>	<u>Page</u>
Table 6-8. Instrumentation attenuation factors	117
Table 6-9. PD conversion factors.....	118
Table 7-1. OSTR Fuel Rod Properties.....	125
Table 7-2. Detectable Limit using P-29 and P-30.....	126
Table B-1. Record of square waves performed at OSTR	157
Table B-2. Record of reactor pulses without sufficient data for analysis.....	161

Quantification of Reactor Kinetics Parameters during Reactor Transients using Cherenkov Light and Auxiliary Application to Nuclear Safeguards

1 INTRODUCTION

The implications of uncontrolled nuclear materials located throughout the world have been identified by the International Atomic Energy Agency (IAEA and also known as the Agency) as a topic of interest and focus regarding nuclear proliferation [1, 2]. The IAEA is the leading organization for monitoring nuclear facilities worldwide, and the Agency's methods are constantly developing and improving in an effort to more effectively safeguard nuclear material. As such, the IAEA addresses near- and long-term risks in order to advance the capabilities of the IAEA inspectors to determine if declared materials have been diverted, which is called a material 'defect'. Advanced inspection techniques enable the inspectors to decrease the uncertainty in their measurements, which translates to the quantification of smaller defects. However, one area that continues to cause difficulties for the IAEA is the non-invasive inspection of research reactors with the objective of identifying the quantity of fissile materials in such facilities. Research reactors necessitate regular inspections by the IAEA driven by historical events in which research applications may be used to develop a full-scale program in a country with aspirations of developing nuclear weapons. For example, a detailed explanation of IAEA safeguards efforts in North Korea is presented by Albright [3] and emphasizes the importance of maintaining safeguards on research reactors since North Korea's initial efforts in plutonium production were facilitated in research reactors, with an estimate for total produced quantities provided by Dreicer [4].

Recently, techniques for qualitative inspections of spent fuel using Cherenkov radiation, or Cherenkov light, have advanced the Agency's ability to perform defect verification measurements following discharge of the fuel from the reactor [5]. Unfortunately, these measurements are limited in their value for safeguards and nuclear material accountancy, since they do not quantify the fissile material quantities and cannot characterize a reactor during operations. Additionally, these methods are

primarily intended for power reactor facilities; in comparison, research reactors are typically smaller in size than power reactors, so identifying defects is innately more difficult.

Theoretically, the dynamic material signatures of fissile isotopes, such as uranium and plutonium, in a reactor facilitate the identification of the fuel mixture composition through reactor kinetics parameters. In this approach, when a nuclear reactor is perturbed from a steady-state condition, the response of the reactor is indicative of the effective kinetics parameters inherent to the system. If quantities such as thermal power are measured directly (or indirectly) during these transients, the kinetics parameters may be quantified. Using the knowledge that the intensity of Cherenkov light emitted from a reactor is linearly proportional to changes in the reactor's power, it may be possible to identify specific fuel signatures in the reactor by measurements of this light. A process is outlined herein which details the method used, hardware selected, and configuration identified that was used to prove the concept. The outcome of this work is the design and implementation of a detecting system that quantifies material signatures in research reactors by performing non-invasive, in-core measurements of (Cherenkov) light that such a facility emits.

1.1 Motivation

The IAEA is committed to providing effective safeguards measurements, and the application of nascent technologies to expand the scope of measurements will provide the staff of inspectors with a larger array of inspection tools. However, most safeguards techniques are applicable only after nuclear material is located in a spent fuel pool or otherwise discharged from operation, and very few techniques are capable of determining illicit material production, or its resulting change in kinetics parameters, during reactor operations.

A research reactor comprises a smaller reactor core than traditional power reactors, so the introduction of bias defects, or small changes in fissile material inventory, during

reactor operations has a larger influence on reactor power. In addition, since reactor power during a transient is a function of neutron kinetics parameters, the measurement of Cherenkov light during this transient indicates the values of the kinetics parameters. In this perturbed state, the point reactor kinetics equations (PRKEs) model the reactor response. These equations are dependent on the kinetics parameters of the reactor [6], which may be inferred from the light intensity measurement as a function of time.

Previous work by Arkani and Gharib [7] has shown that the intensity of Cherenkov light in a reactor is linear with respect to reactor power, though the conversion from the value of light intensity to thermal reactor power in watts can be difficult since the reactor's core and structural geometry can vary from site to site. However, if a prompt perturbation in reactivity is introduced to the reactor, the ratio of light intensities from the initial state to the perturbed state may be used to determine the ratio of reactor power from the initial state to the perturbed state. A light-sensitive detector, such as a photomultiplier tube or photodiode, measuring the flux of Cherenkov light photons in a reactor during the power perturbation can be used to determine reactor kinetics parameters, such as the delayed neutron fraction and prompt neutron lifetime, based on theoretical relationships of the reactor transient. The use of Cherenkov light allows the method to be non-intrusive, a key quality for novel safeguards technologies used by the IAEA, and minimal reliance is placed on facility operations during an inspection.

Cherenkov radiation was first explained in 1934 by Pavel Čerenkov [8] and exhibits a UV-visible wavelength spectrum in water, caused by particles traveling at a superluminal velocities through a dielectric medium. Cherenkov light in a spent fuel pool is produced by decay products (secondary electrons produced by gamma rays from the fuel and beta particles) passing through water within the reactor tank. The intensity of decay heat indicates burnup levels during its lifetime in a reactor core and the time elapsed since the fuel was placed in its present location. While other inspection tools

may be the most appropriate for use outside of reactor operations (i.e. spent fuel pool), however, it is of relevance to quantify defects during operation, which requires the design, and application of a new system.

1.2 Objectives

This study seeks to leverage existing technology by assembling a new detecting system to detect and characterize Cherenkov light and to relate its intensity signature to quantities of fissile material in a repeatable manner. The outcome of this work has yielded a detecting system that quantifies material signatures in research reactors from non-invasive, in-core measurements of the (Cherenkov) light that such a facility emits.

Using off-the-shelf components (including photodiodes and data acquisition system) assembled into a new detecting system, it has been shown one may accurately and independently measure the kinetics parameters quantified from the rate of change of intensity of Cherenkov light in an operating research reactor to determine the delayed neutron fraction and the prompt neutron lifetime based on a specified reactivity perturbation. The detection system is deemed the Cherenkov Radiation Assay for Nuclear Kinetics (CRANK) system, and will be referred to as such throughout this dissertation.

1.3 Overview of Following Chapters

In chapter two, a literature review is presented, providing a general understanding of previously implemented safeguards and previous applications of Cherenkov light in order to examine the potential connection between the two concepts. Additionally, the equations governing reactor kinetics are summarized, with a discussion of previous literature allowing these equations to be applied in this study.

In chapter three, the mechanism of Cherenkov light production and computational models is detailed, along with the point reactor kinetics model and its proposed connection to Cherenkov light. A prompt critical solution for the point reactor kinetics model is presented and particular aspects are highlighted to utilize Cherenkov light intensity in the determination of reactor kinetics parameters.

Chapter four presents a discussion of the experimental equipment and procedure for proving the hypothesis of this study.

In chapter five, the method for determining material diversion is investigated. The kinetics parameters differ for specific isotopes of uranium and plutonium, allowing for discrepancies in reactor response to a reactivity insertion to be analyzed.

In chapter six, results and observations from this study are presented. The results provide experimental data to support the hypothesis of this study and present a comparison of measured kinetics parameters to those declared in the Safety Analysis Report for the Oregon State TRIGA Reactor.

In chapter seven, the method is evaluated for proliferation resistance. In cases where material diversion may be of interest, the reactor core configuration will be altered, but detectability still exists with the CRANK system's method. A case study for the Oregon State TRIGA Reactor is provided.

Lastly, in chapter eight, the research goals are reiterated, with the experimental results provided again for comparison. The relevance and limitations of the CRANK system's method are discussed and any future work that could expand the applicability of the system in a nuclear nonproliferation program.

2 SURVEY OF LITERATURE

The hypothesized application of this research expands the capability of the IAEA to inspect research reactor facilities during normal operations as part of a safeguards regime. Therefore, it is prudent to summarize the safeguards goals of the IAEA and, consequently, review the current safeguards techniques in order to emphasize the significance of this study.

The IAEA Statute [9], which established the IAEA and came into force in 1957, contains a chapter regarding safeguards (Chapter XII) that states inspectors have the responsibility of ensuring compliance in a nuclear facility. The IAEA composes Information Circular (INFCIRC) documents that outline the objectives and limitations of safeguards efforts that may be implemented by the Agency.

In particular, INFCIRC/26 [10] introduced the safeguards regime to research reactors in 1961. Then, in 1965, INFCIRC/66 [11] directly addressed the circumstances that require safeguards. Each of these documents provided item-specific safeguards, applying to specific quantities of materials, rather than facility safeguards. Expansion of revisions to the IAEA's safeguards program occurred with INFCIRC/153 [12] to address the required structure and content of the agreements between the states and the Agency in connection to the Nuclear Nonproliferation Treaty (NPT). Numerous paragraphs within INFCIRC/153 focus on safeguards efforts specifically:

- Part II, paragraph 28: The objective of safeguards is the timely detection of diversion of significant quantities of nuclear material from peaceful nuclear activities to the manufacture of nuclear weapons or of other nuclear explosive devices or for purposes unknown, and deterrence of such diversion by the risk of early detection.
- Part I, paragraph 4: The Agreement should provide that safeguards shall be implemented in a manner designed:

- To avoid hampering the economic and technological development of the State or international co-operation in the field of peaceful nuclear activities, including international exchange of nuclear material;
 - To avoid undue interference in the State's peaceful nuclear activities, and in particular in the operation of facilities; and
 - To be consistent with prudent management practices required for the economic and safe conduct of nuclear activities.
- Part I, paragraph 6: The Agreement should provide that in implementing safeguards pursuant thereto the Agency shall take full account of technological developments in the field of safeguards.

IAEA inspectors are tasked with ensuring compliance with facilities governed by these sets of INFCIRCs. Non-compliance occurs in three varieties:

- Failure to declare material that is controlled by the IAEA,
- Failure to notify the Agency of material in facility under INFCIRC/153 agreement, and
- Failure to comply with binding agreements with the IAEA.

2.1 Current Safeguards Efforts

A comprehensive manual of safeguards techniques and equipment is provided by the IAEA [13], and describes destructive analysis, nondestructive analysis, unattended monitoring, containment and surveillance, remote monitoring, environmental sampling, newly developed, and developing techniques.

Destructive analysis or assay of samples has shown to be the most accurate, and therefore, effective way of determining isotope content, which often includes dissolving the sample in acid. The IAEA frequently performs destructive analysis to create reference standards through which other destructive or nondestructive analyses

may be compared to with an unknown sample when attempting to quantify isotopes of interest [14].

However, in an effort to support the statements of INFCIRC/153, it is more desirable for IAEA inspectors to attain measurements without disrupting normal operations or compromising material integrity, known as nondestructive assay (NDA). The goal of NDA, in support of INFCIRC/153, is the timely detection of diversion, and the staff of inspectors categorizes the diversion by the defect level. The timely detection of diversion is defined by the IAEA and varies based on the material of interest [15], and the three levels of defects used for NDA Instruments with example of defect level [16] are given as:

- Gross defect: Assembly missing or dummy substitute
- Partial defect: More than 50 percent of pins missing from spent fuel assembly
- Bias defect: Enrichment or weight discrepancy by small fraction in a given quantity of uranium or plutonium

The IAEA utilizes a combination of destructive assay (DA) and NDA techniques to achieve its mission, and each technique requires a defensible method of uncertainty quantification (UQ), and, “without UQ fit for purpose, physical measurements and calculations have no meaning” [17]. For each measurement, the associated uncertainty allows inspectors to assign a “confidence” when assessing spent nuclear fuel assemblies or other samples in question. DA requires the modification of a sample to match an analysis method, while NDA techniques are developed to use natural attributes of the sample to determine characteristics of the sample for nonproliferation purposes. The research performed for this dissertation is an NDA method, so the past and current safeguards efforts in DA techniques will not be discussed further.

The outcome of the CRANK system yields a new NDA safeguards technique to provide IAEA inspectors with a new tool in regards to research reactor inspections.

Therefore, it is relevant to discuss safeguards techniques under development as well as contemporary methods. Currently, many independent methods are being developed to provide independent measurements focused on a variety of phenomena with the objective of expanding the IAEA's capacity to provide complete facility inspections. In fact, the Next Generation Safeguards Initiative (NGSI) has expressed interest and provided resources in the research of fourteen key techniques based on the each method's promising progress and potential to provide additional, unique capabilities to the portfolio of IAEA safeguards techniques [18]:

- ^{252}Cf Interrogation with Prompt Neutron Detection,
- Delayed Gamma,
- Delayed Neutrons,
- Different Die-Away,
- Differential Die-Away Self-Interrogation,
- Lead Slowing Down Spectrometer,
- Neutron Multiplicity,
- Neutron Resonance Transmission Analysis,
- Nuclear Resonance Fluorescence,
- Passive Gamma,
- Passive Neutron Albedo Reactivity,
- Passive X-Ray Fluorescence,
- Self-Integration Neutron Resonance Densitometry, and
- Total Neutron Counting

However, these techniques are not fully developed nor implemented by the IAEA as of this writing. A pictorial categorization of current safeguards techniques is presented in Figure 2-1 [19], exhibiting the numerous methods implemented by the IAEA.

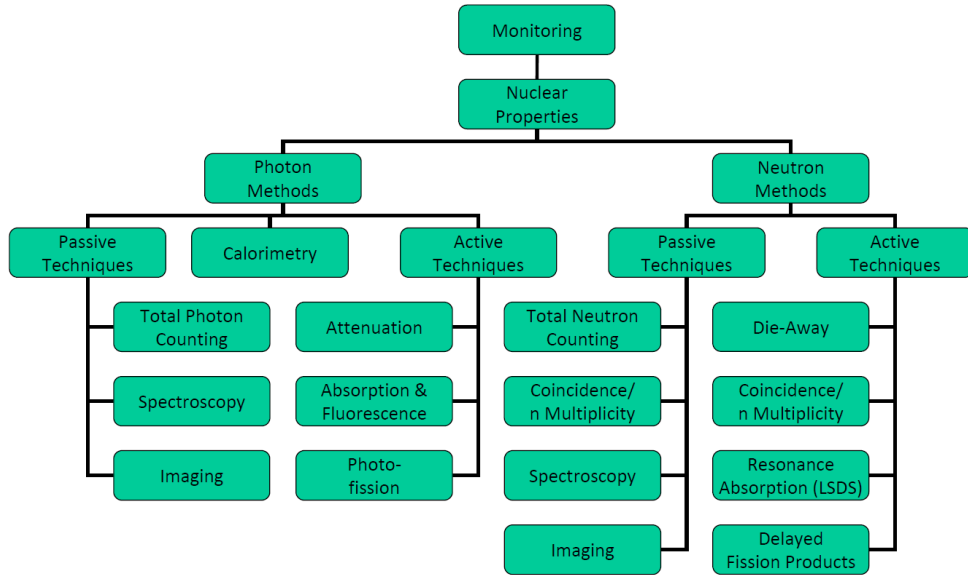


Figure 2-1: Nuclear nondestructive assay techniques

2.1.1 Nondestructive Assay Using Neutrons

Traditionally, reactor power is monitored with a neutron detector located next to the reactor core. Using reactor kinetics relationships, Khalafi et al. [20] showed the ability to determine reactivity based on the neutron detector data from the Tehran Research Reactor (TRR) in real time. The accuracy obtained with this method is sufficient to compare against experimental data for control rod worth and void coefficient reactivity as a reactor approaches full power. However, it is not sufficient for safeguards applications, since assumptions for the reactor kinetics parameters are incorporated into the system's algorithm.

An extended effort is currently being pursued to determine plutonium content in a spent fuel assembly through a technique known as differential die-away (DDA), which may be utilized with passive or active interrogation [21]. In active mode, the DDA concept introduces neutrons into a spent fuel assembly and relates the neutron population's "die-away" time to the fissile material content within the fuel assembly. However, the DDA instrument, in passive mode, works by using spontaneous fission and neutron sources within the fuel to act as the interrogation source, known as

differential die-away self-interrogation (DDSI) [22, 23]. The outcome of the work uses previously determined information from known fuel assemblies to correlate parameters such as burnup, initial enrichment, and cooling time for an unknown fuel assembly.

Additionally, a spent fuel coincidence counter (SFCC) was installed in a BN-350, a sodium-cooled fast reactor, in Kazakhstan in 2002 that used neutron singles and doubles rates from a spent fuel assembly to predict the plutonium content in the sample [24]. The equipment was calibrated using a known ^{252}Cf source and a fresh mixed oxide (MOX) assembly, and successfully estimated the plutonium content in spent fuel assemblies from the BN-350 to within approximately 8 percent.

Finally, total neutron counting (using fission chambers of ^3He -based detectors) may be utilized as a safeguards technique to characterize a spent fuel assembly based on burnup and cooling time.

2.1.2 Nondestructive Assay Using Photons

NDA using gamma rays is similar to those employing neutrons as the particle of interest. Burnup and cooling times are correlated to the intensity and specific signatures of gamma rays corresponding to specific isotopes [25].

Additionally, quantification of plutonium and minor actinide content in spent fuel may be performed using gamma ray spectroscopy (GR-S) on the sample (given certain burnup and cooling times) [25, 26], X-ray spectroscopy (XR-S) to determine individual isotope concentrations [27], or nuclear resonance fluorescence (NRF) induced with external gamma rays [28]. Several of these methods result in very accurate measurements; in particular, the uncertainty of the NRF is addressed by Shizuma et al. [29], concluding about 2-3 percent statistical precision in the actinide content.

However, the use of gamma-ray spectroscopy is not limited to spent fuel. Reactor power monitoring has also been investigated by Armozd et al. [30] and Jalali et al. [31, 32]. In reactor coolant, the interaction of fast neutrons with oxygen (O-16) in water produces nitrogen isotopes (N-16), which emits two gamma rays at energies of 6.13 MeV and 7.1 MeV. Armozd et al. utilized a linear relation between gamma ray intensity and reactor power to provide accurate values of reactor power for the TRR, and it is noted that reliable results were only obtained above a reactor power of 20 kW. Jalali et al. expanded this work with the Iranian Heavy Water Zero Power Reactor (HWZPR), and concluded that the prompt gamma intensity was linearly dependent on reactor power and sensitive to sudden variations in power, with the necessary accuracy for full-power measurement (above 100 W).

At the Kansas State University Training, Research, and Isotopes – General Atomics (TRIGA) Reactor, a group of researchers pursued the use of electro-optic radiation detectors to calibrate and monitor nuclear reactor pulses [33]. The detector's configuration included a Pockels cell to collimate light passing through an optically transparent Cadmium-Zinc-Tellurium (CdZnTe) crystal. Pulses were repeated ten times for each set of reactor pulses in increments of \$0.50 of reactivity from \$1.00 to \$2.50. The measurement system is placed outside the reactor to provide nonintrusive measurements, but the experimental results did not consistently confirm peak reactor power from fission chamber measurements, and was unsuccessful at measuring the pulse shape, making it infeasible to correlate to reactor kinetics parameters and ineffective in a safeguards regime.

2.1.3 Nondestructive Assay Using Antineutrinos

Antineutrino detectors are capable of detecting deviations from normal operating conditions, and have been described as “readily-deployable” [34]. At San Onofre Nuclear Generating Station, an antineutrino detector was installed to identify the feasibility of using this mechanism for monitoring power level and fissile material inventory. There are several drawbacks to the antineutrino method:

- The detector is large and has dimensions of approximately 17 by 17 by 40 inches, and it contains 1, 280 pounds of Gadolinium.
- Antineutrinos are weakly interacting, and the detector receives about 400 neutrinos per day when at full power, and only 10 percent of those are recorded due to the detector intrinsic efficiency.

Therefore, it may be possible to utilize Gadolinium-doped water to produce Cherenkov photons from the antineutrino reaction with protons in the detector material to create a neutron-positron pair that are detected in close time coincidence. The addition of Gadolinium reduces the time signature of the system and also creates gamma rays to induce secondary electrons, which then provide Cherenkov light in the water, which ultimately provides information about the reactor. Unfortunately, it is likely that this approach will possess a very poor energy resolution [34]. Recently though, this work has been expanded by Sweany et al. in 2011 [35], Erickson [36, 37], and Dazeley et al. in 2012 [38], who showed that an efficient system could potentially compete with large ${}^3\text{He}$ detector systems in terms of special nuclear material detection; however, antineutrino detection systems are not applicable to the proposed study. Due to their low detection efficiency, extended detection times are required and would not provide a large number of counts during a reactor transient, which is on the order of milliseconds.

2.1.4 Nondestructive Assay Using Cherenkov Light

Using gamma rays to measure and predict reactor behavior can theoretically be expanded to Cherenkov radiation, since Compton-scattered electrons produced by gamma rays are the largest producer of Cherenkov radiation in a nuclear reactor or spent fuel assembly. Cherenkov radiation is produced by any charged particle traveling through a dielectric medium with a velocity greater than the speed of light in the medium. A detailed discussion of Cherenkov radiation will be presented in Section 3.1.

The path for using Cherenkov light to monitor fissile material began in the early 1960s with Rippon's application [39] of using Cherenkov light for a reactor power monitor at the MERLIN research reactor in the UK. In 1967, Strindehag indicated that rapid increases in Cherenkov light may be used to determine fuel cladding failure, since fission products emitting radiation would be suspended in the reactor coolant [40]. Studies at Los Alamos nearly two decades later by Dowdy and Nicholson [41, 42] demonstrated that it was also possible to examine irradiated fuel using Cherenkov radiation by observing relative intensities in the Cherenkov light. Currently, the IAEA utilizes the measurement of Cherenkov light for spent fuel verification [43], which has been an effort led by the Canadian and Swedish safeguards programs. This effort is primarily aimed at spent fuel from power reactors, since their refueling intervals are much more frequent than most research reactors and volume of fissile material content is much larger. The Cherenkov light is measured with a Cherenkov Viewing Device (CVD) [5] or its more advanced design, the Digital Cherenkov Viewing Device (DCVD) [44]. The DCVD provides nearly 100 times more sensitivity in light collection than the Mark IV CVD [45]. The operation of these instruments is heavily documented since the early 1990s [46, 47], with an abundance of literature detailing system improvements, as well as their application to the spent fuel pools of boiling water reactors [48] and pressurized water reactors [49] in separate publications in the early 2000s. The DCVD is attached to a rail system on the bridge above the spent fuel pool for the purpose of examining the spent fuel in the pool from a field-of-view located directly above; the DCVD is not submerged and cannot be placed in high radiation fields, limiting the potential expansion of its current capabilities. Quantitative observations with the DCVD show excellent agreement with predictions based on theoretical models. The DCVD amplifies the faint UV Cherenkov light from the water surrounding the fuel, whose image may then be photographed or viewed directly for trained inspectors to examine. A filter is used to simultaneously collect 80 percent of the light between 280 and 320 nanometers (ultraviolet (UV) spectrum) and to block transmission of visible light from artificial sources within the bay for a wavelength range of 365 to 780 nanometers [50].

Improvements to the DCVD were made in the frame rate and digitizer system to demonstrate fuel assembly verification within a reasonable time frame [51]. In 2006, more robust post-processing was employed to increase the system's effectiveness at determining fuel assembly defects [52]. Additionally, in 2006 [53] and 2013 [54], detailed simulations were undertaken in order to assess the ability of the DCVD to verify partial defects based on location within the fuel assembly and other diversion mechanisms using Monte Carlo computational methods to produce electron fluxes for the determination of the assembly's Cherenkov light output in a variety of configurations. The DCVD is an intricate part of an IAEA inspector's toolkit, and 156 PWR spent fuel assemblies have been used to confirm its capability to detect 50 percent of fuel rods missing [55]. In fact, it has been shown that the removal of merely 3 percent of the fuel pins in a 17 by 17 fuel assembly can be detected if the pins are clustered together, though a more sophisticated diversion scenario may enable the removal of a higher number of pins. However, it is highly unlikely that the flux profile in a fuel assembly will remain unchanged if the diversion exceeds 20-25 percent of the total number of pins, which is well below the IAEA goal of 50 percent [56].

The development of the DCVD has proved successful in verifying fuel burnup and total cooling time, defined as time since fuel was removed from the core, with additional achievements in detecting gross and partial defects in fuel assemblies. Recall that a partial defect indicates that one or more pins are removed from the fuel assembly, while a gross defect refers to the removal of an entire fuel assembly with a dummy assembly in its place; partial defects tend to be more difficult to quantify and detect based on their reduced quantity of fissile materials when compared to their counterpart (gross defects). However, any quantity of diversion less than a partial defect is considered a bias defect, which is beyond the capabilities and traditional application of a DCVD.

Cherenkov light has been employed for reactor power measurements [7] and residual heat estimation [57-59] in the Tehran Research Reactor by Arkani and Gharib. Their research is greatly relevant to the current research objectives outlined in Section 1.2 and is fundamental to the application of using Cherenkov light for safeguards measurements, since Arkani's and Gharib's use of a charge-coupled device (CCD), or array of photodiodes, has shown that reactor power shows good linearity with the output voltage of the CCD. However, for nonproliferation purposes, their methodology is lacking in two specific areas: the method requires calibration of output voltage to known reactor power in watts prior to its effective implementation and does not attempt to calculate any reactor kinetics parameters. The CRANK system avoids the complication of calibrating photodiode output by correlating a *change* in Cherenkov light to a *change* in reactor power, which is essential to designing an effective safeguards measurement that is flexible for many research reactor facilities and does not heavily rely on operator's actions to accomplish its goal. Additionally, the research objectives outlined in Section 1.2 are fulfilled by utilizing a rapid data acquisition rate to measure the rate of change in Cherenkov light output and, therefore, calculate the reactor kinetics parameters with a high degree of accuracy.

2.1.5 Nondestructive Assay Conclusions

Typically, NDA methods are dependent on prior calibration of the instrument or the construction of library of values for the given parameters for future use in correlating the characteristics of an unknown sample or spent fuel assembly. However, the objective of this work is to determine kinetics parameters in a research reactor. Since most research reactors are unique designs, especially when including variables such as tank size and associated irradiation facilities, it is most beneficial for the CRANK system to be designed without reliance on prior calibration or comparison to pre-determined libraries.

The goal of the CRANK system is to expand an inspector's capabilities, not replace current technology. The CRANK system's method has a significant advantage in that light output does not need to be correlated to power, since the method relies on the ratio between two reactivity states. However, it is unavoidable that each NDA technique will depend on a facility's declarations to some degree, since confirmation of these declarations is the objective of any safeguards technique. Table 2-1 presents a summary of the methods of NDA discussed in this literature survey, with NDA method and target item specified, along with the lead author for each publication. It is important to note that of the research concerning Cherenkov light and reactor core, two previous studies (Rippon [39] and Strindehag [40]) did not address reactor kinetics. Instead, these focused on reactor power and sensing fission products in reactor coolant. This study, therefore, avoids replicating any NDA methods previously pursued and expands the use of Cherenkov light to the detection of diversion in an operating research reactor during normal operations. Furthermore, this study builds upon the work of Arkani and Gharib, who showed Cherenkov light intensity is proportional to reactor power by avoiding light calibration to a specific reactor configuration. Instead, the CRANK system will analyze the reactor power during a transient to enable its application in research reactor facilities with the capability for rapid reactivity insertions.

Table 2-1. Survey of Literature Summary for NDA

Author(s) [reference(s)]	Phenomena Investigated			Target Item	
	NDA Method with Neutrons	NDA Method with Gamma Rays	NDA Method with Cherenkov Light	Spent Fuel Assembly	Reactor Core
Khalafi [20]	Fission Chamber				X
Henzl [21]	DDA			X	
Kaplan [22, 23]	DDSI			X	
Lestone [24]	SFCC			X	
Willman [25]		GR-S		X	
Mora [26]		GR-S		X	
Turunen [27]		XR-S		X	
Hayakawa [28]		NRF		X	
Shizuma [29]		NRF		X	
Armozd [30]		GR-S			X
Jalali [31, 32]		GR-S			X
Nelson [33]		CdZnTe			X
Bowden [34]		WCD			X
Sweaney [35]	WCD	WCD		X	
Erickson [36, 37]	WCD	WCD		X	
Dazeley [38]	WCD			X	
Rippon [39]			Photomultiplier Tube		X
Strindehag [40]			Photomultiplier Tube		X
Dowdy [41]			CRT Camera	X	
Nicholson [42]			CVD	X	
Hildingsson [43]			CVD	X	
Attas [5, 50]			CVD, DCVD	X	
Chen [44, 45, 48, 49, 51, 52, 55]			DCVD	X	
Kuribara [46, 47]			CVD	X	
Lindberg [53]			Modeling CVD	X	
Grape [54]			Modeling DCVD	X	
Rossa [56]			Modeling DCVD	X	
Arkani & Gharib [7, 57 – 59]			Photodiode		X
CRANK System			Photodiode		X

2.2 Methods for Determination of Reactor Kinetics Parameters

The ability to experimentally determine the characteristics of a nuclear reactor have been of interest since the development of nuclear reactors in the 1940s, and a variety of techniques have been developed to determine these quantities. Reactor kinetics parameters are often computationally quantified with associated uncertainty by a reactor facility in order to submit safety analysis reports to a governing entity. The CRANK system provides the user with the ability to calculate the reactor kinetics parameters in a research reactor performing an intended prompt critical transient, allowing a comparison between declared values and independently determined reactor kinetics parameters from the CRANK system to within the guidelines defined by the IAEA for a significant quantity of fissile material [15].

2.2.1 Statistical Methods

Methods to determine kinetics parameters often couple together the delayed neutron fraction and the mean neutron generation time, since these two parameters are related and not easily differentiated from each other. Noise analysis techniques, such as Feynman- α , Rossi- α , and other methods, suffer from this constraint. These methods are experimental, frequently with the neutron flux being measured at low reactor power near delayed critical [60-61]. The variable α is termed the prompt neutron decay constant, given by:

$$\alpha = \frac{\rho - \beta}{\Lambda}, \quad (2-1)$$

where ρ is the reactivity of the system, β is the delayed neutron fraction, and Λ is the mean neutron generation time. A variety of methods exist to calculate this value statistically and analyze reactor parameters through detectors using noise theory. The reactivity of the reactor or critical assembly is altered in several instances, with a linear relation between ρ and α . If this relation is extended to $\rho = 0$, the ratio of the kinetics parameters is found (β/Λ). Some of these noise analysis methods are summarized by Paszit [62], Baker [63], and Uhrig [64]:

- Rossi- α : Determine the probability of detecting neutrons in same chain at time t_1 and t_2 to calculate the prompt neutron decay constant termed α .
- Feynman- α : If neutron counts are perfectly random (Poisson distribution), variance would equal mean. However, neutron counts are related through fission chains, and this method determines the excess (over one) of the variance of neutron counts divided by the mean of neutron counts to determine the prompt neutron decay constant.

In fact, Degweker [65] showed that the Feynman- α method is obtainable from the Rossi- α by a double integration. These methods can be utilized to perform safeguards measurements, in particular, for passive neutron coincidence counting (PNCC) [66]. However, in cases of kinetics parameters determination in an operating reactor, Feynman and Rossi- α methods do not provide a proliferation-resistant technique to a safeguards inspector. Additional methods of kinetics parameter determination are based upon the former two, and include:

- Bennet Variance Method [63]: Very similar to Feynman- α , this method was developed to account for the difficulty in using an expanded form of Feynman- α that includes delayed neutrons, since the Feynman- α method diverges near a reactor state of delayed critical.
- Zero-Count Probability Method [63]: Describes the probability of obtaining zero counts during a time interval, and uses this to calculate the prompt neutron decay constant.
- Nelson Number Method [67]: Similar to Rossi- α , the expression is based on normalizing the neutron source during reactivity steps in a slightly subcritical assembly.

Many researchers have used experimental methods to determine reactor kinetics parameters for specific reactors. Table 2-2 includes experimental reactor kinetics investigations with the corresponding leading author, the method used, and the reactor that was investigated. The outcome of this study uses the Oregon State

TRIGA Reactor (OSTR) to determine its reactor kinetics using the Cherenkov light and the CRANK system using an experimental method during a prompt critical reactor transient, where the statistical- α methods are not applicable. It should be noted that the list in Table 2-2 is by no means exhaustive; many reactor facilities publish their reactor kinetics parameters in a safety analysis report rather than in the form of journal articles, and the methods used to calculate the kinetics values are varied.

2.2.2 Computational Methods

Computational tools may also be used to calculate kinetics parameters (often using Monte Carlo methods) by tracking prompt and delayed neutrons to determine an effective delayed neutron fraction and mean neutron generation time. For MCNP5, version 1.60 specifically [68], Baker [63] explains that previous stochastic methods have lacked adjoint flux calculation capabilities, causing the calculations to be done instead with a deterministic method. Monte Carlo methods utilize a technique called the iterated fission probability interpretation, which reflects that the adjoint is an importance function and allows the kinetic parameters to be weighted by the adjoint flux while using a forward calculation of the neutron flux. The adjoint weighted generation time, or effective generation time, Λ , is given by [69]

$$\Lambda = \frac{\int \psi^\dagger(r, \hat{\Omega}', E') \frac{1}{v} \psi(r, \hat{\Omega}, E)}{\int \psi^\dagger(r, \hat{\Omega}', E') F(r, E, E') \psi(r, \hat{\Omega}, E)}, \quad (2-2)$$

where the integrations are carried over all variables, ψ is the angular neutron flux, ψ^\dagger is the adjoint angular flux, v is the neutron speed, and F is the fission operator:

$$F(r, E, E') = \chi(E \rightarrow E') v \Sigma_f(r, E), \quad (2-3)$$

in which $v \Sigma_f$ is the total (prompt and delayed) fission neutron production cross section and χ is the total fission spectrum. The effective delayed neutron fraction is defined similarly [69]:

$$\beta_{eff,j} = \frac{\int \psi^\dagger(r, \hat{\Omega}', E') B_j(r, E, E') \psi(r, \hat{\Omega}, E)}{\int \psi^\dagger(r, \hat{\Omega}', E') F(r, E, E') \psi(r, \hat{\Omega}, E)}, \quad (2-4)$$

where B_j is the delayed neutron emission source operator:

$$B_j(r, E, E') = \chi_{dj}(E') \nu_{dj} \Sigma_f(r, E), \quad (2-5)$$

in which $\nu_{dj} \Sigma_f$ is the delayed neutron production cross section and χ_{dj} is the delayed neutron emission spectrum for precursor group j. The total β_{eff} is given by:

$$\beta_{eff} = \sum_j \beta_{eff,j}. \quad (2-6)$$

In 2009, Abou El Maaty et al. [70] investigated the influence of variations in kinetics parameters affecting the reactivity insertion. By varying the parameters of interest, it can be easily determined that the reactivity in the system is more sensitive to changes to delayed neutron fraction (β_{eff}) than the neutron mean generation time (Λ), and can drastically affect the accuracy of the transient in a simulation environment, reducing the reliability of computational models. To reduce the uncertainty in simulation, the quantities are required to be determined experimentally. Table 2-2 also includes computational reactor kinetics investigations with the corresponding leading author, the method used, and the reactor that was investigated. It is observed that many authors choose to evaluate reactor kinetics based on Monte Carlo methods, though others decide to evaluate them with diffusion theory by simulating small reactivity perturbations.

2.2.3 Reactor Kinetics Determination Conclusions

Table 2-2 provides a survey of publications that concern the determination of reactor kinetics and the method for each. However, none of these methods are appropriate for safeguards applications for research reactors with pulsing capabilities. The CRANK system is able to detect the ratio of the kinetics parameters, (β/l) or (β/Λ) depending on type of reactivity insertion as discussed in Section 3.2, in a research reactor during a transient, with the mathematical formulation of the method provided in Section 3.2. Explicit determination of a single kinetics parameter is not possible in the CRANK

system or the experimental methods listed in Table 2-2 unless one of the parameters is assumed. Additionally, computational methods are limited by reactor geometry and composition, and cannot be used to obtain accurate results in a safeguards application.

Table 2-2. Calculated Reactor Kinetics Survey

Author(s) [reference(s)]	Experiment or Computational	Method of Reactor Kinetics Determination	Reactor
Spriggs [71]	Experimental	Rossi- α	Highly Enriched Uranyl Nitrate Solution Reactor
Por [72]	Experimental	Feynman- α	Budapest Research Reactor
Spriggs [73]	Experimental	Rossi- α	JAERI XIX-1 Assembly
Kuramoto [74]	Experimental	Feynman- α	IPEN/MB-01 Research Reactor
Pepyolyshev [75]	Experimental	Rossi- α	IBR-2 Pulsed Reactor
Baker [63]	Experimental	Rossi- α , Feynman- α , Bennett Method	Idaho State University AGN-201
Muhammad [76]	Experimental	Noise Analysis	Pakistan Research Reactor
Hosseini [77]	Computational	Inhour Equation	Tehran Research Reactor
Brettscher [78]	Computational	Diffusion Theory without Perturbations	Georgia Tech Research Reactor, Oak Ridge Research Reactor
Zaker [79]	Computational	Diffusion Theory	Tehran Research Reactor
Jonah [80]	Computational	Monte Carlo Methods	Nigerian Research Reactor Highly Enriched Core
Iqbal [81]	Computational	Monte Carlo Methods	Pakistan Research Reactor
Hosseini [82, 83]	Computational	Rossi- α & Feynman- α Simulation	Tehran Research Reactor
Abtin [84]	Computational	Monte Carlo Methods	Iranian Miniature Neutron Source Reactor
Khan [85]	Computational	Diffusion Theory	Bangladesh TRIGA Mark-II
Leppanen [69]	Computational	Monte Carlo Methods	General
Abou-El-Maaty [70]	Computational	PRKEs & Thermal Hydraulic Coupling	ETRR2
Yamamoto [86]	Computational	Monte Carlo Perturbation Techniques	General
CRANK System	Experimental	Integral Ratio	OSTR

2.2.4 Conclusions for Reactor Kinetics Parameters Methods

The CRANK system deviates from traditional methods for determination of reactor kinetics parameters, and the method will be detailed in Section 3.2.3. Traditional Feynman- α and Rossi- α methods utilize a reactor at subcritical or delayed critical conditions and are not appropriate for measurement of reactor kinetics parameters as part of a safeguards inspection for material diversion, since these measurements are highly dependent on reactor operators' actions. All research reactors must publish their reactor kinetics parameters as part of a Final Safety Analysis Report (FSAR) with the respective nuclear governing commission and are usually calculated with computational Monte Carlo methods. The CRANK system allows for the independent measurement of reactor kinetics to be compared against declared values to provide a safeguards inspector with the ability to determine material diversion.

3 THEORY

In order to accomplish the objectives of this work, a nuclear reactor is necessary to provide a source of Cherenkov light for the CRANK system to measure the reactor kinetics parameters. In preliminary, desktop tests, a programmable LED light source was utilized to provide any necessary calibration for the data acquisition system and ensure the system's reliability for full-scale experiments, since the OSTR is capable of performing square waves and/or pulses for the prompt reactivity insertion that will perturb the reactor from its initial steady-state.

3.1 Cherenkov Physics

Cherenkov radiation is electromagnetic radiation emitted when a charged particle travels through a dielectric material (i.e. water) faster than the phase velocity of light in that medium. As the charge particle moves through the medium, it forms dipoles as the electrons and nuclei are displaced to opposite sides of the atoms in the medium. At relatively low speeds, the polarization field from the particle is nearly symmetric, so there is almost no radiation observed at large distances. However, as the particle's speed increases, the polarization field becomes increasingly asymmetric along the path of the particle and extends some distance from the path.

Ultimately, the mechanism producing Cherenkov light is the coherent emission by the dipoles formed due to the polarization of the atoms in the medium by the moving charged particle. If the velocity of the particle is greater than the phase velocity of the light in the medium, the radiated light produces a field observable at a distant point [87], illustrated in Figure 3-1. Cherenkov radiation is given off at a characteristic angle, θ , from the incident charged particle based on its velocity relative to the speed of light in a vacuum, c , and the medium's index of refraction, n , given by the relationship

$$\cos \theta = \frac{1}{\varepsilon n} , \quad (3-1)$$

which leads to the limit as θ approaches zero of $\varepsilon_{\min} = 1/n$. However, for an ultra-relativistic particle when ε approaches unity, the angle of radiation $\theta_{\max} = \cos^{-1}(1/n)$. The radiation occurs mostly in the visible and UV regions of the electromagnetic spectrum for $n > 1$ [87].

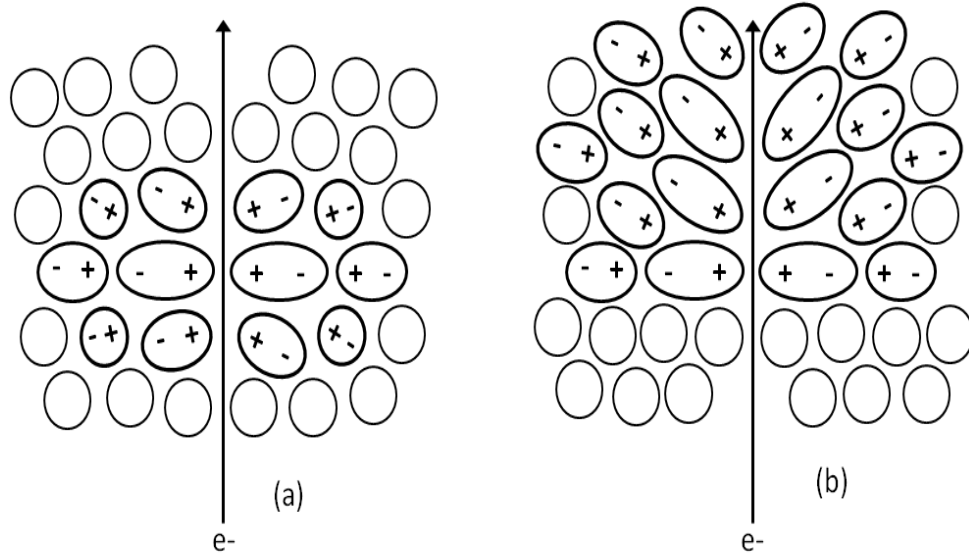


Figure 3-1: Polarization induced by a charged particle moving through matter
(left) slow movement and (right) relatively fast movement

Cherenkov light was first observed during the early years of radiation physics, when it was noticed by Curie, Rutherford, and other scientists who noticed a faint glow surrounding a radiation source when it was submerged in water. It was distinguished from other phenomenon by Sergey I. Vavilov and his post-graduate student, Pavel A. Cherenkov, in 1934 [8] when they indicated that gamma rays of a radium solution caused luminescence as well as a visible, faint light from the solvents. As a result, Cherenkov's name has been utilized to describe the radiation itself. In related literature, his name may be written as Cherenkov or Cerenkov based on author choice. These two names are equivalent and may be interchanged without concern. Henceforth, the chosen nomenclature will be Cherenkov, with the namesake radiation (usually visible or UV light) resulting from particles traveling at a super luminous

velocities through a dielectric medium. Following the discovery of the phenomenon, the mathematical explanation of the Cherenkov radiation was detailed by Frank and Tamm in 1937 and confirmed by several international physicists soon thereafter [88]. The comprehensive quantitative theory afforded an exhaustive interpretation of all the peculiarities of the new phenomenon, including its most remarkable characteristic – the asymmetry of light polarization within the medium. Both sets of physicists received Nobel prizes for their work in this research area in 1958 [89, 90]. In 1985, a detailed textbook concerning the physics of Cherenkov radiation was authored by Jelley [87].

3.1.1 Mechanism of Light Production

In a nuclear reactor, the most common cause of Cherenkov radiation directly from charged particles is the movement of electrons produced from beta decay. However, uncharged particles, such as gamma rays, can indirectly produce Cherenkov light when interactions with atoms yield high-energy electrons. From literature [7, 87], Compton-scattered electrons are often the main contributors to Cherenkov radiation in reactors. The photons are emitted at an angle characteristic of the charged particle's velocity and the index of refraction of the medium as shown previously. The kinetic energy for a charged particle to produce Cherenkov light has a lower threshold based on the medium and the particle's rest mass. Based on (3-1), it is expected that Cherenkov light is only produced when:

$$1/n \leq \varepsilon < 1. \quad (3-2)$$

For $\varepsilon = 1/n$, the radiation is observed at an angle θ , while for the extreme with $\varepsilon = 1$, the angle θ reaches a maximum value

$$\theta_{\max} = \cos^{-1}\left(\frac{1}{n}\right) = \arccos\left(\frac{1}{n}\right). \quad (3-3)$$

For instance, in the case of water, $n \approx 1.33$, the minimum fractional velocity is equal to $1/1.33 = 0.75$. Therefore, the Cherenkov radiation is observed in water whenever $\varepsilon \geq 0.75$. For an electron passing through the water, this condition is satisfied if

$$T_e = m_e c^2 \left(\frac{1}{(1 - \varepsilon^2)^{1/2}} - 1 \right) = 0.511 \text{ MeV} \left(\frac{1}{(1 - 0.75^2)^{1/2}} - 1 \right) = 0.262 \text{ MeV}. \quad (3-4)$$

Therefore, an electron with kinetic energy greater than 262 keV will produce Cherenkov radiation in water.

It is important to recognize the differences between Cherenkov radiation and other phenomena that produce photons in the visible portion of the electromagnetic spectrum, such as recombination or excitation radiation associated with ionization caused by a charged particle. Additionally, it should not be mistaken for bremsstrahlung, which is an acceleration radiation produced when the particle is influenced by the electrostatic field of an atomic nucleus [87].

For the purpose of this work, the number of photons, and therefore the intensity of light, will be assumed linearly proportional to the power level of the reactor, demonstrated in experiments performed by Arkani and Gharib at the Tehran Research Reactor in 2009 [7, 31]. However, the linearity of the relationship was not shown to be valid below a certain threshold of ~ 100 kW, though this research only observed steady-state behavior and utilized the system as a safety feature, not as an investigative tool. Their work also shows that it is necessary to subtract the background light or use a wavelength filter in order to correctly determine the amount of light coming from the reactor. Therefore, to identify the kinetics parameters of fissile materials, it is beneficial not to correlate the Cherenkov light intensity to power level of the reactor. Instead, the change in reactor power over the course of a reactivity perturbation will be used to determine the desired quantities.

Based on information from Ilver [91], the wavelength of interest for Cherenkov occurs at a peak of approximately 310 nanometers from a spent fuel assembly submerged underwater; in Figure 3-2 [91], the relative Cherenkov light intensity is provided as a function of depth in water. Additionally, the Cherenkov production is

governed by the Sellmeier correlation [92, 93] shown in the blue line and follows a $1/\lambda^4$ relationship and results in the predominant production of photons at lower wavelengths, especially in the UV spectrum (<380 nm). However, the attenuation of light in water is dependent on wavelength and is greater at lower wavelengths, causing a wavelength peak to be observed in the other four wavelength spectra. The testing of the CRANK system employed the use of the OSTR, detailed in Section 4.1, a pool-type reactor whose core is submerged 16 feet underwater, resulting in a Cherenkov light spectrum consisting primarily of high-UV and violet light. Figure 3-3 provides a view of the OSTR from reactor top during full power operations at 1 megawatt of thermal power.

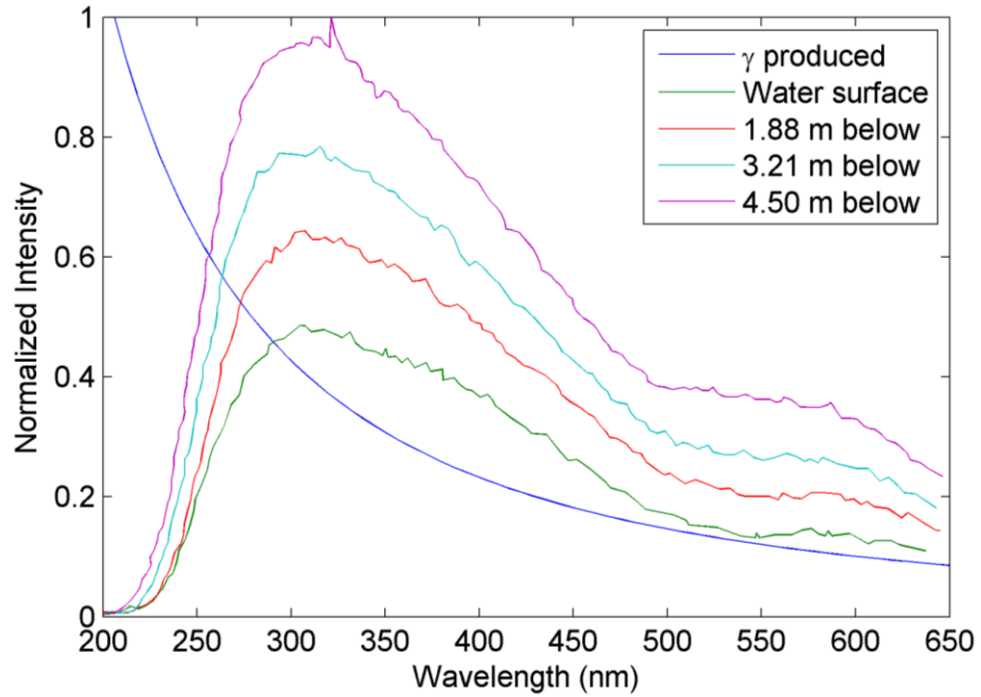


Figure 3-2. Cherenkov light intensity as a function of wavelength.

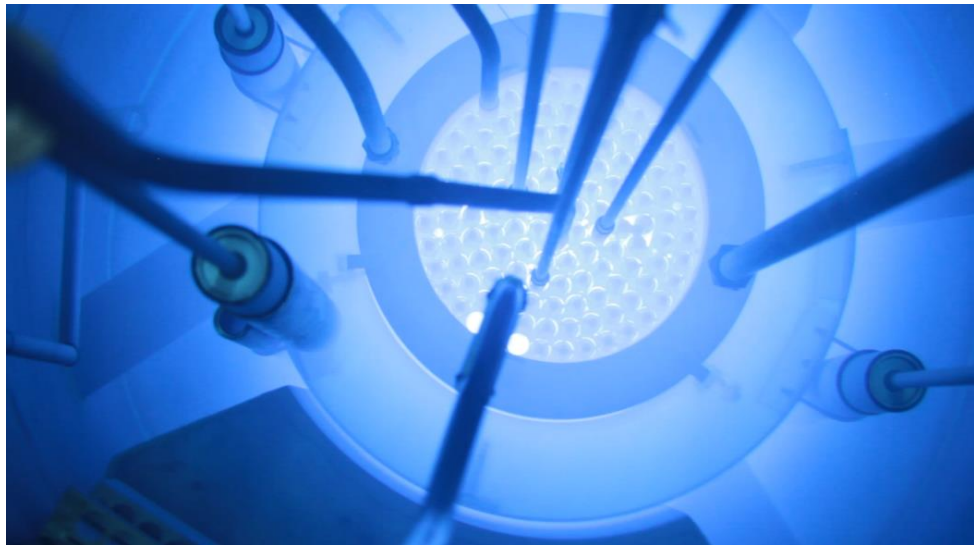


Figure 3-3. View of OSTR at steady power of 1 MW.

3.1.2 Computational Tools for Cherenkov Light

Though the focus of this study is to perform experimental measurements in pursuit of a new tool for IAEA inspectors during investigations of research reactor facilities, computational models will be used to support and confirm experimental measurements. Traditionally, Monte Carlo methods are employed for simulating Cherenkov light, and recently, Monte Carlo N-Particle (MCNP), version 6.1.1 [94, 95] included a physics package for Cherenkov photon production from charged particles. In order to use this feature, the refraction index of a material must be specified for MCNP6 to calculate the number of Cherenkov photons produced per interaction event in the medium. The verification of the Cherenkov physics is performed by Durkee and James using sample calculations with simple geometry [92] and implementation of the Cherenkov physics is detailed by James [93]. Geometry creation is simple in MCNP6, and modeling of the Cherenkov light production in the OSTR is used to confirm measurements taken with the CRANK system in the OSTR as part of the study proposed in this document.

Finally, computational models are used to support experimental measurements of the Cherenkov light intensity from the data acquisition system (DAS) during the reactor

transients. Advancements in computational physics simulations allow the prediction of Cherenkov light production through Monte Carlo methods. MCNP6 functions by assembling specific cards compiled into a single deck, with program options specified by the physics cards included into the code. Figure 3-4 provides a plot of sample Cherenkov photon yield utilized in MCNP6; the two lines represent different predictions of photons per wavelength based on the physics model options chosen by the user. The Cauchy model is appropriate for gaseous media, while Sellmeier is appropriately used for liquids and solids; therefore, the Sellmeier correlation is used in models of the OSTR. Figure 3-4 represents the number of photons produced per wavelength interval with 100 wavelength intervals from 200 to 800 nanometers for a 4-Mev electron in water as defined by the Cauchy and Sellmeier models in MCNP6.1.1 Cherenkov physics options.

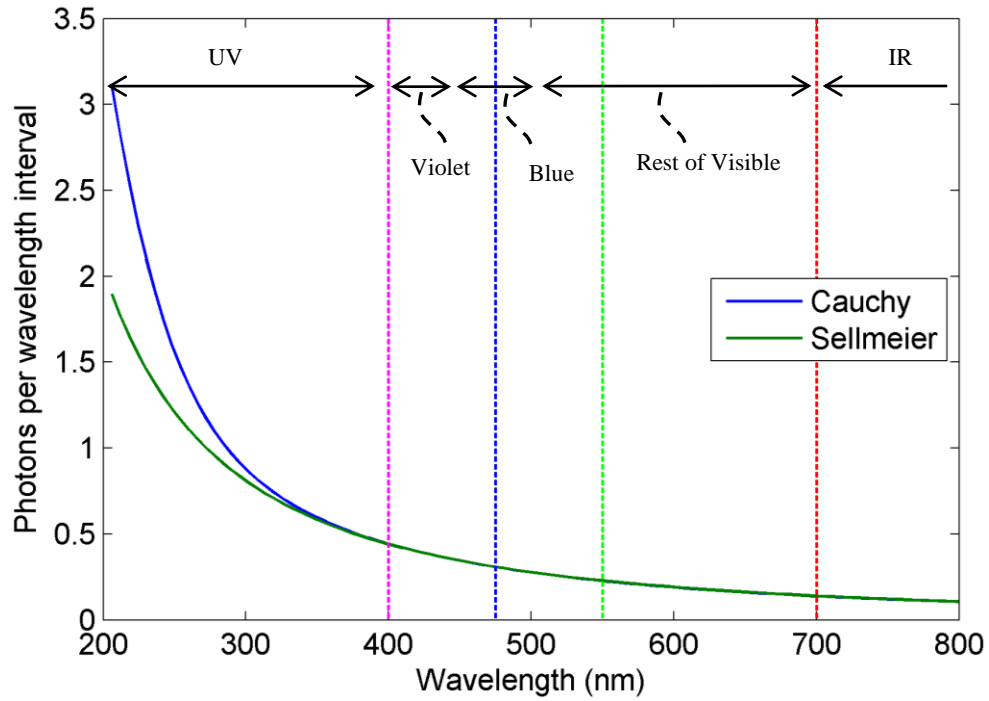


Figure 3-4: Sample Cherenkov photon yield utilized in MCNP6.

3.2 Reactor Kinetics

As discussed in Section 2.1, a bias defect refers to a discrepancy in enrichment or weight by a small fraction of fissile material. The CRANK system is designed to measure the Cherenkov light in a research reactor during a transient to ascertain the ratio of the reactor kinetics parameters as part of a safeguards program; therefore, the system must be able to identify slight discrepancies in the reactor kinetics parameters. In a diversion scenario, the expected values for the kinetics parameters may be very similar to measured values, potentially making it difficult to determine a reactor's kinetics parameters with statistically confidence.

The delayed neutron fraction is a characteristic pertaining specifically to the fissile material composition in the reactor. Typically, the effective delayed neutron fraction of U-235 is approximately 0.007, while the effective delayed neutron fraction of Pu-239 is approximately 0.003. Over the course of a reactor's operating history, the delayed neutron fraction decreases as original fuel, composed of U-235, is "burned" and Pu-239 is produced through the transmutation of U-238. Therefore, unless the reactor kinetics parameters are measured at the beginning-of-life (BOL) with a single fissile isotope composition, the fuel comprises a mixture of fissile isotopes, and the delayed neutron fraction must be computed in (3-5) with atom-weighted averages of the fissile material, predominantly U-235 and Pu-239 [96]. Each isotope is denoted by q in (3-5),

$$\beta_{mix}^i = \frac{\sum_{q=1} v_q \sigma_f^q N_q(t) \beta_q^i}{\sum_{q=1} v_q \sigma_f^q N_q(t)} \quad (3-5)$$

where v is the average number of neutrons produced per fission for each isotope, σ_f is the fission cross section for each isotope, and $N_q(t)$ is the concentration of the isotope in the overall fuel mixture; for the simplified model, $N_q(t)$ is assumed to not change with time, and this is represented by the fraction of isotope in fuel mixture. Lastly, β^i is the delayed neutron fraction for each precursor group of the given isotope [6], with the sum of β^i over all precursor groups providing the delayed neutron fraction. The

effective delayed neutron fraction is smaller in a reactor core with Pu-239 as the primary fissile material than the same reactor core geometry with U-235.

The other reactor kinetics parameter of interest, the prompt neutron lifetime, is affected by more phenomena than the delayed neutron fraction, so is more complex in its assessment. The prompt neutron lifetime is the mean time between a neutron's emission by fission to the absorption of the neutron or its escape from the system [97]. Generally, the prompt neutron lifetime increases with reactor operations as fissile isotope density decreases, though increased Pu-239 content causes an increase in prompt neutron lifetime [98-104]. However, the former effect dominates the latter. As a result, it is difficult to analytically predict the prompt neutron lifetime at a given time in a reactor's life and the ratio of the reactor kinetics parameters (β/l) might possess the same value at multiple instances in the reactor's life. From a safeguards perspective, an inspection method that attempts to determine the ratio of the reactor kinetics parameters, therefore, require repeated inspections at a specified interval depending on each facility's characteristics and inspection history.

The CRANK system aims to measure the Cherenkov light intensity from the entire reactor, so the ratio or individual reactor kinetics parameters are core averaged parameters, rather than local measurements, which impacts the lower limit of fissile material that can be detected with the methodology outlined in Section 3.2.3 and Section 3.2.4.

3.2.1 Mathematical Models of Reactor Kinetics

The power produced by fission is driven by the neutron population in the reactor, with prompt and delayed components. The delayed neutrons are produced by the decay of fission products, and due to the probabilistic decay of the fission products, they are collected in specific groups based on neutron precursor half-lives. In most cases, six or eight neutron precursor groups are utilized when solving the PRKEs

numerically [6]. The kinetics parameters may be time or temperature dependent, but each case must be solved individually based on the physical situation being modeled.

For the CRANK system to be effectively implemented as a safeguards tool, experimental results must be compared to theoretical reactor kinetics relationships, allowing the determination of the reactor kinetics parameters. The Cherenkov light is assumed to be linear with reactor power, based on the discussion in Section 1.1 and Section 2.1.2, allowing an experimental measurement of the Cherenkov light intensity to be used in reactor kinetics equations as analogous to reactor power during an intended reactor transient. A set of differential equations, known as the PRKEs is used to compare the measured response of the Cherenkov light to predicted power in the reactor based on its kinetics parameters. The PRKEs are given by the coupled differential equations [6, 97, 98]:

$$\frac{dP}{dt} = \frac{\rho(t) - \beta}{\Lambda} P(t) + \sum_i \lambda_i C_i(t) + S \quad (3-6)$$

and

$$\frac{dC_i}{dt} = \frac{\beta_i}{\Lambda} P(t) - \lambda_i C_i(t), \quad (3-7)$$

where P is the reactor power, C_i is the precursor concentration for each delayed neutron “group,” and S is the strength of an external neutron source. Additionally, ρ represents reactivity value of the reactor, β_i is the delayed neutron fraction for each precursor group, β is sum of delayed neutron fraction weighted for each precursor group, λ_i is the decay constant for each precursor group, and Λ represents the mean neutron generation time. The mean neutron generation time is dependent on the prompt neutron lifetime and the reactivity inserted, shown as

$$\Lambda = l(1 - \rho), \quad (3-8)$$

where l is the prompt neutron lifetime.

The PRKEs model an entire reactor with a single point, and, as a result, are limited by several conditions [6]:

- Neutron flux and power shape remains in a fundamental mode to characterize a reactor core that has been subjected to reactivity change away from critical,
- One-speed diffusion approximation is valid, and
- Reactivity insertions do not occur locally, but affect the reactor ubiquitously at the instant reactivity change occurs.

In cases of reactivity insertion, it is common to label them in terms of dollars, where

$$\$ = \frac{\rho}{\beta} \quad (3-9)$$

Additionally, one major modification that is often made to the PRKEs concerns the variable used to represent the delayed neutron fraction. Since delayed neutrons are born with noticeably less energy than prompt fission neutrons, they are more effective at creating fission since fewer collisions are necessary to reduce the neutrons to thermal energies. As a result, it is necessary to alter β to β_{eff} , where the *effective* delayed neutron fraction has a larger value than the delayed neutron fraction [6].

3.2.2 Numerical Solutions to PRKEs

A numerical solution is readily found by evaluating the precursor concentration based on an average of the power level at the current time step (t_n) and the next time step (t_{n+1}) given by

$$P_{avg} = \frac{P(t_{n+1}) + P(t_n)}{2}. \quad (3-10)$$

For the solution, the time step is defined as

$$\Delta t = t_{n+1} - t_n. \quad (3-11)$$

The exact solution is given below and is solved iteratively for each time t_{n+1} . For all cases to be run as part of this study, the time step used is sufficiently small to prevent

numerical instability, since the solution for the full PRKE utilizes an explicit solution method.

$$P(t_{n+1}) = P(t_n) e^{\left(\frac{\rho(t_n)-\beta}{\Lambda(t_n)}\right)\Delta t} + \sum_{i=1}^6 \lambda_i C_i(t_n) \left(e^{\left(\frac{\rho(t_n)-\beta}{\Lambda(t_n)}\right)\Delta t} - 1 \right) \left(\frac{\rho(t_n)-\beta}{\Lambda(t_n)} \right)^{-1} \quad (3-12)$$

and

$$C_i(t_{n+1}) = C_i(t_n) e^{-\lambda_i \Delta t} + \frac{\beta_i}{\lambda_i \cdot \Lambda(t_n)} P_{avg} \left(1 - e^{-\lambda_i \Delta t} \right). \quad (3-13)$$

In cases of larger reactivity insertions, the temperature coefficient of reactivity (α) is always negative for pulsing research reactors, such as the OSTR, and causes the reactivity to decrease as reactor power rises. In the explicit numerical solution for the PRKEs, the temperature rise and subsequent reactivity change are dependent on the reactor power and core temperature [105]. The total core heat capacity of the OSTR at a given temperature is dependent on the reactor power:

$$C_p(T') \frac{dT'}{dt} = P(t). \quad (3-14)$$

The declared values of the temperature coefficient of reactivity and specific heat capacity for the OSTR are found in the FSAR [106] and in Table 3-1, calculated with MCNP5 [68]. The total core heat capacity is dependent linearly on temperature (3-15).

$$C_p(T) = C_{p0} + C_{p1} \cdot T \quad (3-15)$$

By integrating (3-15), the left-hand side of (3-14) becomes (3-16). When evaluated over a time step, Δt , the integration becomes (3-17) when utilizing the average power between time steps.

$$\int C_p(T) dT = C_{p0} \cdot T + \frac{C_{p1}}{2} \cdot T^2 \quad (3-16)$$

$$\left(C_{p0} \cdot T_{n+1} + \frac{C_{p1}}{2} \cdot T_{n+1}^2 \right) - \left(C_{p0} \cdot T_n + \frac{C_{p1}}{2} \cdot T_n^2 \right) = \left(\frac{P_{n+1} + P_n}{2} \right) \cdot \Delta t \quad (3-17)$$

Solving for T_{n+1} results in (3-18).

$$T_{n+1} = \frac{-C_{p0} + \left(C_{p0}^2 + 2 \cdot C_{p1} \cdot \left(\left(C_{p0} \cdot T_n + \frac{C_{p1}}{2} \cdot T_n^2 \right) + \left(\frac{P_{n+1} + P_n}{2} \right) \cdot \Delta t \right) \right)^{\frac{1}{2}}}{C_{p1}} \quad (3-18)$$

Then, the temperature at the next time step is used to calculate reactivity in the next time step based on a varying temperature coefficient of reactivity (α), with OSTR values found in Table 3-1.

$$\rho_{n+1} = \rho_n + \alpha(T_{n+1}) \cdot (T_{n+1} - T_n) \quad (3-19)$$

The explicit numerical solution, shown in (3-12) and (3-13) can be expanded by characterizing the reactivity insertion, ρ , as a ramp insertion rather than a step change. The alteration to the definition ρ in (3-19) for a ramp insertion is found in (3-20) and makes little difference in the magnitude of the reactor transient or the profile of the transient, though by implementing a ramp rate, large differences occur when attempting to ascertain accurate values of the reactor kinetics parameters. For the case of a ramp insertion, the control rod worth tables, supplied by the OSTR staff, were used to calculate the reactivity inserted by the control rod withdrawal as a function of time using the known air pressure (80 psi) and mass of the control rod being ejected (approximately 15 lbs), so that the reactivity inserted becomes:

$$\rho_{n+1} = \rho_n + \alpha(T_{n+1}) \cdot (T_{n+1} - T_n) + \rho_{ramp}(t_{n+1}) - \rho_{ramp}(t_n) \quad (3-20)$$

Table 3-1. Reactor Kinetics Parameters for OSTR LEU Core

Specified Time in Fuel Cycle	Beginning of Life (BOL)	Middle of Life (MOL)	End of Life (EOL)
Delayed Neutron Fraction (β)	0.0076 ± 0.0001	0.0073 ± 0.0002	0.0075 ± 0.0002
Prompt Neutron Lifetime (l) in μs	22.6 ± 2.9	19.0 ± 1.9	30.7 ± 2.8
Temperature Coefficient of Reactivity (α)	$1.797 \times 10^{-5} \cdot T + 1.065 \times 10^{-3}$	$1.320 \times 10^{-5} \cdot T + 1.161 \times 10^{-3}$	$8.733 \times 10^{-6} \cdot T + 2.167 \times 10^{-3}$
Total Core Heat Capacity (W-s/ $^{\circ}\text{C}$)	$C_\rho = 69058 + 141.68 \cdot T$		

3.2.3 Reactor Pulses

The vast majority of research reactors with pulsing capability possess a negative feedback coefficient, which causes a decrease in reactivity with an increase in reactor power. During a pulse, the reactor power rapidly increases at an exponential rate proportional to the reactivity inserted. At a particular instance, the slope of the power decreases due to the negative feedback, causing a maximum power to be reached and a subsequent decrease in power to occur following this maximum.

It is desirable to define a specific, repeatable methodology for the analysis of reactor pulses based on an analytical solution of the point reactor kinetics equations (PRKEs) [6]. An analytical solution to the PRKEs may be found for a reactor pulse by assuming that no source neutrons or neutron precursors exist during the reactor pulse. On average, a \$2.00 pulse in the OSTR occurs over 30 milliseconds with a full-width half maximum (FWHM) of approximately 10 milliseconds. For comparison, the fastest decaying U-235 neutron precursor group has a half-life of 17.9 milliseconds, constituting 2.6 percent of all delayed neutron precursors [6]. The next fastest-decaying neutron precursor group occurs with a half-life of 49.6 milliseconds, justifying the assumption of zero precursor contribution to the reactor power during a large reactor pulse in the OSTR. A useful approximation to the PRKEs during a reactor pulse, or reactivity insertions greater than \$1.00, as defined by (3-9), is the Fuchs-Nordheim (FN) model, which solves the PRKEs with no delayed neutron precursors or external source and reduces (3-6) to (3-21), [98].

$$\frac{dP}{dt} = \frac{\rho(t) - \beta}{l} P(t) \quad (3-21)$$

The FN model assumed that the temperature coefficient of reactivity and heat capacity of the reactor are constant, provided by (3-22) and (3-23) where ρ_0 is the initial reactivity insertion.

$$\rho = \rho_0 - \alpha \cdot T(t) \quad (3-22)$$

$$C \frac{dT}{dt} = P(t) \quad (3-23)$$

Additionally, the initial reactor power is neglected due to the magnitude of the peak power during a reactor pulse, though solutions exist to include initial power [107]. However, the inclusion of initial reactor power does not drastically affect the pulse shape and results only in a temporal shift in the reactor power. With these assumptions, it is possible to derive the power as a function of time. Traditionally, the FN model is formulated so that the maximum power occurs at $t = 0$, resulting in (3-24) [98].

$$\frac{P(t)}{P_{\max}} = \operatorname{sech}^2\left(\frac{\omega t}{2}\right), \quad (3-24)$$

where ω is the initial transient reactor period following the reactivity perturbation and defined by (3-25).

$$\omega = \frac{\rho_0 - \beta}{l} = \frac{\beta(-1)}{l} \quad (3-25)$$

The pulse shape predicted by the FN model is not dependent on the temperature feedback of the reactor during the transient, since it is assumed constant in the derivation of the FN model. During experiments, the FN model is used to compare normalized experimental Cherenkov light data in order to calculate ω , which may then be correlated to the β/l ratio based on the dollar value of the reactivity insertion. The reactivity insertion in dollars is found by the reactor operator in rod control worth tables, a standard document for the majority of research reactors. Figure 3-5 provides a comparison of the FN model (3-24) with the PRKE explicit solution (3-12) for a time step of 1 microsecond with step reactivity insertion (3-19) and a ramped reactivity insertion (3-20) for a \$2.00 pulse and a \$1.75 pulse for the OSTR BOL parameters. A baseline signal is introduced to the PRKE solutions to more accurately model experimental data, and all curves are normalized to their peak power and the curves are centered on the peak at $t = 0$.

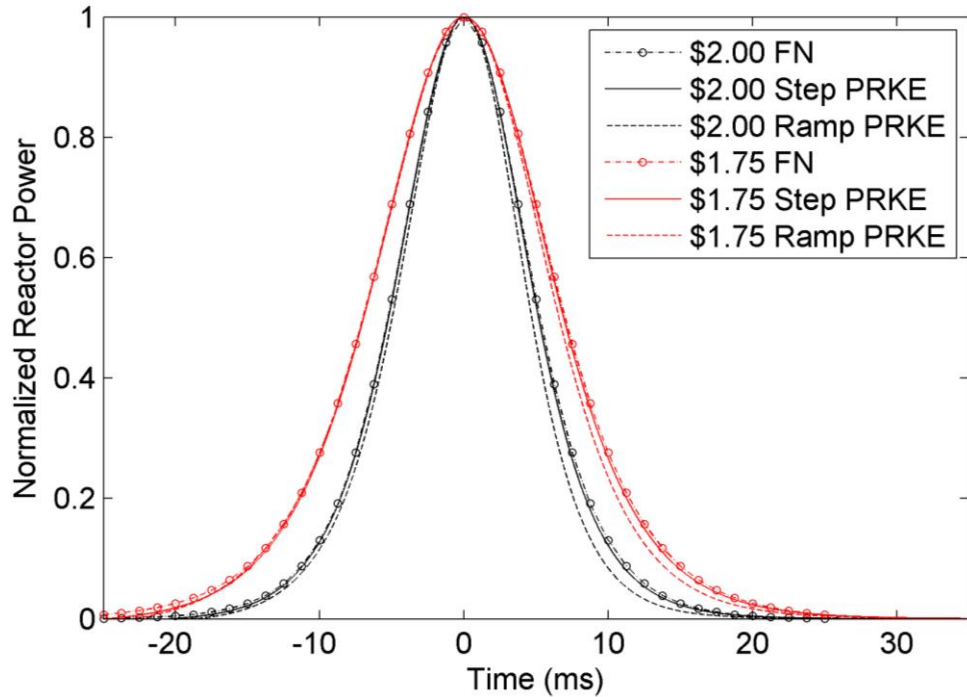


Figure 3-5. Comparison of PRKE solutions and FN models.

From Figure 3-5, the step PRKE solution and the FN model are nearly identical based on the declared temperature reactivity coefficient and heat capacity of the OSTR, shown in Table 3-1. The solution for the PRKEs with a ramped reactivity insertion represents the solution with the most realistic conditions to the OSTR during a pulse; however, the ramped reactivity insertion results in a slightly different profile for the two reactivity insertions. Several authors, including Scalettar [108], Wolfe [109], and Lewins [110] have investigated modifications to the FN model by expressing the temperature reactivity coefficient and heat capacity as a function of the temperature. In particular, Scalettar demonstrated the relation of maximum reactor power and total energy release during a pulse in comparison with the FN model by assuming a constant temperature reactivity coefficient and linearly varying heat capacity, though reactor power as a function of time; however, analytical expressions cannot be derived without knowledge of these parameters and their respective temperature dependence. The FN model predicts that the maximum power is scaled as $(\$-1)^2$ and total energy released (integrated power) is scaled as $(\$-1)$. In other words, if two

reactor pulses are compared, the ratio between the maximum power of the pulses is proportional to $(\$-1)^2$ and the total energy released is proportional to $(\$-1)$.

Recall that the objective of this research is to determine the reactor kinetics parameters as part of a safeguards inspection to independently measure these quantities. Based on (3-24), it is desirable to analyze the plots in Figure 3-5 in a way to determine the ω for each curve; for example, integration may be utilized to obtain an expression for ω .

$$I = \int_0^{\infty} FN(t) dt = \int_0^{\infty} \operatorname{sech}^2\left(\frac{\omega t}{2}\right) dt = \frac{2}{\omega} = \frac{2l}{\beta(\$-1)} \quad (3-26)$$

The numerical data are integrated beginning at the peak ($t = 0$) instead of the first data point ($t = -\infty$) to avoid integrating the baseline signal during the OSTR experimental phase of the research. Through integration of the data in Figure 3-5, a value for the ratio of β/l may be obtained with an expected dollar reactivity insertion in (3-27).

$$\frac{\beta}{l} = \frac{2}{I(\$-1)} \quad (3-27)$$

Additionally, the second derivative may be found to provide information at the peak of the reactor pulse. The second derivative of the FN model is given in (3-28).

$$D = \frac{1}{P_{\max}} \frac{d^2 P}{dt^2} = -\frac{\omega^2}{2} \left(\operatorname{sech}^4\left(\frac{\omega t}{2}\right) - 2 \operatorname{sech}^2\left(\frac{\omega t}{2}\right) \tanh^2\left(\frac{\omega t}{2}\right) \right) \quad (3-28)$$

The FN model assigns the value of $t = 0$ at the peak of the reactor pulse, shown in Figure 3-5, and at $t = 0$, (3-28) can be reduced to (3-29).

$$D = \frac{-\omega^2}{2} \quad (3-29)$$

and rearranged to calculate the ratio of β/l in (3-30).

$$\frac{\beta}{l} = \frac{(-2D)^{1/2}}{(\$-1)} \quad (3-30)$$

Table 3-2 presents the calculated β/l ratio for each curve presented in Figure 3-5. The theoretical FN model predicts a ratio of 336.28, equal to the β/l ratio from the OSTR

BOL values in Table 3-1. The PRKE model with step reactivity insertion calculates values close the FN model, but the ramped reactivity insertion cases are substantially different from theoretical values, which is readily observed from the pulse shapes in Figure 3-5. In fact, by utilizing the FN model to calculate the β/l ratio from a ramped reactivity insertion, the value is overestimated by about 12 percent for the \$2.00 pulse.

Table 3-2. Calculated β/l ratios for theoretical and numerical models

Reactivity Insertion	Model	β/l measurement using integration (3-27)	β/l measurement using 2 nd derivative (3-30)
\$1.75	FN	336.28	336.28
	Step PRKE	341.27	338.09
	Ramp PRKE	359.85	348.58
\$2.00	FN	336.28	336.28
	Step PRKE	342.44	339.44
	Ramp PRKE	378.25	367.75

Though the PRKE model with ramped reactivity insertion utilizes the most realistic conditions to OSTR pulses based on the BOL conditions in Table 3-1, the calculated β/l ratio is very different. However, it is proposed that an adjustment to the FN model based on empirical evidence in the OSTR produces an accurate calculation of the β/l ratio. Recall the form of the FN model in (3-24), which is found by assuming a constant value for the temperature reactivity coefficient and heat capacity. Though an analytical solution is not available by allowing these parameters to vary with temperature, an approximation may be found by assuming a novel, corrected form of the point reactor kinetics to be solved with the constant temperature reactivity coefficient and heat capacity, shown in (3-31).

$$\frac{dP}{dt} = \frac{\rho(t) - \beta}{l} P(t) \left(1 + H (\$ - 1)^2 \right) \quad (3-31)$$

where H is constant for a given reactor under identical conditions. H is multiplied by $(\$ - 1)^2$ due to, as stated earlier, the scaling of maximum reactor power as $(\$ - 1)^2$. Therefore, the approximation obtained by assuming the form in (3-31) for varying temperature feedback for reactivity and heat capacity should also be scaled by this value. When the form in (3-31) is solved identically to the FN model utilizing (3-22) and (3-23), the normalized, modified FN model is found to be

$$\frac{P(t)}{P_{\max}} = \operatorname{sech}^2 \left(\frac{\alpha t}{2} \left(1 + H (\$ - 1)^2 \right) \right) \quad (3-32)$$

Therefore, if (3-32) is solved for two reactor pulses under the same conditions with unique reactivity insertions, the value of H is the same for each reactor pulse, which allows for the independent calculation of the β/l ratio during the realistic case of a reactor pulse which contains a ramped reactivity insertion and temperature dependent feedback parameters. From (3-32), it is possible to formulate expressions for the β/l ratio based on the integral and 2nd derivative forms in the same manner as (3-27) and (3-30) by assuming that H maintains the same value for a particular reactor under identical conditions. If the integral of each curve is given for n th pulse, the integral and second derivative are shown in (3-33) and (3-34), respectively.

$$I_n = \int_0^\infty \frac{P_n(t)}{P_{\max}} dt = \frac{2l}{\beta (\$_n - 1) \left(1 + H (\$_n - 1)^2 \right)} \quad (3-33)$$

$$D_n = \frac{1}{P_{\max}} \left. \frac{d^2 P_n}{dt^2} \right|_{t=0} = \frac{-\beta^2 (\$_n - 1)^2}{2l^2} \left(1 + H (\$_n - 1)^2 \right)^2 \quad (3-34)$$

Which may be arranged for expressions of the β/l ratio based on the integral and 2nd derivative method in (3-35) and (3-36).

$$\frac{\beta}{l} = \left(\frac{1}{(\$_2 - 1)^2 - (\$_1 - 1)^2} \right) \left(\frac{2(\$_2 - 1)^2}{I_1 (\$_1 - 1)} - \frac{2(\$_1 - 1)^2}{I_2 (\$_2 - 1)} \right) \quad (3-35)$$

$$\frac{\beta}{l} = \left(\frac{1}{(\$_2 - 1)^2 - (\$_1 - 1)^2} \right) \left(\frac{2(\$_2 - 1)^2 (-2D_1)^{1/2}}{(\$_1 - 1)} - \frac{2(\$_1 - 1)^2 (-2D_2)^{1/2}}{(\$_2 - 1)} \right) \quad (3-36)$$

Table 3-3 provides the β/l ratio calculations based on the plots from Figure 3-5 utilizing (3-35) and (3-36). For each type of reactivity insertion in Figure 3-5, the two different values of reactivity insertion are used for the two pulses, denoted as subscripts 1 and 2. A comparison between Table 3-2 and Table 3-3 provides validity for the novel, proposed method for a solution of the PRKEs similar to the FN model, but utilizing the introduced factor, H , to account for temperature feedback parameters that would otherwise prevent the analytical solution of the PRKEs. In particular, excellent agreement is found for the ramped reactivity insertion case as compared to values in Table 3-2.

Table 3-3. Calculated β/l ratios for modified theoretical and numerical models

Selected data from Figure 3-5	β/l measurement using integration of two pulses (3-35)	β/l measurement using 2 nd derivative of two pulses (3-36)
FN	336.28	336.28
Step PRKE	339.75	338.63
Ramp PRKE	336.08	323.83

Analysis of experimental data from the OSTR utilizes the formulas in (3-35) and (3-36) to ascertain the ratio of the reactor kinetics parameters from two pulses. An uncertainty analysis of the method, found in Appendix C, shows that the calculated value can be found with low uncertainty depending on the reactivity insertion values chosen. During analysis, signal noise becomes important when assessing the uncertainty in the measurement with the formulas in (3-35) and (3-36). Differentiation acts as a high pass filter, so instrumentation noise is exaggerated during the calculation of the β/l ratio while integration acts as a low pass filter and is impacted less by inherent signal noise.

3.2.4 Reactor Square Waves

In contrast to reactor pulses, a square wave is a reactor transient in which the reactivity insertion is less than \$1.00, per the definition in (3-9). In a square wave, neutron precursors cannot be neglected, though an analytical solution may be found by assuming only one neutron precursor group, or a correction factor for an improved one-group model [111], which reduces (3-6) and (3-7) to (3-37) and (3-38) given as

$$\frac{dP}{dt} = \frac{\rho_0 - \beta}{\Lambda} P(t) + \lambda C(t) \quad (3-37)$$

and

$$\frac{dC}{dt} = \frac{\beta}{\Lambda} P(t) - \lambda C(t). \quad (3-38)$$

At the time of reactivity insertion, the solution assumes that the derivatives with respect to power and precursor concentration are equal to zero, resulting in an initial power increase followed by a steady power increase according to the steady reactor period. The solution to the PRKEs with a single delayed neutron group is shown fully developed as

$$\frac{P(t)}{P(t=0)} = \frac{\beta}{\beta - \rho} e^{\frac{\lambda\rho}{\beta-\rho}t} - \frac{\rho}{\beta - \rho} e^{\frac{\rho-\beta}{\Lambda}t}, \quad (3-39)$$

which is known as the prompt jump (PJ) approximation. The second exponential term represents the inverse of the initial reactor period, and can provide insight to the fissile material content in the reactor. Ultimately, the PJ approximation in (3-39) is limited to $\rho < \beta/2$, or a \$0.50 reactivity insertion [6], since a large reactivity insertion is accompanied by large temperature increases and subsequent physical feedback not accounted for in (3-39). Empirical evidence from the OSTR suggests that this limit for temperature feedback may be extended to approximately \$0.75. However, from the PJ approximation, it is possible to determine the reactor kinetics parameters, the delayed neutron fraction (β) and the prompt neutron lifetime (l), independently, which is discussed in detail in Section 6.1.4.

Figure 3-6 displays the difference exhibited by U-235 and Pu-239 reactor kinetics parameters in response to a \$0.50 reactivity insertion. In contrast to the pulses in Figure 3-5, the square waves are normalized to the initial reactor power rather than the maximum reactor power; and, in fact, the reactor power as a result of a square wave is many orders of magnitude less than a pulse and occurs over a much longer period of time. Figure 3-6 shows that for an identical, or compensated, reactivity insertion, the U-235 and Pu-239 are differentiated by the amount of time until the steady reactor period is achieved.

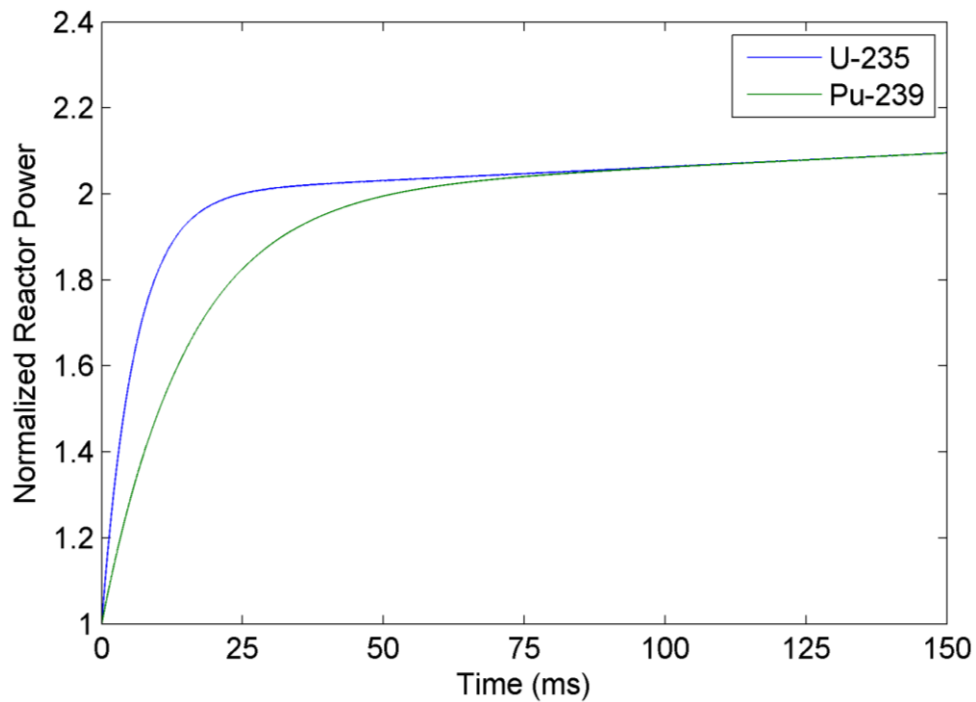


Figure 3-6. Comparison of \$0.50 reactivity insertion for U-235 and Pu-239

As with the reactor pulse, the reactor kinetics parameters do not constitute pure U-235 or Pu-239, but contain a mixture of the two that impacts the calculation of the delayed neutron fraction through (3-5). Calculation of the reactor kinetics parameters using square waves constitutes curve fitting the PJ approximation, formed in (3-39), of two separate reactivity insertions to ascertain the delayed neutron fraction, and through additional manipulation, the prompt neutron lifetime. However, this method is

hindered by two factors. In a square wave, the magnitude of the reactor power is much lower, increasing the signal-to-noise (S/N) ratio for any instrumentation, and the method of curve fitting is very sensitive to inherent noise in the instrumentation.

3.2.5 Reactor Kinetics Conclusions

The method of calculation of the reactor kinetics parameters is dependent on the type of reactivity insertion. The novel, modified form of the FN model proves successful when incorporating a ramped reactivity insertion and temperature dependent feedback for a reactor pulse, while curve fitting must be utilized for a square wave. The analysis of reactor pulses show that only the ratio of the kinetics parameters (β/l) may be calculated, which does not allow for the independent verification of the relative amount of fissile isotopes. Instead, the analysis of reactor pulses provides a proliferation-resistant method of verification for declared value of β/l , which is a requirement for any facility's safety analysis. However, independent quantification of the delayed neutron fraction and prompt neutron lifetime may be found with analysis of a set of square waves, though this might prove impractical during OSTR experiments due to lack of sufficient S/N ratio and inherent sensitivity in the method of analysis.

4 INSTRUMENTATION

As stated in Section 1.2, the objective of this research is to quantify the reactor kinetics parameters through measurement of Cherenkov light to support nonproliferation and safeguards programs. Therefore, instrumentation for the CRANK system must be chosen based on its ability to contribute to the overall goals. Experiments conducted at the OSTR provide results to validate the theoretical methodology proposed in Section 3.2. The following sections in this chapter will detail the instrumentation chosen and each instrument's contribution to the overall objective.

Table 4-1. List of CRANK System Components and Functions

Component	Function	Section
OSTR	Provide Cherenkov light for measurement with varying reactivity insertions	4.1
Photodiode (PD)	Convert light intensity to voltage signal during OSTR reactivity insertion	4.2
Fiber Bundle	Increase collection of photons by moving point of photon incidence closer to source without submerging PD in reactor pool	4.3
Lens	Increase collection of photons to increase S/N ratio	4.4
Data Acquisition System (DAS)	Record voltage signal from PD at a high rate to provide measurements for analysis	4.5
Programmable Light Source	Simulate OSTR light source in a desktop setting to provide insight to PD performance without OSTR testing	4.6

The instruments and equipment needed to perform experiments at OSTR are required to be robust while still maintaining a high resolution and data transfer rate.

4.1 Oregon State TRIGA Reactor

The OSTR is a Mark-II TRIGA reactor capable of steady-state power up to its license limit of 1.1 MW_{th}, with cooling provided by natural convection at atmospheric

pressure. The Mark-II design allows for in-core irradiation of samples, and it can also perform reactivity insertions up to administratively limited \$2.25 for pulsing operations resulting in peak power levels of approximately 2700 MW_{th} [112]. The reactor tank has an outside diameter of six and a half feet and is twenty and a half feet deep, and four beam ports penetrate the vessel, in addition to a graphite thermal column for sample irradiation. The core is located near the bottom of the reactor pool, shown in Figure 4-1 [112], with approximately sixteen feet of water between the core top and the reactor top. Due to the open pool design of the OSTR, the reactor top allows access to the reactor pool and line-of-sight to the reactor core.

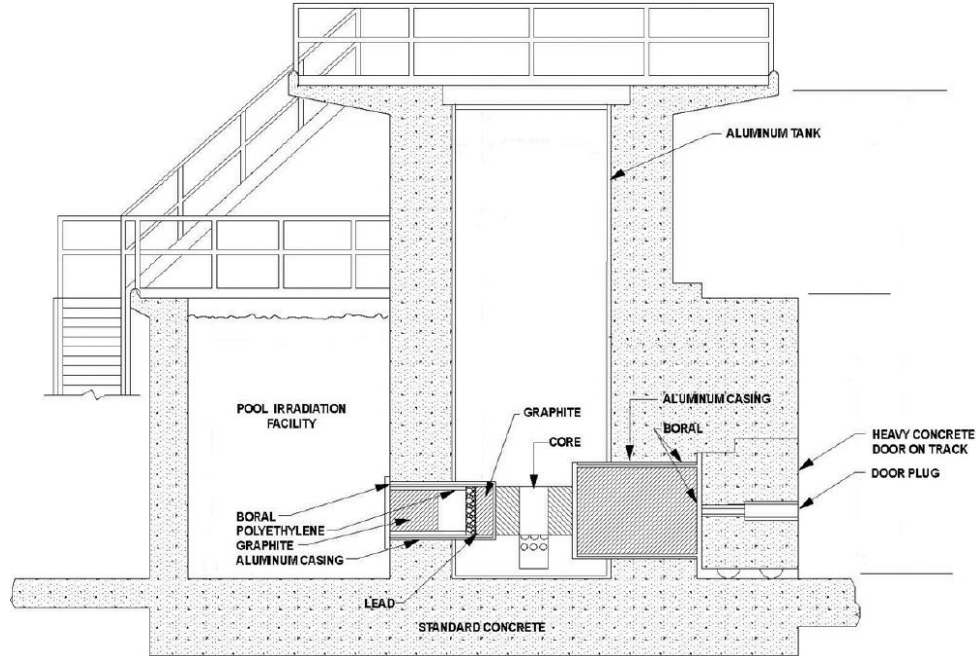


Figure 4-1. Vertical Section of OSTR

Figure 4-2 provides a closer view of the reactor core to provide understanding of the location of the control rods, power monitoring tools, and irradiation tubes within the reactor core [112]. The core is composed of seven rings of circular fuel elements with water acting as a moderator and coolant between the fuel elements. It is important to recall that Cherenkov light is produced by the *water* inside the OSTR reactor vessel,

though the charged particles, gamma rays, and neutrons that produce the radiation originate in the fuel or structural components depending on the type of interaction event. For the OSTR reactor core, Cherenkov light is predominantly produced in the spaces between fuel elements, or the fraction of the core that allows water to flow between core elements. Due to the physics involved with Cherenkov photons, the relatively small size of the reactor core, and the highly reflective surface of the reactor vessel, Cherenkov light is observable from any viewpoint at the top of the reactor during a reactivity transient.

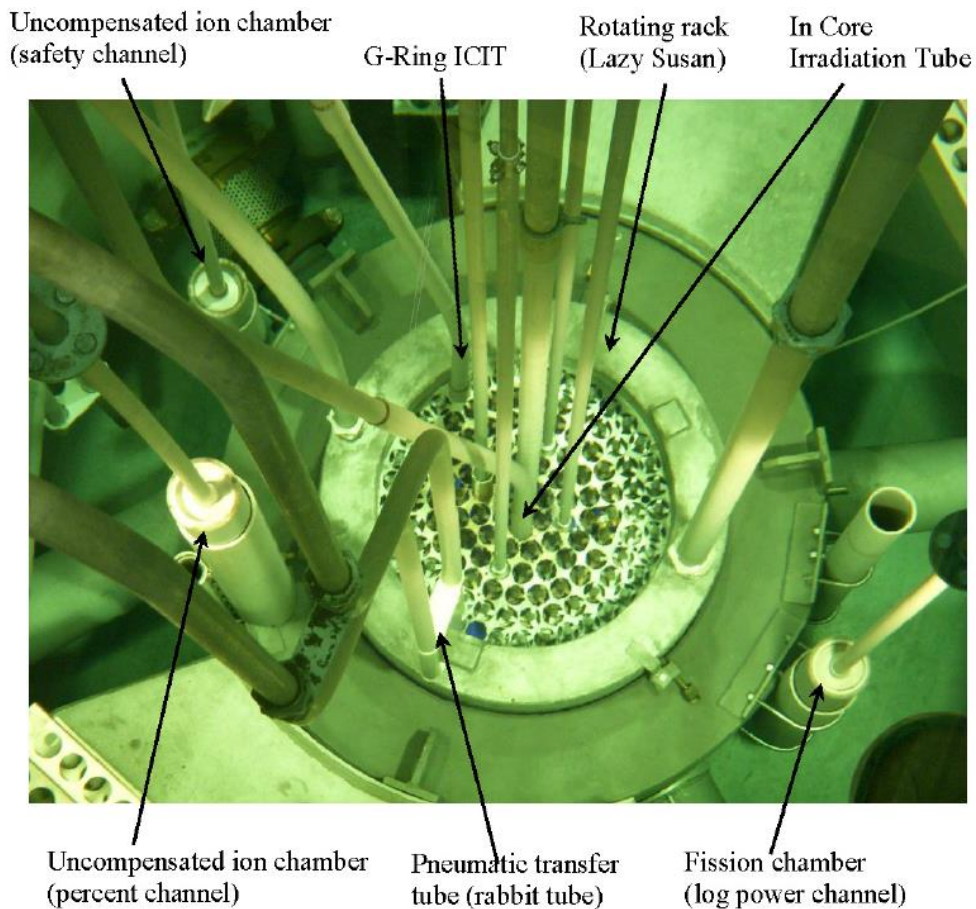


Figure 4-2. OSTR Core and Adjacent Equipment

The OSTR is utilized in this study as a source of Cherenkov light by performing specified reactivity insertions, and TRIGA reactors are ideal to perform reactivity perturbations due to the large negative feedback coefficient inherent to the reactor

[113]. The OSTR is capable of performing square waves and reactor pulses in normal operations, which result in abrupt changes in power level by pneumatically ejecting the transient control rod over a short amount of time, on the order of milliseconds.

Table 3-1 listed the reactor kinetics parameters of the OSTR from the FSAR. However, in a safeguards application, the CRANK system is required to provide the kinetics parameters, or kinetics parameters ratio, with an associated uncertainty to ascertain a confidence when determining material diversion activities. The OSTR FSAR [106] provides a 2σ uncertainty value, shown in Table 4-2, for each reactor kinetic parameters of interest in this research. Since the ratio of β/l is of interest in pulse analysis, it is pertinent to show the calculated value for the OSTR with associated uncertainty in (4-1), where the uncertainty in the β/l ratio is shown with the root mean square method [114].

$$\sigma_{\beta/l} = \left(\left(\frac{\partial \beta/l}{\partial \beta} \sigma_\beta \right)^2 + \left(\frac{\partial \beta/l}{\partial l} \sigma_l \right)^2 \right)^{1/2} \quad (4-1)$$

Table 4-2. Associated Uncertainty in β/l ratio

Specified Time in Fuel Cycle	β/l Ratio and approx. percent uncertainty (2σ)
Beginning of Life (BOL)	$336.28 \pm 43.38 (\approx 12.9\%)$
Middle of Life (MOL)	$384.21 \pm 39.84 (\approx 10.4\%)$
End of Life (EOL)	$244.30 \pm 22.52 (\approx 9.2\%)$

As can be seen, the uncertainty in the declared values of the FSAR is around 10 percent for each specified time in the OSTR's fuel cycle. Though this does not pose a threat to the safety of the core for day-to-day operations, the uncertainty has a large impact on the pulse shape for the purpose of the experiments conducted throughout this research. As of January 2017, the OSTR core is approximately 9 years old. With a standard core life of 70 years, it is anticipated that the reactor kinetics parameters

during OSTR experiments are nearly identical to the declared values at BOL. The desktop light source needs to be able to produce light in this fashion for the preliminary tests.

4.2 Photodiodes

Design of the CRANK system for a safeguards application requires simple, off-the-shelf instrumentation for the measurement of Cherenkov light, and from Figure 3-2, the chosen detector is required to have a high quantum efficiency and response to UV and low-wavelength visible light. The CRANK system does not implement a filter or other wavelength-shifting mechanisms in an attempt to isolate a single wavelength interval. Instead, the total intensity of Cherenkov light is measured based on the prior advancements in the field for both reactor and spent fuel applications discussed in Section 2.1.

A photomultiplier tube (PMT) is a typical device used for the detection of light, but it possesses some disadvantages that make it less desirable for use in testing at OSTR. However, a photodiode (PD) is a simpler instrument than a PMT, which allows it to be a better option for this research. Table 4-3 provides a comparison of PD and PMT characteristics, with desirable characteristics highlighted in green. Though PMTs have a high S/N ratio and a large active area, they require high voltage power supplies. In comparison, PDs have a relatively low S/N ratio, but are robust and do not require a high voltage power supply. Acquisition of a PD with a coupled amplifier reduces the S/N ratio by increasing the voltage output without high voltage power supply. Additionally, the introduction of a fiber bundle and optical lens, discussed in Section 4.3 and Section 4.4, respectively, allows for a greater active area at a closer distance to the OSTR source of Cherenkov light for the CRANK system.

Table 4-3. Comparison of PD and PMT characteristics

Phenomenon	PD	PMT
Signal to Noise (S/N) Ratio	Low	High
Active Area	Small (Medium w/ Lens)	Large
Voltage Output	Low	High
Damage from Saturation?	No	Yes
High Voltage Required	No	Yes

Based on recommendations from staff at Idaho National Laboratory, the PDA25K photodiode, displayed in Figure 4-3 (left), is chosen as the instrument to measure the Cherenkov light in the OSTR. The PDA25K is a GaP photodiode with a built in preamplifier (known as a DET25K without the preamplifier), and it is sensitive to wavelengths in the low visible (blue) and UV range in the spectrum, as shown in Figure 4-3 (right) [115], where the transition from UV to visible light occurs at a wavelength of approximately 400 nanometers. The active area of the photodiode is a 2.2 millimeter x 2.2 millimeter surface on the front of the detector.

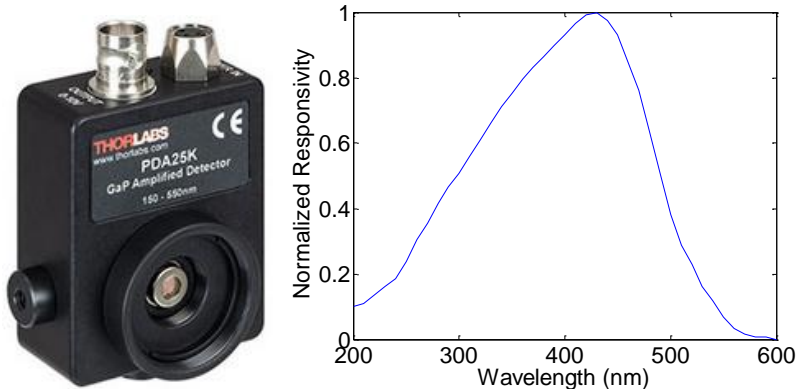


Figure 4-3: PDA25K GaP Photodiode

A comparison of the PDA25K photodiode responsivity (blue) [115] to the Cherenkov light spectrum (red) [91] from Figure 3-2 is provided in Figure 4-4, with the product of the two curves shown in black to provide the spectral detection of the CRANK system. It can be observed that there exists good agreement between PDA25K

photodiode and the Cherenkov photon intensity from Figure 3-2 [91]. An ideal PD's responsivity would be uniform throughout the wavelengths of the Cherenkov spectrum; however, the PDA25K has the best available responsivity to low wavelength light for readily available, off-the-shelf instrumentation.

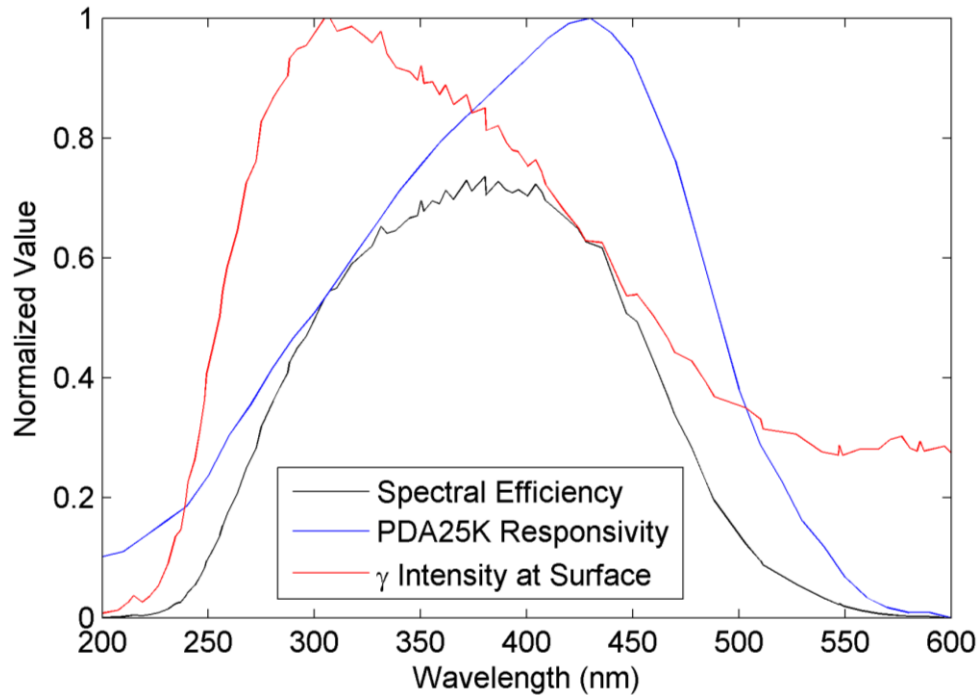


Figure 4-4. Comparison of PD Responsivity and Cherenkov spectrum

The PDA25K possesses a very fast rise time (approximately one nanosecond), but the inclusion of the amplifier increases the rise time response (t_r) of the photodiode with increased amplification. The PDA25K photodiode possesses an internal amplifier from 0 to 70 decibels (dB) in 10 dB steps. Altering the amplifier gain changes the photodiode output voltage, bandwidth of the signal, root mean square (RMS) signal noise, and voltage offset, shown in Table 4-4. The bandwidth decreases with increasing gain due to the time constant of the amplifier circuit. The cutoff frequency is defined as the frequency at which photodiode output decreases by 3 dB relative to the maximum photodiode output, roughly approximated through the relation in (4-2) [116].

$$t_r = \frac{0.35}{f_{BW}} \quad (4-2)$$

where f_{BW} is the frequency bandwidth in hertz, which differs for a given photodiode at a specified amplification gain. The published values of f_{BW} for the PDA25K are provided in Table 4-4 for varying amplifier gain, and for example, the rise time associated with the highest amplification of 70 dB is approximately 100 microseconds, per (4-2).

Table 4-4. PDA25K Gain Specifications

Gain (dB)	Relative Gain to 0 dB	Bandwidth	Noise (RMS) (μ V)	Offset (mV)
0	1	7.5 MHz	350	± 5 (max 10)
10	3.162	3.3 MHz	290	± 6 (max 12)
20	10	1.0 MHz	260	± 6 (max 15)
30	31.62	300 kHz	245	± 8 (max 15)
40	100	100 kHz	325	± 10 (max 20)
50	316.2	32 kHz	500	± 15 (max 40)
60	1,000	11 kHz	675	± 20 (max 75)
70	3,162	3.3 kHz	900	± 40 (max 200)

The PDA25K provides a 0-10 volt (V) signal to the data acquisition system. Since previous research has shown that Cherenkov light intensity is proportional to reactor power, when the PD is operated in a light environment that results in a linear response, the PD voltage is representative of proportional reactor power.

4.3 Fiber Bundle

For OSTR experiments, the PD is not submerged in the reactor pool above the core. Instead, the Thorlabs BF20HSMA01 fiber bundle [117] is connected to the SMA port adapter on the front of the Thorlabs PDA25K detector. The chosen fiber bundle is waterproof and is positioned in the reactor pool with line of sight to the reactor core. As Cherenkov light is produced in the OSTR during a reactivity insertion, some light

enters the fiber bundle and is channeled up the fibers through internal reflection until it reaches the PDA25K, producing a voltage signal. Figure 4-5 provides an image of the chosen fiber bundle from Thorlabs, with a detailed view in Figure 4-6 illustrating the 7-fiber design of the fiber bundle. The effective light area is approximately 56 percent of the full cross-sectional area of the fiber bundle.



Figure 4-5. Thorlabs BF20HSMA01 fiber bundle



Figure 4-6. Thorlabs BF20HSMA01 fiber design with 7 separate fibers

The fiber bundle increases the Cherenkov light intensity incident on the PD by extending the point of light collection closer towards the OSTR and increasing the PD output voltage without submerging the CRANK system's electronic components. Characteristics of the fiber bundle are found in Table 4-5, with the corresponding approximate light loss due to attenuation reported from Thorlabs specifications [117].

Figure 4-7 displays the attenuation of light in the fiber bundle as a function of wavelength in dB/kilometer of fiber for the Thorlabs BF20HSMA01, which is of the High-OH type [117]. For the approximate Cherenkov light wavelength of 300 nanometers, this translates to an approximate loss of -0.15 dB/meter of fiber length, or an approximate loss 3.4 percent of the original light intensity, which is good transmission rate compared to other off-the-shelf fiber bundles.

Table 4-5. Characteristics of Thorlabs BF20HSMA01 fiber bundle

Cable type	Diameter (mm)	Effective Light Area (mm ²)	Loss at 300 nm (dB/m)
Bare Fiber Bundle	2.0	1.663 (56% full area)	-0.15

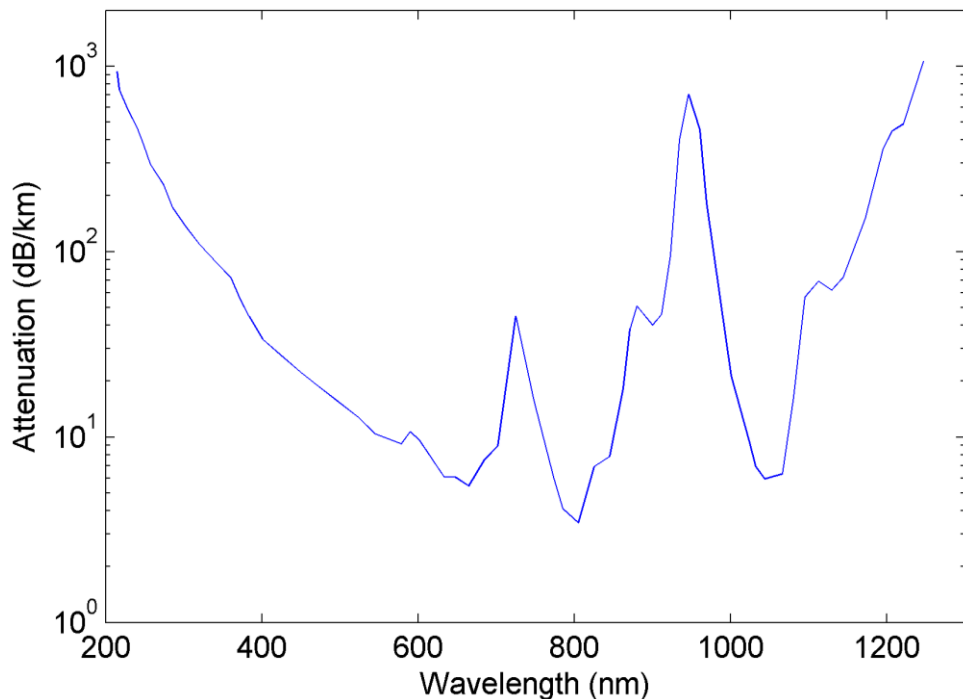


Figure 4-7. Multimode Fiber Attenuation for Thorlabs BF20HSMA01

For OSTR experiments after March 2016, a custom four meter version of the Thorlabs BF20HSMA01 fiber bundle was purchased from Thorlabs to further extend the collection closer to the OSTR to increase the Cherenkov light intensity measured by the PDA25K. From estimations of the solid angle from [118], the change from the

off-the-shelf one meter fiber bundle to the custom four meter fiber bundle results in a 7.4 magnitude increase in photon intensity.

4.4 Optical Lens

From the discussion in Section 4.2 and Table 4-3, one of the most important disadvantages for a PD as compared to a PMT was the magnitude of the active area. Typically, PDs are very small; therefore, to increase the PD voltage output in response to Cherenkov light produced during a reactor transient, it is desirable to increase the number of Cherenkov light photons incident on the PD. As described in Section 4.3, a fiber bundle is submerged into the reactor pool and is connected to the PDA25K. Two lenses were evaluated for use in OSTR experiments: the Thorlabs F810SMA-543 [119] collimator and the Ocean Optics Col-UV-30 lens [120], shown in Figure 4-8 and Figure 4-9, respectively. Each lens is equipped with an SMA connection allowing for direct connection to the submerged end of the Thorlabs BF20HSMA01 fiber bundle.



Figure 4-8. Thorlabs F810SMA-543 collimator

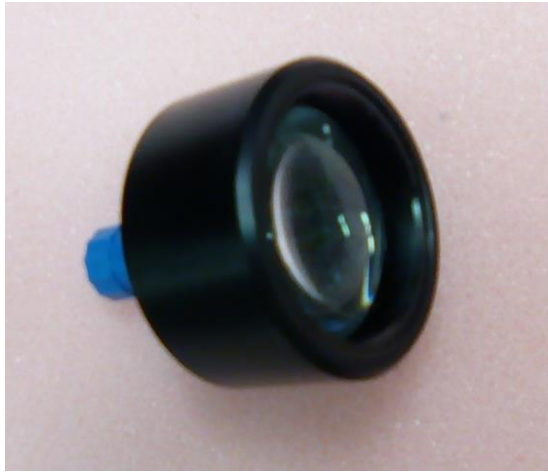


Figure 4-9. Ocean Optics COL-UV-30 collimating lens

The Thorlabs F810 SMA-543 collimator has an outer diameter of 17.5 millimeters and consists of a dense flint glass called N-SF6. As can be observed in Figure 4-10 (blue), the transmission percentage of N-SF6 in the wavelengths of interest for Cherenkov light (~300 nm) is very low [119], causing a sharply reduced voltage signal from the PDA25K. In contrast, the Ocean Optics COL-UV-30 collimating lens has an outer diameter of 27.5 millimeters and is composed of fused silica, called Suprasil. The transmission percentage of Suprasil [121], shown in Figure 4-10 (green), is much greater than N-SF6 at the peak Cherenkov wavelength of 310 nm, making it the best off-the-shelf option for an optical lens for the CRANK system.

The Ocean Optics lens has a published field-of-view of approximately 25 degrees with a 30 millimeter focal length [120]. From Section 4.3, the two separate lengths of the Thorlabs BF20HSMA01 fiber bundle can potentially be used in OSTR experiments of the CRANK system. The one meter fiber bundle causes the optical lens to be submerged approximately 189 inches above the reactor core while the four meter cable results in the optical lens to be approximately 70.5 inches above the reactor core. The published field-of-view and focal length for the Ocean Optic lens allows the entire top surface of the reactor core to be observed from either position, shown in Table 4-6, where the field of view is found by the tangent of the field-of-view angle and is greater than the core diameter in both cases.

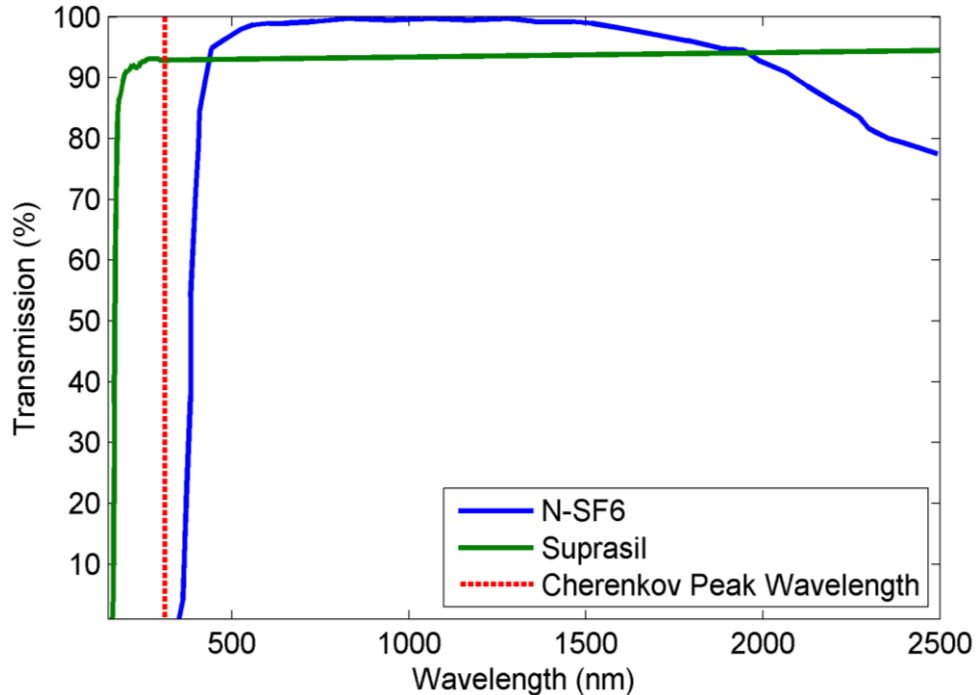


Figure 4-10. Transmission percentage of N-SF6 and Suprasil glass

Table 4-6. Comparison of FOV for Thorlabs collimator and Ocean Optics lens

Cable type	Focal Length (mm)	Diameter of reactor core (inches)	Field of View radius at higher position (inches)	Field of View radius at lower position (inches)
Ocean Optics Lens	30	21	88.1	32.9

4.5 Data Acquisition System

The Thorlabs PDA25K is connected to the DAS with a simple coaxial BNC cable to record voltage signals during the reactivity insertion. Due to the short duration of reactivity transient for pulses and square waves, the DAS is required to possess a sufficient sample rate with ample resolution to satisfy the mathematical analyses techniques proposed in Section 3.2 to identify discrepancies in fissile material content. The chosen data acquisition system consists of National Instruments (NI) hardware, including a NI PXIe (Peripheral component interconnect eXtensions for

Instrumentation Express) chassis and digital oscilloscope. The NI-5171R digital oscilloscope, shown in Figure 4-11, is a voltage or current input module with a voltage limit of 0-5V and is a high precision reconfigurable oscilloscope module with a maximum acquisition rate of 250 million samples per second (250 MHz) [122], which is sufficient for the time scales observed during OSTR reactivity insertions. The NI-5171R is connected to the NI PXIe-1085 chassis, shown in Figure 4-12 with sample modules, which can transfer data up to a rate of 24 gigabytes per second (GB/s) and has the capacity for up to 18 separate modules [123].



Figure 4-11. NI PXIe-5171R digital oscilloscope

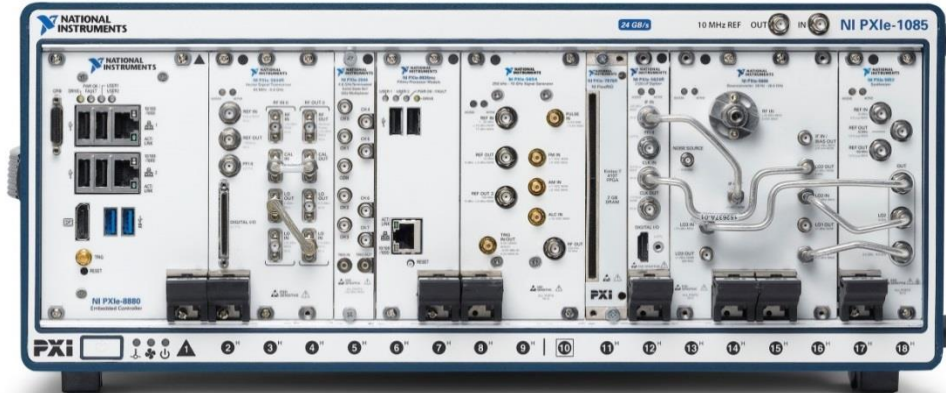


Figure 4-12. NI PXIe-1085 chassis with sample modules

4.6 Programmable Light Source

Prior to OSTR experiments, it is desirable to characterize the PD response to incident light in a desktop, preliminary environment without including many of the complications associated with OSTR experiments. A light emitting diode (LED) light source is used to simulate the Cherenkov light output in the OSTR. The Thorlabs M365FP1 LED light source possesses a nominal wavelength of 365 nanometers with a maximum input current of 1400 mA [124]. Ideally, the wavelength spectrum of the Thorlabs M365FP1 LED light source would mimic the Cherenkov light spectrum. However, for readily available off-the-shelf instrumentation, the Thorlabs M365FP1 LED light source provides the closest approximation to the Cherenkov light spectrum. Figure 4-13 provides a comparison of the Cherenkov light spectrum (red) and PDA25K responsivity (blue) curves from Figure 4-4 including the LED light source spectrum (black). As can be observed, the M365FP1 is very similar to the wavelengths of interest to the CRANK system during OSTR experiments.

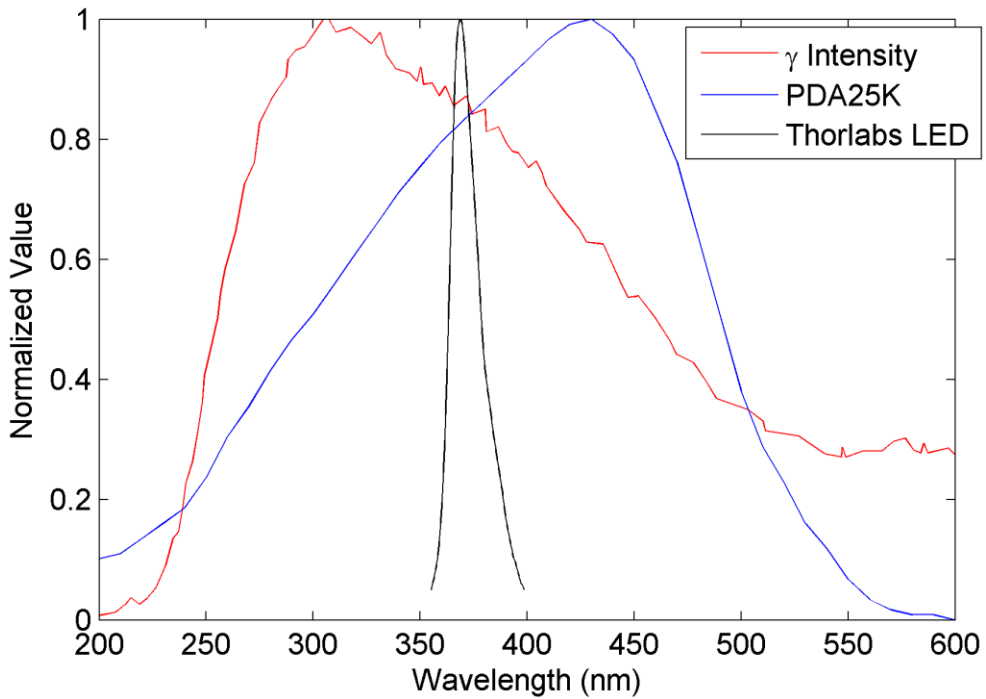


Figure 4-13. Comparison of PD, LED, and Cherenkov spectrums

To vary the supplied current, and therefore light output, of the Thorlabs M365FP1 light source, an NI PXIe-4322 analog output module, located within the NI PXIe-1085 chassis is used to provide a current output from 0 to 20 millamps (mA) to the Thorlabs M365FP1 LED light source. The NI PXIe-4322 can produce samples at 250,000 samples per second (kS/s) and is controlled with NI LabVIEW software to mimic the light output of the OSTR Cherenkov light intensity during a square wave or reactor pulse transient. It was shown that a 20 mA current applied to the M365FP1 produces enough light to saturate the PDA25K photodiode at a gain of 50 dB or greater, which demonstrates the ability of the system to represent all potential light intensities produced by the OSTR from null to saturation.

4.7 Instrumentation Conclusions

The CRANK system is assembled with the components in Section 4 to measure the Cherenkov light intensity during a reactivity insertion. Figure 4-14 presents the

CRANK system, with all major components labeled, during a layout of equipment prior to an experiment being conducted in OSTR. The complete system is compact, robust, and simple, drastically increasing its value in a potential safeguards application.

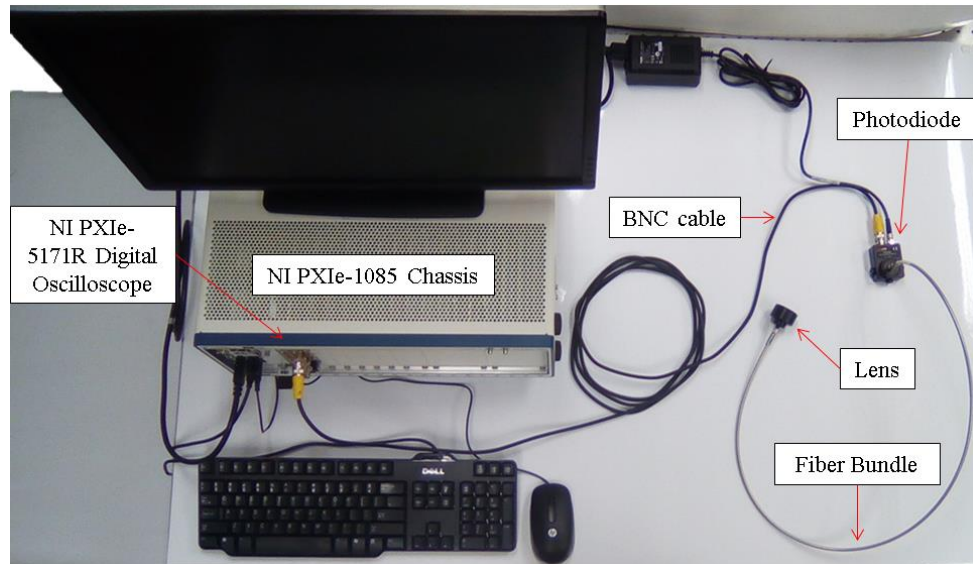


Figure 4-14. Layout of CRANK system components

A pictorial representation of the complete experimental set-up for OSTR experiments is provided in Figure 4-15 and Figure 4-16. The Thorlabs PDA25K photodiode is positioned next to the reactor control rod housing and attached with zip-ties to maintain its position during the reactor transient. The PD is connected to the NI DAS with a BNC cable, and the NI-5171R digital oscilloscope records the voltage output at 250 MHz. The PD receives light channeled from the custom, four meter Thorlabs BF20HSMA01 fiber bundle is submerged in the reactor pool with the Ocean Optics COL-UV-30 collimating lens connected to the end. During OSTR experiments, with the four meter fiber bundle, the lens is approximately six feet above the core, which is approximately 16 feet under the water surface.

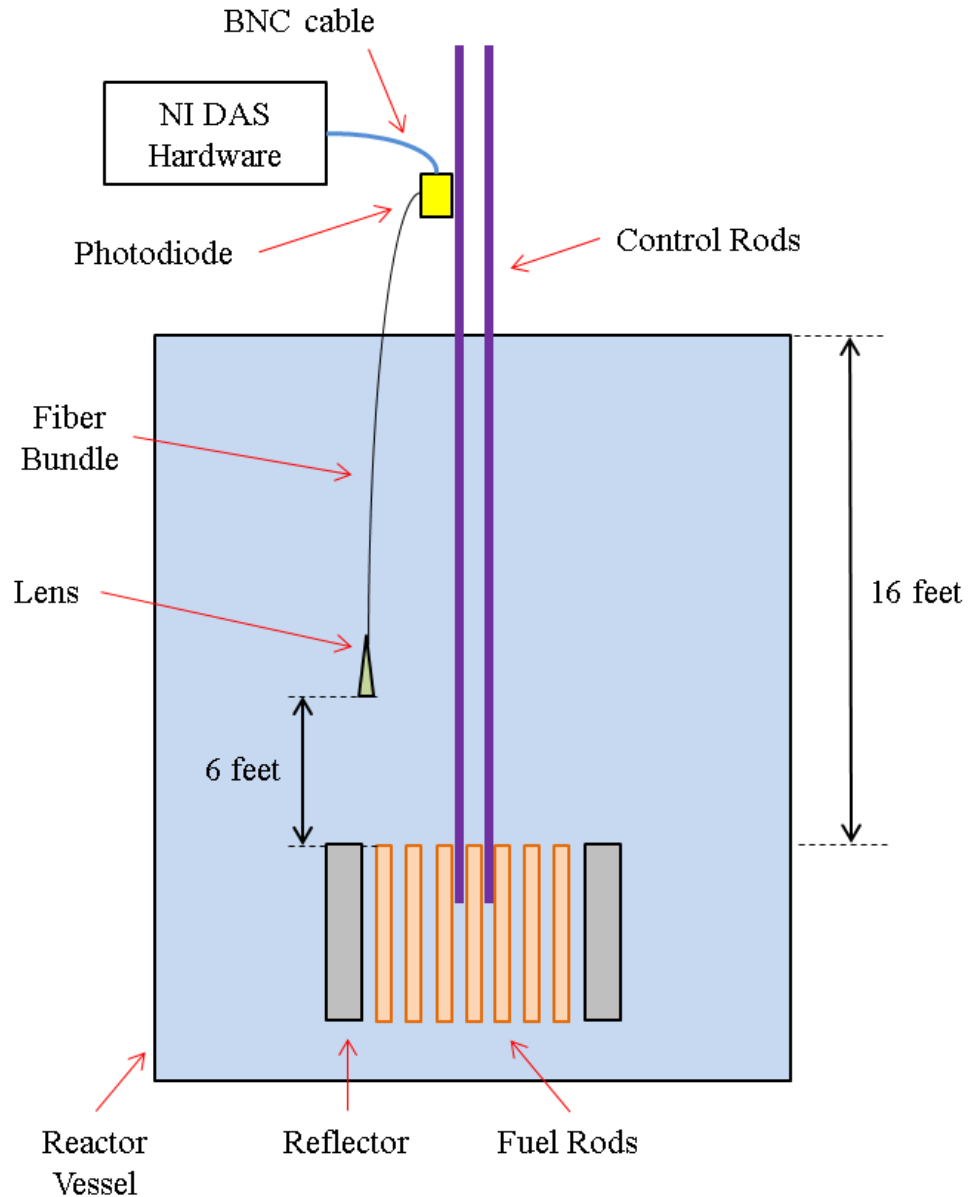


Figure 4-15. Horizontal section view of CRANK system setup at OSTR

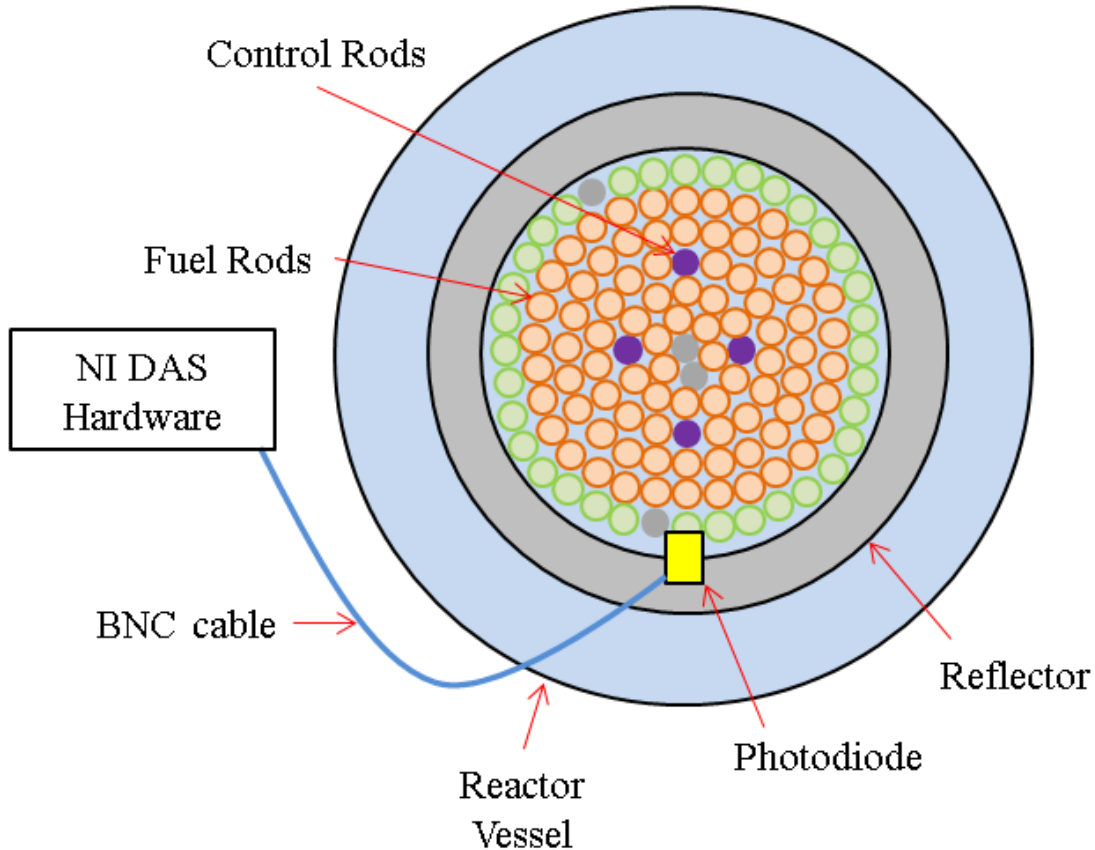


Figure 4-16. Vertical section view of CRANK system setup at OSTR

It can be observed from Figure 4-15, Figure 4-16, and the discussion in Section 4.4, the CRANK system cannot be simply submerged directly above the OSTR core due to instrumentation housings and irradiation tubes. Instead, the fiber bundle is positioned offset approximately 14 inches from the center of the core with the optical lens face parallel to the top of the reactor core. However, the large field-of-view for the optical lens detailed in Table 4-6 and the high reflectivity of all OSTR components, the CRANK system maintains the ability to observe Cherenkov light during reactivity insertions during OSTR experiments.

5 EXPERIMENTAL METHODS

The CRANK system components, detailed in Section 4, are assembled in a novel configuration to determine reactor kinetics parameters with off-the-shelf instrumentation in a specific methodology and procedure to analyze results in a repeatable manner. The methods for the desktop and OSTR experiments differ based on the applicable instrumentation for each case.

5.1 Desktop Experiments

Desktop experiments are performed in a controlled, laboratory setting to investigate phenomena that might impact the final declarations of reactor kinetics parameters when measured with the CRANK system. Prior to desktop experiments that simulate an OSTR reactivity insertion, it is necessary to determine the PDA25K response to varying light intensity as a function of the amplification gain setting. Photodiode calibration was performed with the Thorlabs M365FP1 LED light source, detailed in Section 4.6, with the LED's light intensity controlled by the current applied by the NI PXIe-4322 analog output module. The analog output module is controlled by NI LabVIEW virtual instrument (VI) to operate at a steady value for 10 seconds to obtain a reduced uncertainty for each value of PD response. The PD response during the 10 seconds is averaged to obtain the photodiode response in volts with associated uncertainty as a function of applied current, shown in Figure 5-1 for an amplification gain of 70 dB. Additional response curves for varied amplification gain are found in Appendix A. A preliminary OSTR reactivity insertion was performed to obtain the PDA25K output voltage during a maximum OSTR reactivity insertion of \$2.00, which equates to approximately 1.6 mA applied to the Thorlabs M365FP1 LED light source.

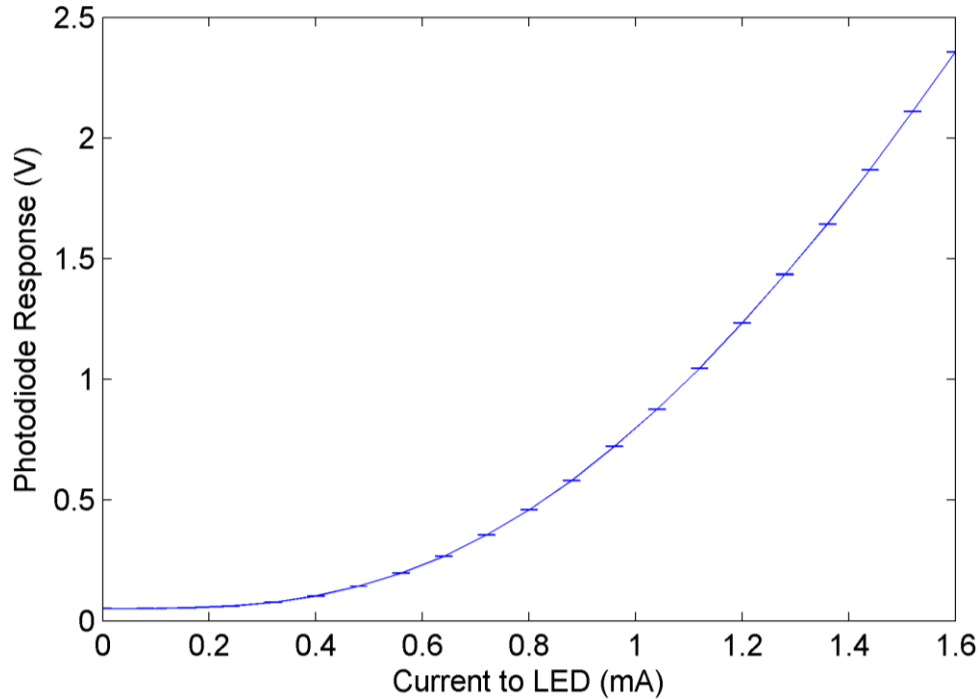


Figure 5-1. PDA25K response to steady state current with error bars

Recall from Section 2 that previous investigations have shown that Cherenkov light intensity is proportional to reactor power. Therefore, for analysis of reactivity insertions, it is desirable for the PD to possess a linear response to the light intensity. However, Figure 5-1 does not display a linear response of the Thorlabs PDA25K in response to programmed current from the NI PXIe-4322. Specifications of the PDA25K indicate that nonlinearity of the signal, as observed in Figure 5-1 should not occur in the predicted region of light intensity.

Upon request, Thorlabs, Inc. provided the M365FP1 LED light source output as a function of supplied current from a controller. Typically, the M365FP1 LED light source is operated at a maximum level of 1400 mA, much greater than the light intensity anticipated in the OSTR. Though the Thorlabs M365FP1 LED light source provides a linear output with supplied current at high values of current, Figure 5-2 provides the LED optical power (light intensity) as a function of supplied current at very low values of current typical of those used with the CRANK system during the

desktop experiment phase of development. Figure 5-3 combines the ordinate axes of Figure 5-1 and Figure 5-2 to provide the Thorlabs PDA25K response as a function of LED optical power, which does display a linear trend as desired.

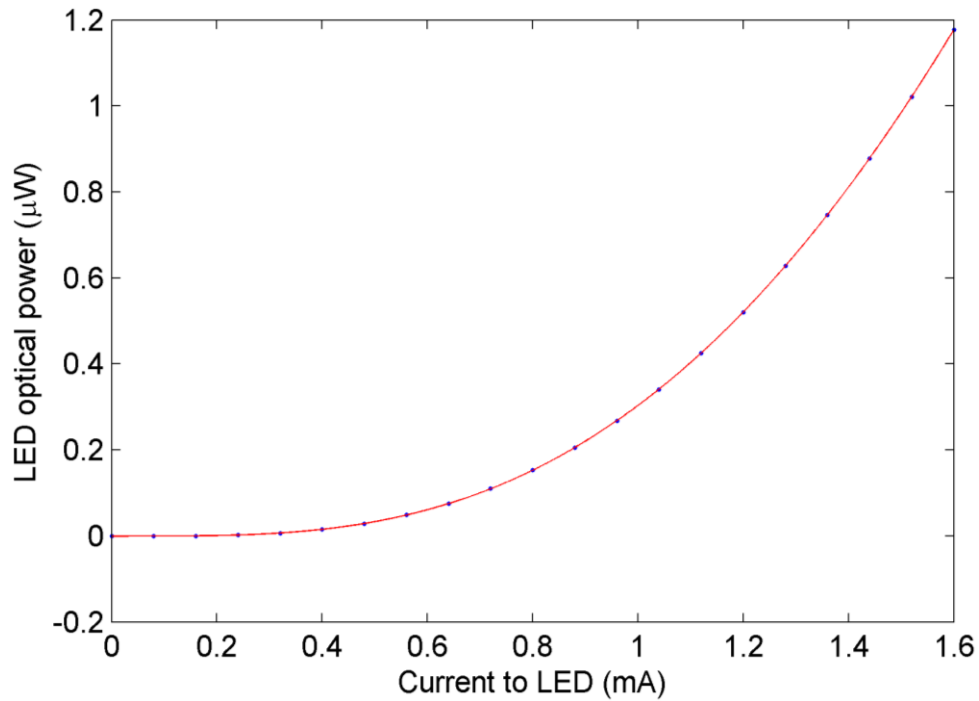


Figure 5-2. M365FP1 output as function of supplied current

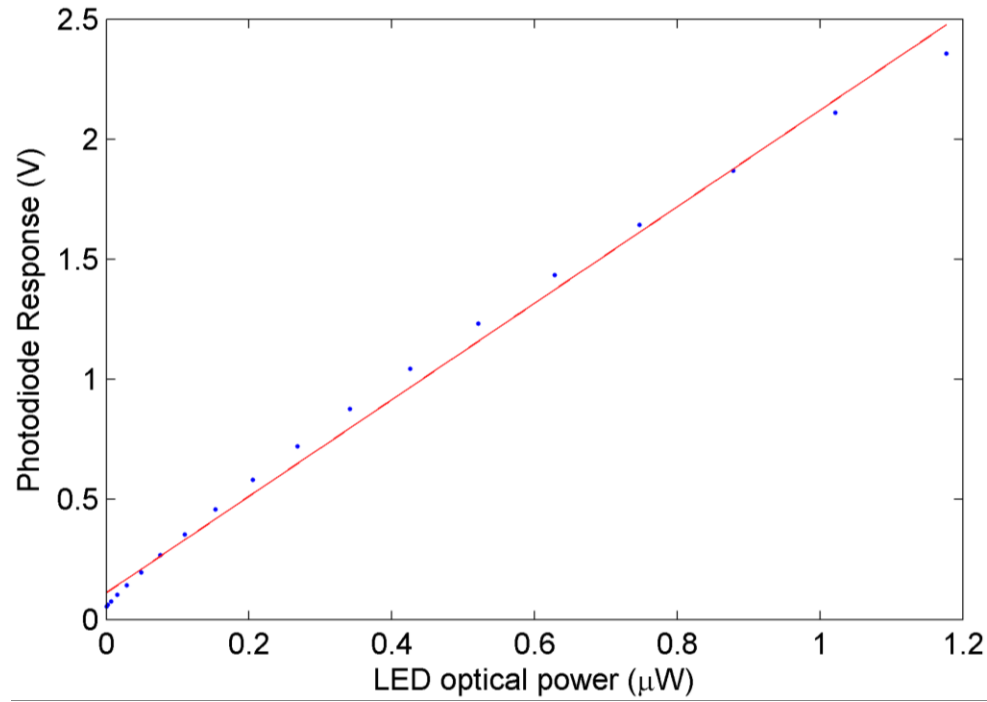


Figure 5-3. PDA25K response as a function of M365FP1 light intensity

For desktop transient tests, the Thorlabs BF20HSMA01 fiber bundle is directly connected to the SMA ports on the Thorlabs PDA25K photodiode and the Thorlabs M365FP1 LED light source to avoid background light contamination.

5.2 OSTR Experiments

OSTR experiments are performed to mimic the proposed format of a safeguards inspection to ascertain reactor kinetics parameters in a reactor facility with minimal reliance on facility operations, with unknown reactor kinetics parameters, and without comparison against a standard, which is typical of many safeguards techniques. OSTR experiments provide a series of proof-of-concept tests, so that the values of the reactor kinetics parameters measured with the CRANK system during OSTR experiments are compared with FSAR values [106], since the OSTR is a known reactor without ambitions for unintended material diversion.

For each method proposed in Section 3.2, two reactivity insertions are required to determine the reactor kinetics parameters ratio with reactor pulses or the individual reactor kinetics parameters with square waves. OSTR experiments are performed in OSTR per the depiction in Figure 4-15 with the components discussed in Section 4.

A standard set of documents for a reactor facility is the control rod worth tables. The control rods are calibrated per a standard schedule (the OSTR is once per year) to determine the reactivity of the reactor as a function of each rod's individual position, deemed the control rod worth. These values are usually in the form of dollars, per the definition in (3-9). As the reactor operates between control rod calibrations, the reactivity of the control rods is altered due to fissile material burnup and fission product accumulation. Ideally, a safeguards inspection employing the CRANK system should take place shortly following the reactor facility's control rod calibration, since this is when the reactivity values of the control rods are most accurate. The CRANK system requires two reactivity insertions to be performed by the reactor operators, and should follow a procedure similar to that provided below.

1. Assemble CRANK system on reactor top at reactor facility.
2. Ensure that:
 - a. NI LabVIEW software or equivalent is properly operating.
 - b. Fiber bundle and lens have unobstructed view of reactor core.
3. Determine the value of two reactivity insertions to be performed.
4. Specify dollar value of first reactivity insertion to be performed.
5. Record data during first reactivity insertion for appropriate amount of time.
6. Wait appropriate amount of time for reactor to return to a stable, critical condition.
7. Specify dollar value of second reactivity insertion to be performed.
8. Record data during second reactivity insertion for appropriate amount of time.

9. Utilizing the recorded measurements, perform the desired analysis to determine reactor kinetics parameters based on (3-35) or (3-36) for reactor pulses or curve fitting for square waves.

Based on experience gained through OSTR experiments, several items in the list should be performed with the following suggestions:

- With respect to step #3, it is desired to perform the smaller reactivity insertion prior to the larger reactivity insertion to avoid large temperature or fission product buildup.
- With respect to step #5 and step #7, the appropriate time to record data is dependent on the magnitude of the reactivity insertion. For a \$2.00 pulse, recording for 40 milliseconds is appropriate. However, a \$0.50 square wave would require approximately 150-250 milliseconds of data to be recorded.
- With respect to step #6, the appropriate waiting period for OSTR reactivity insertions is approximately fifteen minutes. However, it was shown that extending the waiting period can greatly benefit the analysis of the reactor transients to reduce the error associated with control rod worth.

6 RESULTS AND OBSERVATIONS

The majority of the work performed as part of this research consists of design and implementation of the CRANK system, as well as analysis of experimental data in support of the intended safeguards application. Desktop experiments provide a mechanism to investigate phenomena that could provide ambiguity in OSTR experiments and allows for the identification of potential solutions. Finally, experiments utilizing the OSTR and procedural methodology outlined in Section 5.2 allow for the calculation of the reactor kinetics parameters.

6.1 Desktop Experiments

Since several phenomena are expected to affect the outcomes of the CRANK system, desktop experiments are conducted to assess the photodiode's response due to:

- Background light contamination,
- Sensitivity to angular offset and stand-off distance, and
- Rapid light increase characteristic of research reactor transient.

Each of these characteristics impacts the CRANK system's ability to detect fissile material diversion in a research reactor, and desktop experiments can investigate each parameter independently.

6.1.1 Background Light Contamination

Background light contamination is controlled by implementing a black enclosure box, with small slits cut for power and signal connections, shown in Figure 6-1. Preliminary tests assess photodiode response under background light contamination from overhead, fluorescent laboratory lights, with identical tests repeated with the enclosure box to eliminate background light contamination. A “lights on” condition specifies that no enclosure box is included, and the laboratory lights remain on, while a “covered” condition specifies that the enclosure is placed over the experimental set-up, creating a dark environment. Comparison of the PD signal for inclusion or exclusion of the enclosure box is found in Figure 6-3.



Figure 6-1. Enclosure box for preliminary desktop experiments

6.1.2 *Angular Offset and Stand-off Distance*

The angular offset and stand-off distance of the photodiode with respect to a light source position impacts the total number of incident photons on the PDA25K's detector surface, and therefore affect the voltage output. Figure 6-2 illustrates the use of a letter system to record the position of the photodiode and LED light source, with single- and double-lettered positions describing rows and columns of breadboard positions of one-inch offset bolt holes around the LED light source, for an array of distances from 2 to 12 inches (A-K) at 1 inch intervals along the axis of incident light and 0 to 6 inches (AA-GG) at 1 inch intervals normal to the axis of incident light.

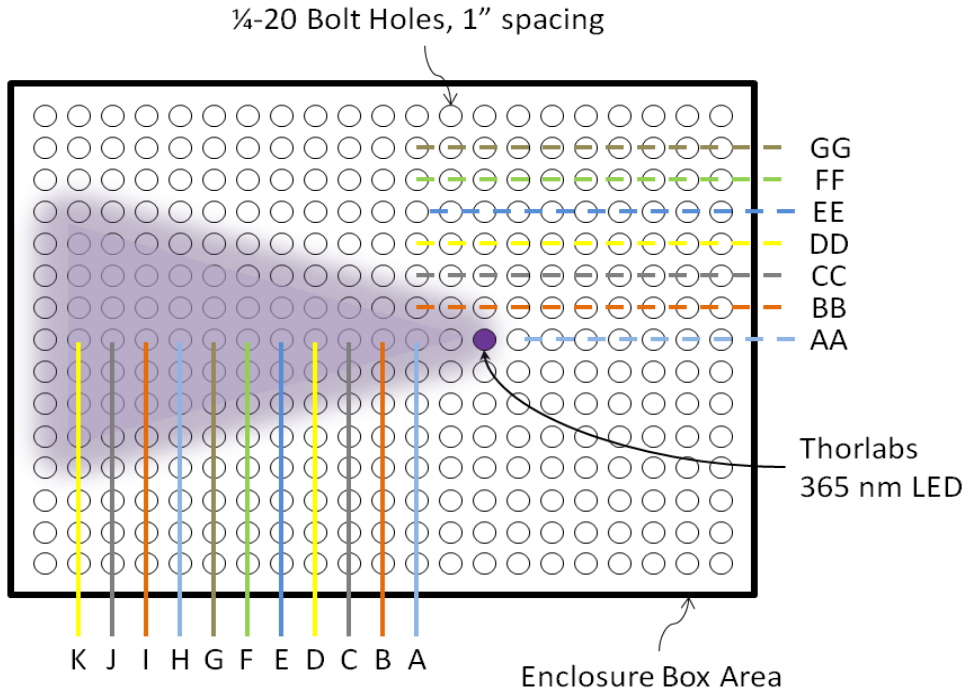


Figure 6-2. Depiction of positioning scheme representing stand-off distance.

Utilizing the instrumentation detailed previously in Section 4, a series of tests was performed to investigate the three topics of interest presented at the beginning of this section. First, the background light contamination was investigated. In full-scale OSTR experiments, it was hypothesized that large fluorescent lights might have a significant impact on photodiode response and resulting outcomes. The tests shown in Figure 6-3 use the Thorlabs M365FP1 LED light source for a PDA25K amplification gain setting of 0 dB. Logically, the maximum photodiode response occurs at position A-AA, according to Figure 6-2. However, as shown in Figure 6-3, the “lights on” condition is nearly identical to the covered condition, indicating that the influence of overhead, fluorescent lights has a minimal effect on the signal. In fact, the “lights on” condition increases the signal by an average of only 1.65 percent. The data from Figure 6-3 were taken at a reduced sample rate (500 Hz) to avoid overwhelming the NI LabVIEW software’s internal memory for the test duration of several seconds. The LED light source was programmed to output zero light for the initial and final 0.25 seconds, and maximum output for 1.25 seconds. During the zero incident light

condition, from Figure 6-3, the PDA25K exhibits a nonzero response due to inherent noise. For OSTR experiments, the noise level is removed through subtraction to null the PDA25K response during a zero light condition to maintain continuity with the theoretical models outlined in Section 3.2.

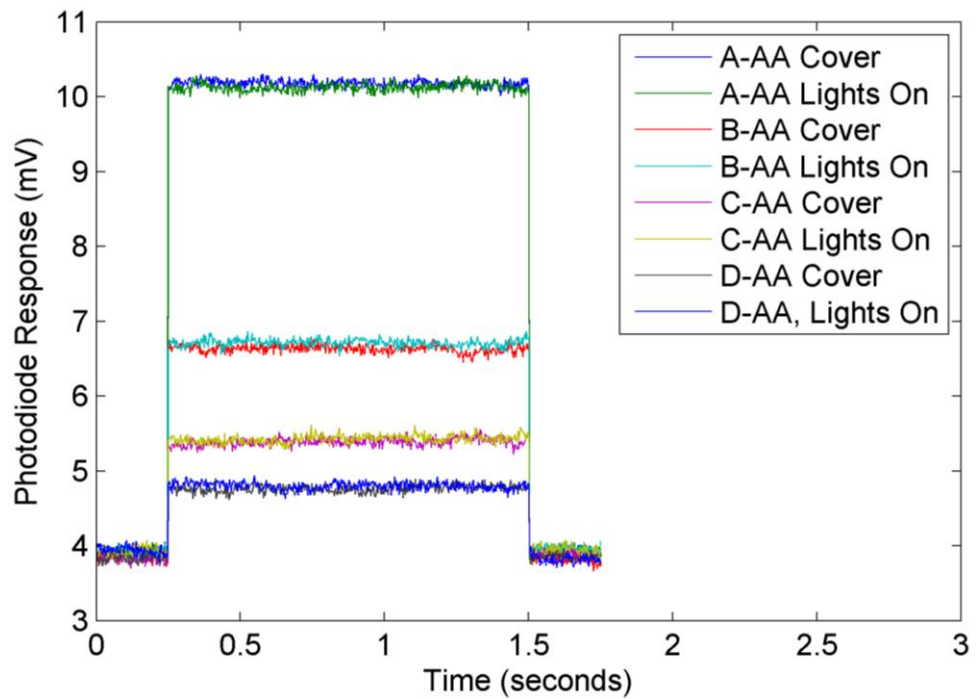


Figure 6-3. PDA25K response at 0 dB at steady light intensity for select positions.

Next, the impact of angular offset and stand-off distance on the photodiode response was investigated to provide a foundation for desktop experiments using a transient LED light intensity in a similar fashion to OSTR transients. Figure 6-4 provides the normalized voltage response of the Thorlabs PDA25K at a gain setting of 70 dB as a function of position from the LED light source illuminating the space at a constant output intensity calculated for each photodiode position per Figure 6-2. As expected, voltage intensity decreases with increasing distance from the LED. For all test positions, the photodiode was positioned normal to the “distance along” axis. As a result, the photodiode response decreases quickly with increased distance along, since the solid angle of the photodiode’s surface decreases.

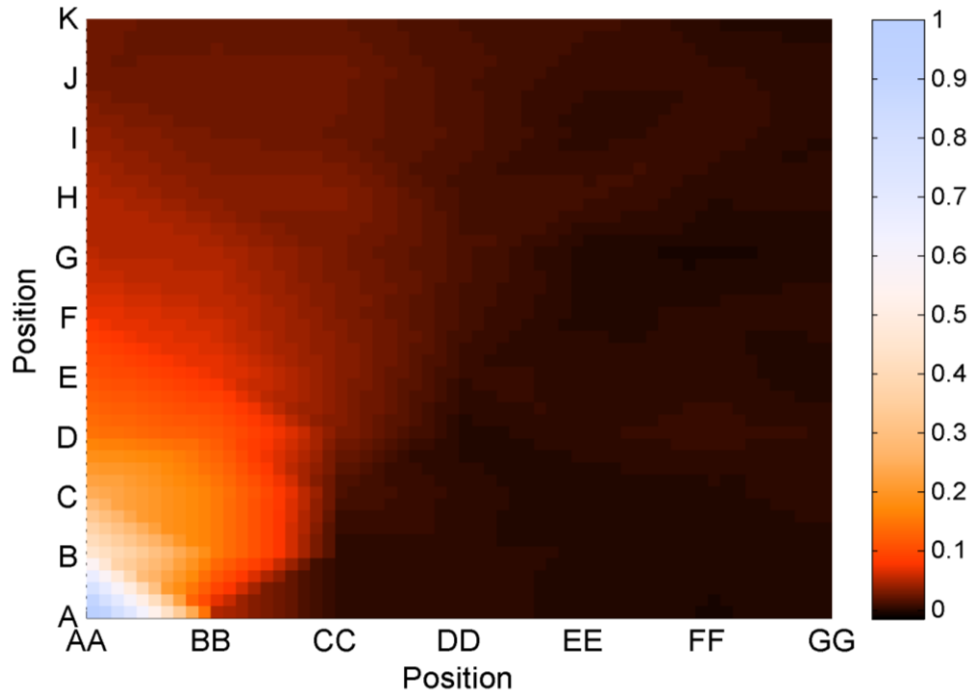


Figure 6-4. Contour plot for normalized photodiode response

To provide values of uncertainty for each photodiode response, Figure 6-5 provides a selection of individual row data, per the positions defined by Figure 6-2. The uncertainty in the photodiode response is calculated with the standard deviation at of the photodiode response during the constant output intensity portion of the Figure 6-3

data. As a result, the ranges of the uncertainty bars in Figure 6-5 are extremely small. Additional photodiode response curves as a function of position may be found in Appendix A.

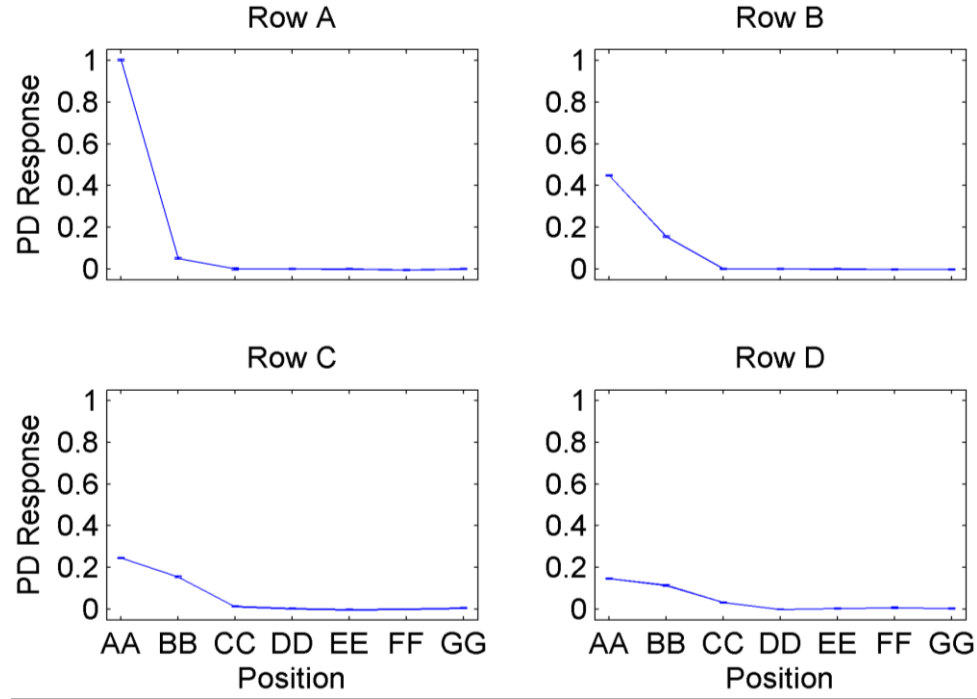


Figure 6-5. Normalized PD response with associated uncertainty (A-D)

6.1.3 Simulations

It is imperative to explore the viability of an experimental situation with computational simulations to confirm the physical phenomena observed by instrumentation, and confirmation allows the further simulation of experiments with confidence.

Figure 6-6 provides the theoretical photon flux at each detector position (at 1 inch intervals) from a constant light source with a given dispersion angle (33 degrees) to match the Thorlabs M365FP1 LED solid angle at the emission point of the light. The data for Figure 6-6 were acquired with Monte Carlo N-Particle (MCNP6.1.1 [95]) to

compare with measured values in Figure 6-4. The overall trend in Figure 6-6 is similar to that of Figure 6-4, but discrepancies arise through the orientation of the photodiode. As stated before, the photodiodes are positioned normal to the “distance along” axis, causing the normalized response of the photodiode in Figure 6-4 to decrease faster than the normalized photon flux in Figure 6-6. To illustrate this behavior, observe the detector position at (CC, K). In Figure 6-4, this value is approximately 0.075; however, in Figure 6-6, the same value provides a value of approximately 0.05.

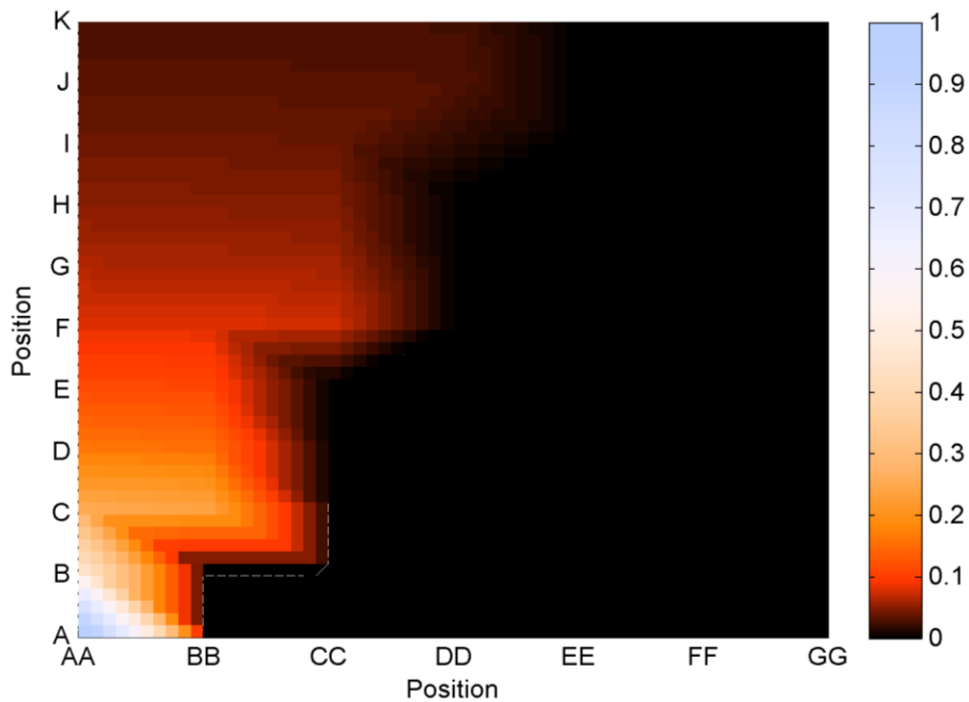


Figure 6-6. Contour plot for normalized MCNP photon transport

Based on these preliminary tests, it is pertinent to acquire as many data points as possible for uncertainty quantification, per Figure 6-5, and to position the photodiode normal to the incoming flux during OSTR experiments.

6.1.4 Transient Testing with Desktop Experiments – Square Waves

Recall from Section 3.2.4 that it is desired to use the PJ approximation, given below, to characterize the fissile material content within the reactor during a reactivity insertion of less than \$1.00, as defined by (3-9).

$$P(t) = \frac{\beta}{\beta - \rho} e^{\frac{\lambda\rho}{\beta - \rho}t} - \frac{\rho}{\beta - \rho} e^{\frac{\rho - \beta}{\lambda}t} \quad (3-39)$$

The desktop experiments described previously have consisted of the LED light source at a binary position (full on/off) to characterize the positional response of the photodiode. However, to determine fissile material content, a transient must be measured. During a separate desktop experiment, a time dependent signal from the NI LabVIEW VI to the Thorlabs M365FP1 LED light source was used to mimic the Cherenkov light intensity from a reactor core composed of U-235 for a \$0.50 and \$0.75 reactivity insertion, with the Thorlabs PDA25K response measured at a gain setting of 0 dB shown in Figure 6-7. The data were recorded by the NI PXIe-5171R digital oscilloscope at a sample rate of 250 MHz. The theoretical kinetics parameters used were obtained from the OSTR BOL values from Table 3-1.

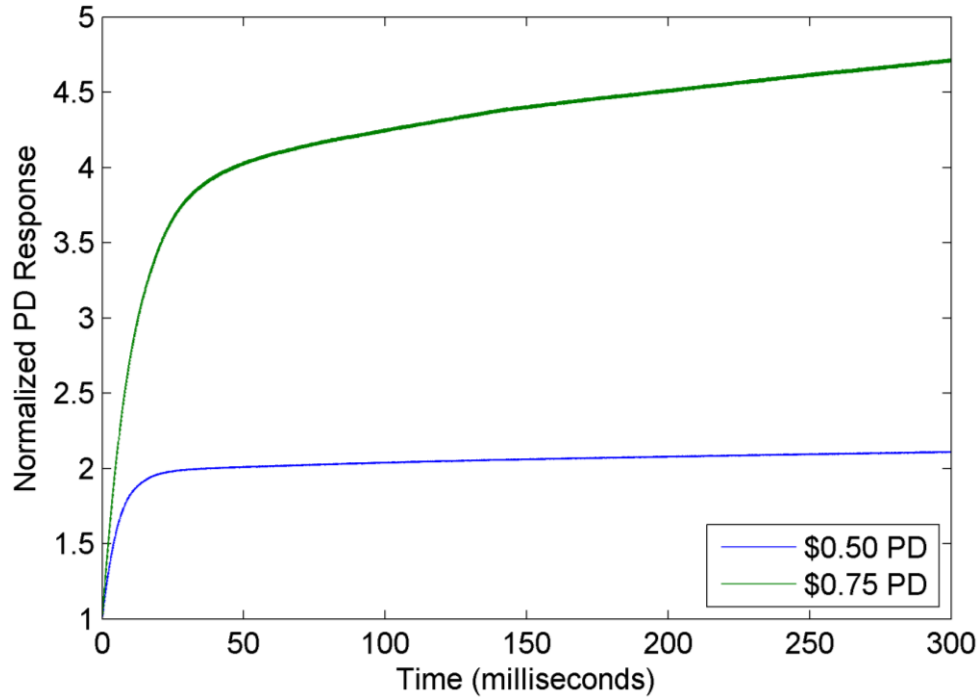


Figure 6-7. Response of PD to square waves with different \$ values.

As discussed in Section 3.2.4, the calculation of individual reactor kinetics parameters is possible with square waves through the comparison of the curve fits for each individual reactivity insertion. From (3-39), the first term contains the long term exponential inverse period (s_1) and the PJ value, while the second term contains the inverse transient period (s_2), shown in (6-1), (6-2), and (6-3), respectively.

$$s_1 = \frac{\lambda\rho}{\beta - \rho} = \frac{\lambda\$}{1-\$} \quad (6-1)$$

$$PJ = \frac{\beta}{\beta - \rho} = \frac{1}{1-\$} \quad (6-2)$$

$$s_2 = \frac{\rho - \beta}{\Lambda} = \frac{\beta(\$-1)}{l(1-\rho)} = \frac{\beta(\$-1)}{l(1-\$)\beta} \quad (6-3)$$

From (6-1), the curves in Figure 6-7 may be curve fit in MATLAB based on a generic form of the first term in (3-39), shown in (6-4), for the steady inverse period for the latter portion of the curve to calculate the \$ value for each respective PD response assuming a single delayed neutron group, where P_J is the PJ value from (6-2). The

Thorlabs M365FP1 LED light source was programmed to use a delayed neutron precursor half-life of 2.23 seconds (λ_4 in [6]) based on its applicable in the time regime approximately 1-2 seconds after a reactivity insertion for a square wave.

$$P(t) = P_1 e^{s_1 t} \quad (6-4)$$

Then, using the identified $\$$ value of simulated reactivity insertion, the entire PD response curve is fit to the form of (6-5), which provides the value of the inverse transient period, s_2 , provided in (6-3).

$$P(t) = P_1 e^{s_1 t} + P_2 e^{s_2 t} \quad (6-5)$$

Finally, after the fitted value for the inverse transient period (s_2) is found for the two separate reactivity insertions, the value of β may be calculated through the manipulation of (6-3) in the form of (6-6), where f represents the calculated s_2 value for each respective reactivity insertion, and the indices 1 and 2 in (6-6) represent the first and second reactivity insertion to be compared.

$$\beta = \frac{f_1(\$_2 - 1) - f_2(\$_1 - 1)}{f_1 \$_1 (\$_2 - 1) - f_2 \$_2 (\$_1 - 1)} \quad (6-6)$$

Table 6-1 presents the analysis of the simulated reactivity insertions performed in Figure 6-7.

Table 6-1. Reactor kinetics values for PJ approximations from Figure 6-7

	\$0.50 PJ with LED source	\$0.75 PJ with LED source
Theoretical Dollar Insertion	\$0.50	\$0.75
Calculated Dollar Insertion	\$0.5004	\$0.7526
Theoretical Inverse Transient Period (s_2)	-168.78	-84.55
Calculated Inverse Transient Period (s_2)	-170.44	-79.31
Theoretical β_{eff}	0.0076	
Calculated β_{eff}	-0.3506	

From Table 6-1, the curve fitting method calculates the dollar insertion in very good agreement with the theoretical dollar insertion output by the Thorlabs M365FP1 LED light source. Additionally, the calculated inverse transient period from (6-3) is in good agreement with the theoretical value. However, when the calculation of the delayed neutron fraction (β) is performed, significant disagreement is observed, which results from the magnitude of the desired value. Returning to the value of the inverse transient period (6-3), the delayed neutron fraction in the denominator is the variable solved for in (6-6) by assuming the β/l value is consistent between the two reactivity insertions. However, since the value of β is small ($\sim 10^{-3}$), slight differences in the calculated inverse transient period cause a very large difference in the calculated delayed neutron fraction. The impact of slight irregularities within the PD response during reactivity insertions in OSTR experiments are non-negligible and require additional filter or other manipulation to produce results with significance.

6.1.5 Transient Testing with Desktop Experiments – Reactor Pulses

For reactivity insertions more than \$1.00, recall the theoretical FN model from Section 3.2.3, presented again as reference:

$$\frac{P(t)}{P_{\max}} = \operatorname{sech}^2\left(\frac{\omega t}{2}\right), \quad (3-24)$$

where ω is the initial reactor period following the reactivity perturbation and defined by (3-25).

$$\omega = \frac{\rho_0 - \beta}{l} = \frac{\beta(\$-1)}{l} \quad (3-25)$$

The Thorlabs M365FP1 LED light source was programmed to output a light intensity characteristic of a reactor pulse based on the FN model for reactivity insertions of \$1.75 and \$2.00, with the Thorlabs PDA25K response shown in Figure 6-8 from the maximum response to the end of the simulated reactor pulse with a comparison of the FN model in (3-24). The theoretical kinetics parameters used were obtained from the

OSTR BOL values from Table 3-1. The data were recorded by the NI PXIe-5171R digital oscilloscope at a sample rate of 250 MHz. For each plot, the noise of the Thorlabs PDA25K, or the voltage signal that occurs during a state of zero incident light, is subtracted from the total signal, the photodiode signal is normalized to its maximum voltage value, and the response peak is assigned to occur at $t = 0$. From Section 3.2.3, it can be determined that a larger $\$$ insertion causes a larger peak reactor power, and therefore Cherenkov light intensity. However, by normalizing the PD response to its maximum for each respective curve, larger $\$$ insertion causes a “steeper” curve, shown in Figure 6-8.

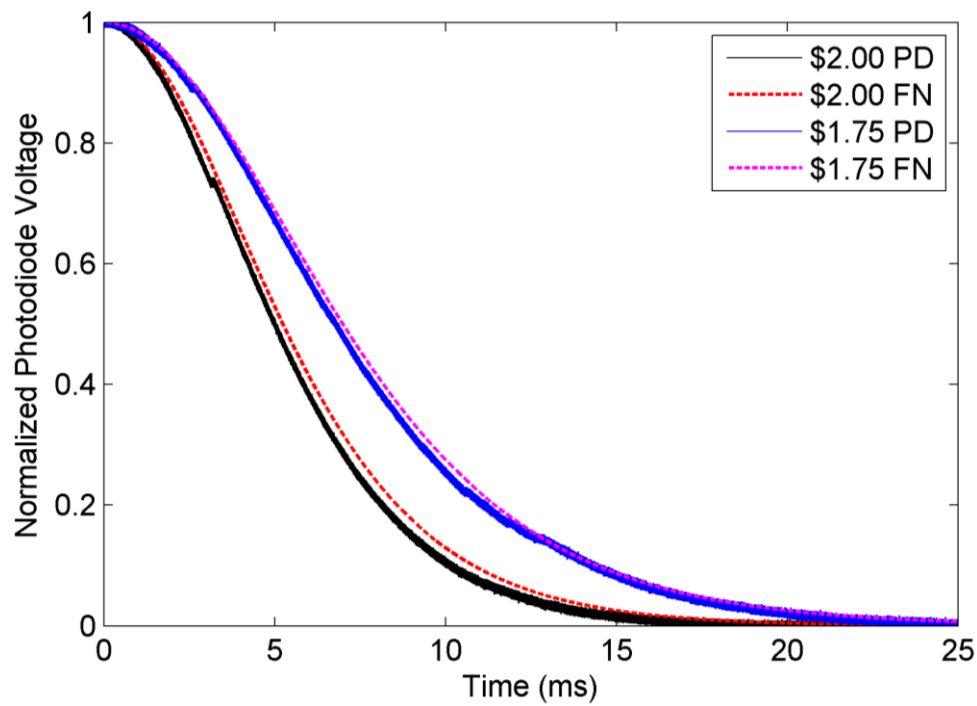


Figure 6-8. Response of PD to reactor pulses with different $\$$ values.

The PD responses in Figure 6-8 are in good agreement with the theoretical FN model used as the programmed output of the Thorlabs M365FP1 LED light source. However, slight discrepancies occur during the response shown in Figure 6-8. It is hypothesized that these deviations from the model occur due to the response of the LED light source with respect to a rapid increase or decrease in supplied current. This phenomenon was observed over multiple, repeated tests with simulated reactor pulses

and cannot be adequately corrected since the transient response of the LED is not well characterized by Thorlabs, Inc.

However, the discrepancy is beneficial for the analysis of the pulses in Figure 6-8 using methods detailed in Section 3.2.3 for a reactivity insertion with varying temperature feedback and a ramped reactivity insertion, since these are representative of irregularities in reactor output as compared to the FN model. Recall the modified FN model, shown again for reference in (3-32), and the solution methods based on the integral and second derivative in (3-35) and (3-36), respectively.

$$\frac{P(t)}{P_{\max}} = \operatorname{sech}^2\left(\frac{\omega t}{2}\left(1 + H(\$ - 1)^2\right)\right) \quad (3-32)$$

Since it is assumed that the LED light source possesses a time delay or other irregularities based on the magnitude of the intended supplied current, the analysis of both reactivity insertions in Figure 6-8 can be used to compute the β/l ratio. Results of the analysis with the FN model for each individual pulse are found in are found in Table 6-2 , and the analysis of the simulated pulses using the modified FN model are provided in Table 6-3. For the analysis utilizing the second derivative of the PD response, it is necessary to filter the data to avoid excessively large values of the second derivative due to the sample rate of the NI PXIe-5171R digital oscilloscope at 250 MHz and the time constant of the capacitor in the amplifier in the Thorlabs PDA25K. Figure 6-9 presents identical data to Figure 6-8, but with a smaller time scale on the abscissa. As can be observed in Figure 6-9, the pulse shape of the data for each PD curve is ill-suited to obtain accurate derivatives, since derivatives act as a “high-pass” filter, which allows for signals varying in an oscillatory manner to be preserved.

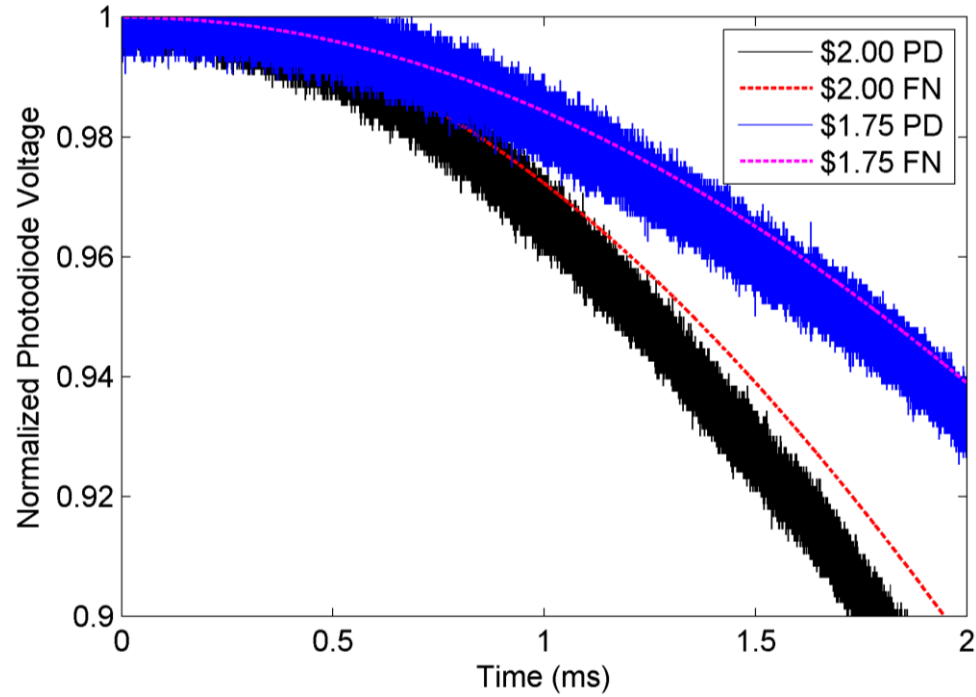


Figure 6-9. Detailed view of PD response from Figure 6-8

However, by using a Butterworth filter [126] to “smooth” the data, a pulse shape profile was created without the oscillations observed in Figure 6-9 due to Gaussian electronic noise and the time constant of the amplifier circuit in the Thorlabs PDA25K. A Butterworth filter is designed to have a flat frequency response in the passband of interest, is a standard MATLAB filter package, and requires the sample frequency to be specified; in this case, the value was 250 MHz, the sample rate of the NI PXIe-5171R digital oscilloscope. Additionally, a cutoff frequency is required. In order to capture the entire pulse shape, the cutoff frequency was specified as the inverse of the duration of the pulse to provide accurate results for the PD response data in Figure 6-8. Though this option does provide good analysis and agreement with both theoretical values and integration techniques, its application is limited in OSTR experiments since slight changes in the cutoff frequency significantly affect the calculated β/l ratio. A comparison of the values of the β/l ratio in Table 6-2 shows that analysis using the integration and second derivative technique do not accurately predict the β/l ratio from the theoretical FN model in (3-24) for either value of

simulated reactivity insertion. However, Table 6-3 provides more accurate values of the predicted β/l ratio by utilizing the novel, modified FN model in (3-32) to provide the β/l ratio based on the data obtained from both simulated reactivity insertions.

Table 6-2. Calculated β/l ratios for FN model and simulated reactor pulses

Reactivity Insertion	Selected data from Figure 3-5	β/l measurement using integration (3-27)	β/l measurement using 2 nd derivative (3-30)
\$1.75	FN (theory)	336.28	336.28
	PD	346.89	337.98
\$2.00	FN (theory)	336.28	336.28
	PD	358.10	341.86

Table 6-3. Calculated β/l ratios for modified FN model and simulated pulses

Selected data from Figure 3-5	β/l measurement using integration of two pulses (3-35)	β/l measurement using 2 nd derivative of two pulses (3-36)
FN (theory)	336.28	336.28
PD	332.47	332.99

Analysis of PD response data obtained during OSTR experiments is more suitably analyzed with integration, rather than second-derivative, techniques. The integration technique of the curves in Figure 6-8 may also be applied to PD response curves with a Butterworth filter for improvement in integration by removing electronic noise and oscillations from the amplifier circuit. Any value of the cutoff frequency less than the sample rate and greater than the inverse of the pulse duration may be applied; however, minimal improvement is found over integration with raw data due to the relatively small magnitude of the oscillations and Gaussian noise as compared to the signal data.

6.1.6 Desktop Experiment Conclusions

The desktop experiments show the ability of the Thorlabs PDA25K to capture a simulated reactor pulse with intended reactivity insertions mimicking the FN model. However, due to discrepancies associated with the Thorlabs M365FP1 LED light

source's transient behavior, the light intensity does not exactly simulate the FN model and creates large errors when attempting to calculate β/l with the FN model, though these errors are minimized when analyzing the pulses with the modified FN model.

Additionally, it is concluded that the calculation of the β/l ratio should be performed only with an integration approach for OSTR experiments, since the second derivative method requires a filter to discern the pulse shape when sampled with the NI PXIe-5171R digital oscilloscope. The value of the cutoff frequency in the applied filter has an impact on the computation of β/l , and an ideal value is not easily attainable. In a safeguards application, the value of the cutoff frequency could negatively impact the CRANK system's methods and could cause false discrepancies in the measured and reported reactor kinetics parameters, an undesirable characteristic for technologies dedicated to nuclear safeguards in a facility.

6.2 OSTR Experiments

OSTR experiments with the CRANK system began in February 2016 with the objective of ascertaining the reactor kinetics parameters in the OSTR with associated uncertainty and comparing these results with the declared reactor kinetics parameters in the OSTR FSAR [106] obtained by using MCNP5 [68].

Experiments were performed to validate 1) the methodology of solving the reactor kinetics parameters using the novel, modified FN model, and 2) the use of Cherenkov light as an accurate representation of reactor power above a lower threshold. Additionally, the results provide insight to the CRANK system's ability to discern reactor kinetics parameters in a safeguards application during inspections over a defined interval for a facility.

Based on the observations previously in Section 6.1.5, the simplest, unambiguous method of calculating the β/l ratio is the integration of the raw, normalized PD response data during a reactor transient, with specific data manipulation detailed in

Section 6.2.2 Slight changes in filtering methods in performing derivatives result in variations of the calculated β/l ratio, and without prior knowledge of reactor characteristics, it is inadvisable to perform such filtering during the intended purpose of the CRANK system, which is the inspection of a research reactor facility governed by a safeguards program. Additionally, conclusions from safeguards measurements must be associated with a provided value of uncertainty, and the propagation of errors through filtering methods are cumbersome and may increase the overall uncertainty of the calculated reactor kinetics parameters.

6.2.1 *Square Waves*

The initial OSTR experiments focused on square waves since, from Section 3.2.4, it is possible to independently determine the reactor kinetics parameters using a curve fitting analysis based on the PJ approximation (3-39). However, despite improvements from a longer fiber bundle, detailed in Section 4.3, and an optical lens with greater transmission at Cherenkov wavelengths, detailed in Section 4.4, the Cherenkov light intensity was not sufficient to create a PD response with a large enough S/N ratio to provide the reactor kinetics parameters with acceptable values of uncertainty. In fact, the abrupt power jump characteristic of the reactor's transient period following a square wave is not readily seen by the human eye, either.

The OSTR possess license limits that prevent an operator from inciting a reactor transient above 1 kW of steady-state thermal power, though, as a guideline, reactivity insertions are performed at an initial power of 15 W. Initial OSTR experiments were performed from a power level of 15 W, but latter tests were performed from the upper threshold of 1 kW in an attempt to increase the intensity of Cherenkov light during the transient. Figure 6-10 provides the PD response with the highest S/N ratio during all square waves performed. The data in Figure 6-10 were collected during a \$0.80 square wave on 25 May 2016 (SQ-10). OSTR experiments are labeled chronologically, and a complete list of square waves at OSTR measured with the CRANK system can be found in Table B-1. Figure 6-10 provides the raw PD

response in addition to a filtered signal utilizing a Butterworth filter with cutoff frequency of 50 Hz for better visualization of the transient profile.

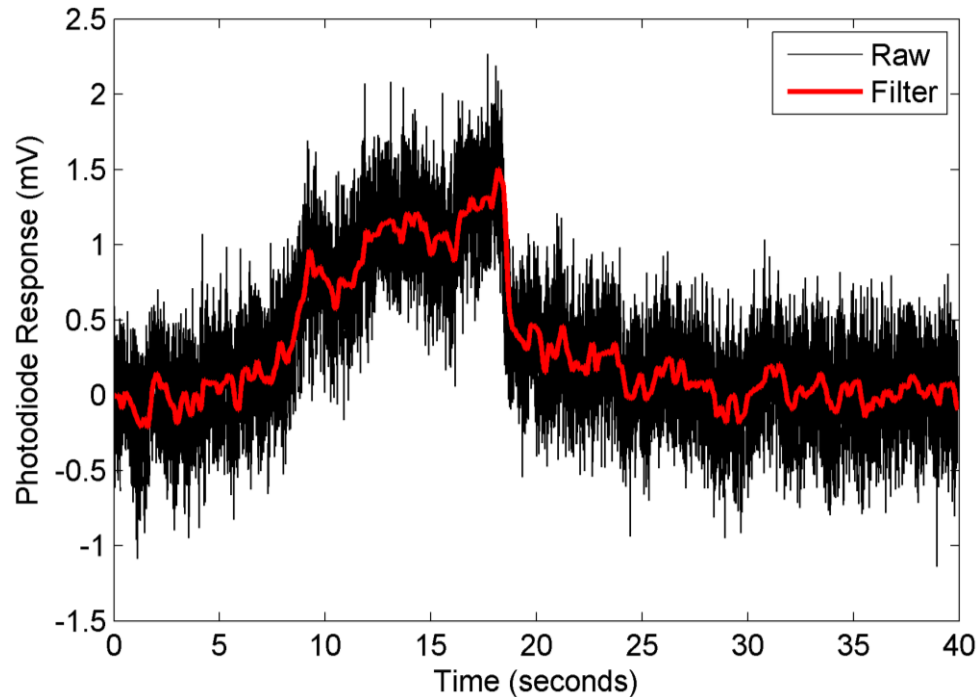


Figure 6-10. PD response from \$0.80 square wave (SQ-10)

As can be noted from Figure 6-10, there is a distinct increase in PD response from approximately 8 seconds to 18 seconds. Though the increase might indicate potential success for analyzing the reactivity transient with the PJ approximation, the increase in PD response is due to the inverse steady reactor period (s_1) in (6-1), rather than the abrupt power jump from the inverse transient reactor period (s_2) in (6-3). Recall from Figure 6-7 that the abrupt increase in power (PJ from (6-2)) due to the transient reactor period occurs over approximately 20-100 milliseconds, while the time scale on the abscissa of Figure 6-10 is on the order of seconds. Also, a sharp decrease can be observed at approximately 18 seconds in Figure 6-10 caused by a reactor SCRAM (or shut down) in which all control rods are reinserted into the OSTR core when reactor power reaches a level of 1 MW.

The only method outlined in Section 3.2 that allows for the independent calculation of reactor kinetics parameters with the CRANK system was the analysis based on curve fitting the PJ approximation. However, Figure 6-10 shows that this approach is ill-advised, even with the best S/N ratio measured (SQ-10). In fact, experiments on 20 September 2016 measured the increase in Cherenkov light intensity as reactor staff increased the reactor power slowly. Results from this experiment showed that the intensity of Cherenkov light was not measurable by the CRANK system in its current configuration until a reactor power of approximately 500 kW. In comparison, the resulting PJ from a \$0.80 is a factor of 5. Therefore, when initiating a \$0.80 reactivity insertion from 1 kW, the reactor power reaches 5 kW in approximately 100 milliseconds, well below the measured threshold of 500 kW. The increase in PD response in Figure 6-10 is representative of the steady rise in reactor power following the initial, abrupt power jump. Since it is necessary to measure the Cherenkov light intensity during the abrupt power rise in the first ~100 milliseconds following the initiation of the reactivity insertion, attempts to measure Cherenkov light intensity with the CRANK system in square wave operations at OSTR were discontinued. Additional data collected during square waves are found in Appendix B.

6.2.2 Reactor Pulses

The increase in reactor power during a reactor pulse is many orders of magnitude greater than the increase during a square wave, allowing for a much greater S/N ratio for the PD response. However, recall from Section 3.2.3 that reactor pulses cannot be used to independently determine the reactor kinetics parameters, and no previously investigated methods related to the literature in Section 2.2 are capable of experimentally determining them independently either; only the β/l ratio may be determined.

The campaign of OSTR pulses was pursued simultaneously with square waves. A full list of OSTR pulses may be found in Appendix B, but those pulses with sufficient S/N ratio and sample rate for usable analysis are found in Table 6-4 with chronological

test number, test date, reactivity insertion, and gain setting of Thorlabs PDA25K in dB. It was found that large \$ pulses often saturated the NI PXIe-5171R digital oscilloscope with a gain setting at the maximum of 70 dB, so in some cases, this is decreased to 60 dB without consequence in the overall determination of the β/l ratio.

Table 6-4. Record of reactor pulses with sufficient data for analysis

Test Number	Date	Reactivity	Amplification (dB)
P-18	Dec. 12, 2016	\$2.00	60
P-19	Dec. 14, 2016	\$1.95	70
P-20	Dec. 14, 2016	\$2.00	70
P-22	Jan. 30, 2017	\$1.95	60
P-23	Jan. 30, 2017	\$2.00	60
P-24	Jan. 30, 2017	\$1.85	60
P-25	Jan. 30, 2017	\$1.89	60
P-26	Feb. 22, 2017	\$1.65	70
P-27	Feb. 22, 2017	\$2.00	60
P-28	Feb. 22, 2017	\$1.85	60
P-29	March 20, 2017	\$1.65	70
P-30	March 20, 2017	\$2.00	60
P-31	March 20, 2017	\$1.85	70

From Section 3.2.3, it is stated that the relative uncertainty associated with the determination of the β/l ratio using (3-35) or (3-36) is dependent on the reactivity insertions being compared. The full uncertainty analysis is found in Appendix C, and Figure 6-11 depicts this visually. It can be shown that a combination of a large reactor pulse (~\$2.00) and a medium sized pulse (~\$1.65) provide the lowest percent uncertainty in the determined ratio of reactor kinetics parameters while maintaining a large S/N ratio in the smaller pulse. However, it was determined that several repeated \$ values of reactivity insertion should be performed in addition to a variety of other reactivity insertions to address the validity of the method.

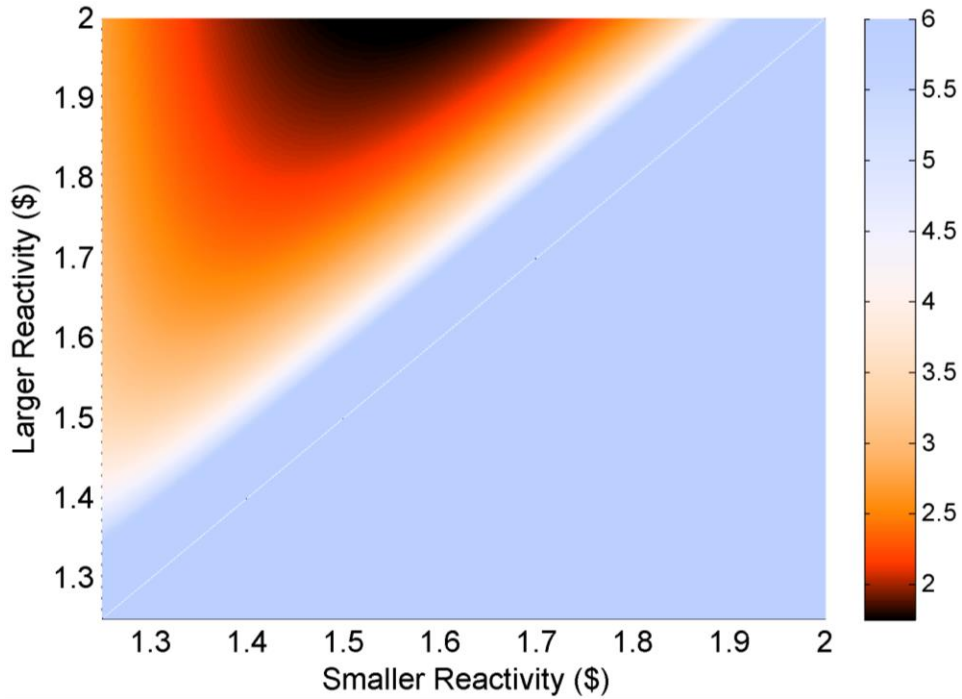


Figure 6-11. Percent experimental uncertainty in β/l ratio using (3-35) (2σ)

During the campaign of OSTR reactor pulses, it was found that there was a distinct difference in pulse shape between identical reactivity insertions performed on Monday compared to those performed later in the operating week. For the purposes of this research, the CRANK system measured OSTR pulse operations during conditions of both high core excess and low core excess. The difference is caused by the buildup of fission products, most notably Xe-135, which has a half-life of approximately 9.2 hours [6], and contributes to a decrease in control rod worth. The OSTR, described in detail in Section 4.1, contains four control rods – safety, shim, regulating, and transient, the last of which is pneumatically ejected for square wave and pulse operations. The OSTR is inactive on weekends, and the control rods are calibrated once per year on a Monday morning (high core excess condition) to ensure that fission products, especially Xe-135, have decayed sufficiently to minimize impact on control rod worth. The OSTR typically operates approximately 35 hours per week at a steady-state power of 1 MW, so the effect of fission product buildup may be visually

observed in the value of the core excess over the course of the week, shown in Figure 6-12 for four weeks of operating days in OSTR (6 February - 3 March 2017).

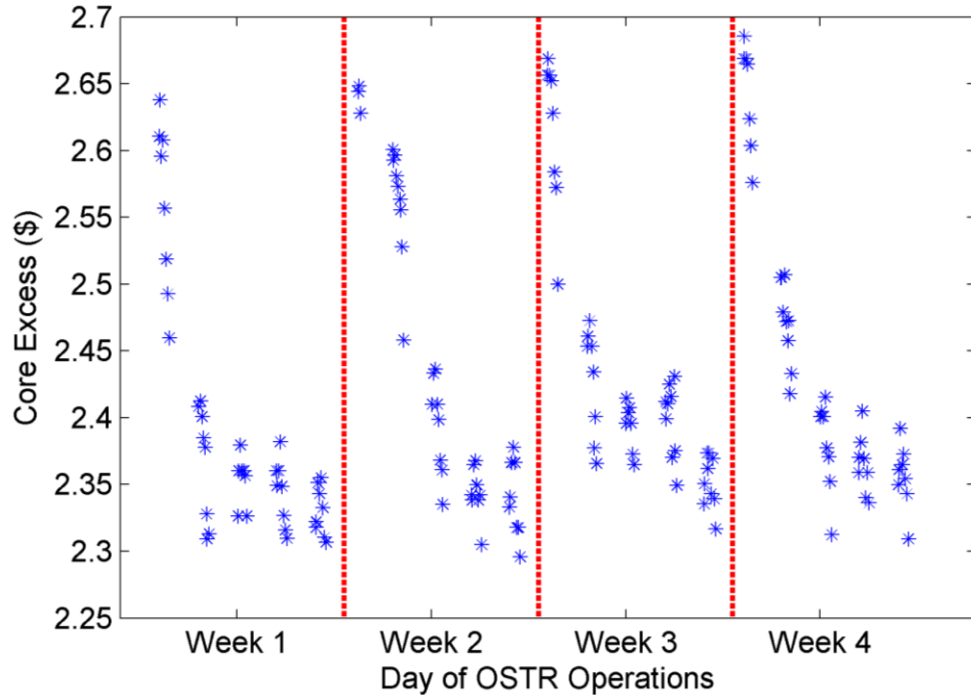


Figure 6-12. OSTR core excess over one month period

From Figure 6-12, four distinct sets of curves with five clusters of data points are visible that represent the four weeks and five days per week of data collection. The cluster of data points above \$2.60 of core excess occur on a Monday and decreasing during OSTR daily operations with a change in nearly \$0.30 over the course of a week. A detailed view of the first week from Figure 6-12 is found in Figure 6-13.

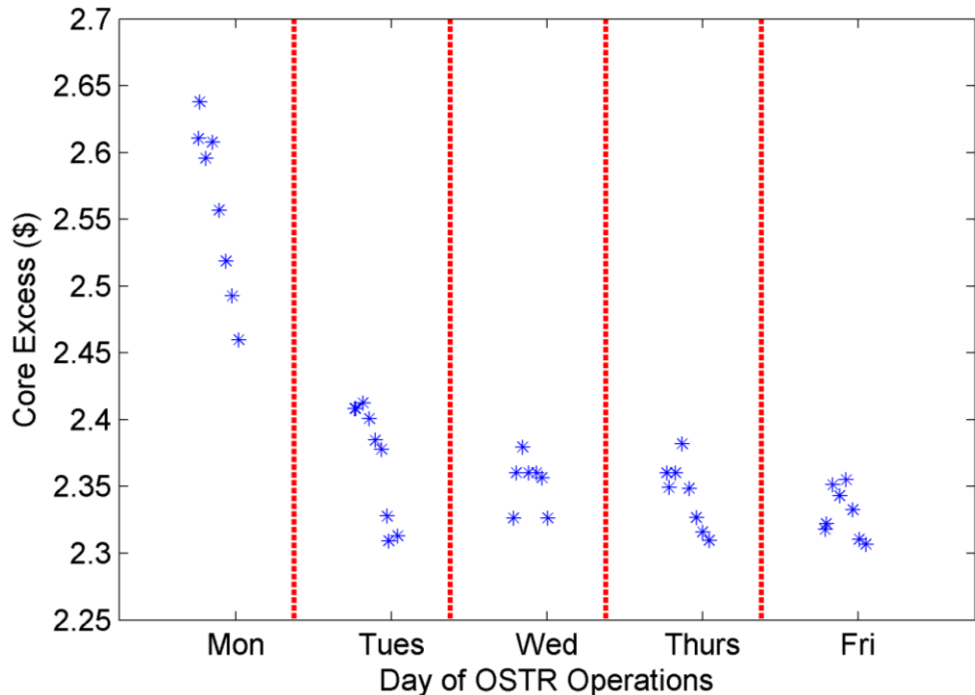


Figure 6-13. OSTR core excess over a one week period

The core excess, and therefore control rod worth, has a substantial effect on the pulse shape and Cherenkov light intensity. Recall from Section 5.2 that in the procedure for performing OSTR experiments in a methodology for safeguards inspections, two reactivity insertions are required to be specified. If an inspection occurs when the reactor is in a state inconsistent with the condition used for control rod calibration, the CRANK system and subsequent analysis will not accurately measure the ratio of the reactor kinetics parameters. Additionally, it is inherently difficult to determine a priori the reduced transient control rod worth in a low core excess operating condition as compared to a high core excess condition and becomes more complicated during a safeguards inspection. For the validation of the CRANK system and the novel, modified FN model analysis, the pulses from Table 6-4 are repeated in Table 6-5 and divided into its \$ value of reactivity insertion and OSTR core condition based on the day of the week it was performed. The data in Table 6-5 are divided into four categories, denoted by X_1 , X_2 , Y_1 , and Y_2 . The final result and associated uncertainty using the CRANK methodology to calculate the β/l ratio is highly dependent on the

requested reactivity insertions, shown in Figure 6-11. The large reactivity insertions are grouped into $X1$ and $X2$, while the small reactivity insertion OSTR experiments comprise $Y1$ and $Y2$. Likewise, OSTR experiments in a high core excess condition are grouped into $X1$ and $Y1$, with low core excess conditions divided into $X2$ and $Y2$. If the vectors X and Y are defined as (6-7) and (6-8), the matrix of calculated β/l ratios may be computed by (6-9) for each comparison of X and Y pulses, where N represents 1 or 2.

$$\bar{X} = (X1, X2) \quad (6-7)$$

$$\bar{Y} = (Y1, Y2) \quad (6-8)$$

$$\bar{X} \cdot (\bar{Y})^T = \left(\frac{\beta}{l} \right)_{XN,YN} \quad (6-9)$$

Table 6-5. Record of reactor pulses based on reactivity insertion and core excess

High Core Excess, Large Reactivity Insertion [X1]	Low Core Excess, Large Reactivity Insertion [X2]	High Core Excess, Small Reactivity Insertion [Y1]	Low Core Excess, Small Reactivity Insertion [Y2]
P-18	P-19	P-24	P-26
P-22	P-20	P-25	P-28
P-23	P-27	P-29	
P-30		P-31	

For the data collected with the CRANK system for all the pulses specified in Table 6-4 and Table 6-5, a specific methodology is followed to maintain consistency throughout the analysis to obtain the β/l ratio. The NI-5171R digital oscilloscope and NI LabVIEW software provided the ability to specify a PD response threshold in volts. When the threshold was exceeded by the increase in Cherenkov light intensity and subsequent PD response, the NI-5171R digital oscilloscope collected data at its maximum sample rate, 250 MHz for 100 milliseconds, far exceeding the duration of all OSTR pulses specified in Table 6-4.

A simple MATLAB script was written to perform the following functions for each reactor pulse:

- 1) A baseline PD response is measured during a zero light condition following assembly of the CRANK system at the OSTR prior to pulsing operations. These data are averaged and subtracted from the PD response during the reactor pulse.
- 2) The data are normalized to the peak value to provide consistency with the FN model and analysis techniques in Section 3.2.3.
- 3) Due to the large sample rate of the NI PXIe-5171R digital oscilloscope, minor oscillations are observed from the amplifier circuit in the Thorlabs PDA25K. A 2nd-order polynomial fit is created, centered on the PD response peak for a duration of one millisecond, and the PD response is normalized to the peak identified by the 2nd-order polynomial.
- 4) If desired, the adjusted PD response peak is assigned to occur at $t = 0$ to provide visual comparison with the FN model.
- 5) The PD response peak is integrated using the trapezoidal method from the adjusted peak value to the end of collected data.
- 6) When two pulses are analyzed in this manner, the β/l ratio and associated uncertainty is calculated. The uncertainty analysis includes all instrumentation error and mathematical sensitivity when calculating β/l per (3-35).

With respect to 3) above, a 2nd-order polynomial is created based on its ease of use and accuracy to theoretical and experimental data near the normalized peak power or normalized peak PD response, respectively. Figure 6-14 depicts the Taylor polynomial expansion of the FN model about $t = 0$, also known as a Maclaurin series, for even powers up to $n = 8$. Note that odd derivatives of the FN model are equal to zero when centered on the peak in a Maclaurin series. As can be observed, there is nearly no distinction between any curves for approximately one millisecond about the normalized peak power. Additionally, Figure 6-15 provides experimental data from P-29 with 2nd- and 4th-order polynomial fits to the experimental with nearly no

distinction between the two polynomial fits, which both exhibit excellent agreement with the experimental data. Also, the small oscillations observed from the Thorlabs PDA25K amplifier are evident in the experimental data, causing an inaccurate maximum to be calculated from raw data, rather than the pulse shape.

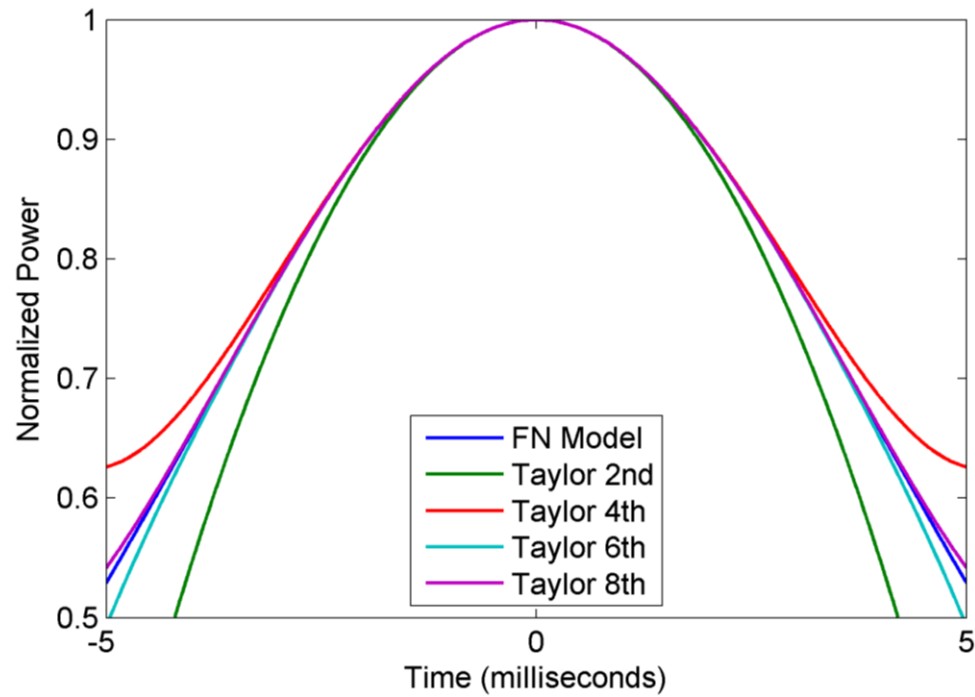


Figure 6-14. Taylor expansion of FN model

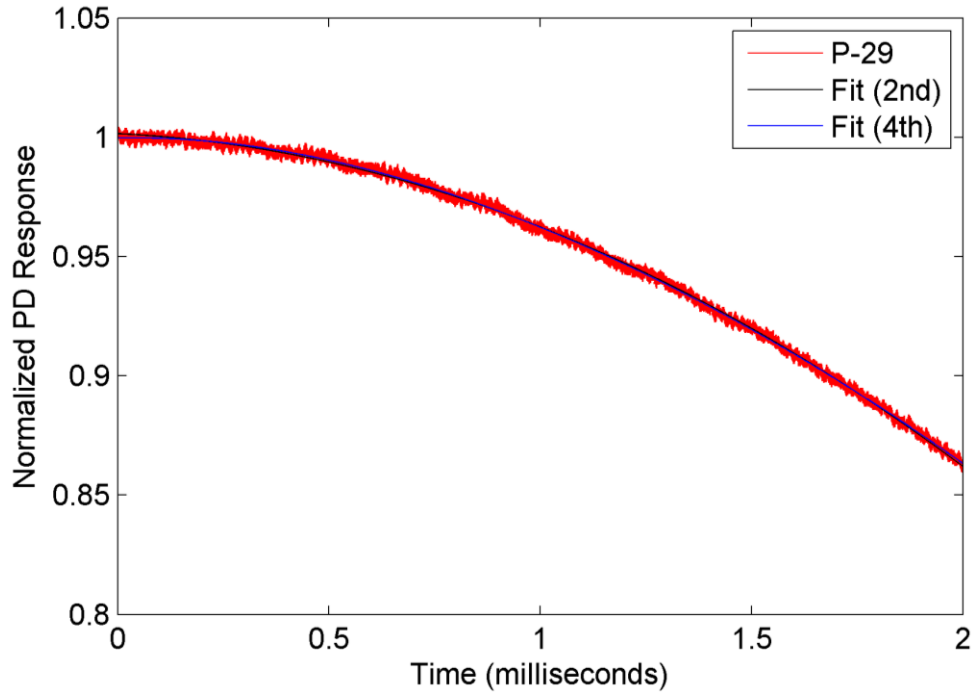


Figure 6-15. Second and fourth order polynomial fits of P-29 near pulse peak

Recall that the derivation of the FN model does not account for varying temperature feedback, which requires the manipulation of the existing model into the novel, modified form required for accurate determination of the ratio of the reactor kinetics parameters. Figure 6-16 provides pulse data collected on 30 January 2017 for P-22 and P-23, which correspond to \$1.95 and \$2.00 reactivity insertions, respectively. As expected, the lack of varying temperature feedback parameters causes the FN model curves using OSTR BOL kinetics parameters, found in Table 3-1, to be wider, representing a less steep pulse than is measured by the CRANK system. Additionally, recall that the integral method for the determination of the β/l ratio proposed in (3-35) is performed from the peak PD response to the end of the reactor pulse. Near the initiation of the pulse, the ramped reactivity insertion that occurs in a transient reactor causes a major deviation from the FN model to occur; since the CRANK system requires the user to specify a threshold PD voltage to begin measurements, varying the threshold voltage alters the profile of the pulse near the initiation of the transient.

Therefore, the initial behavior of the pulse is ignored to maintain consistency throughout varying PD gain settings and magnitude of reactivity insertion.

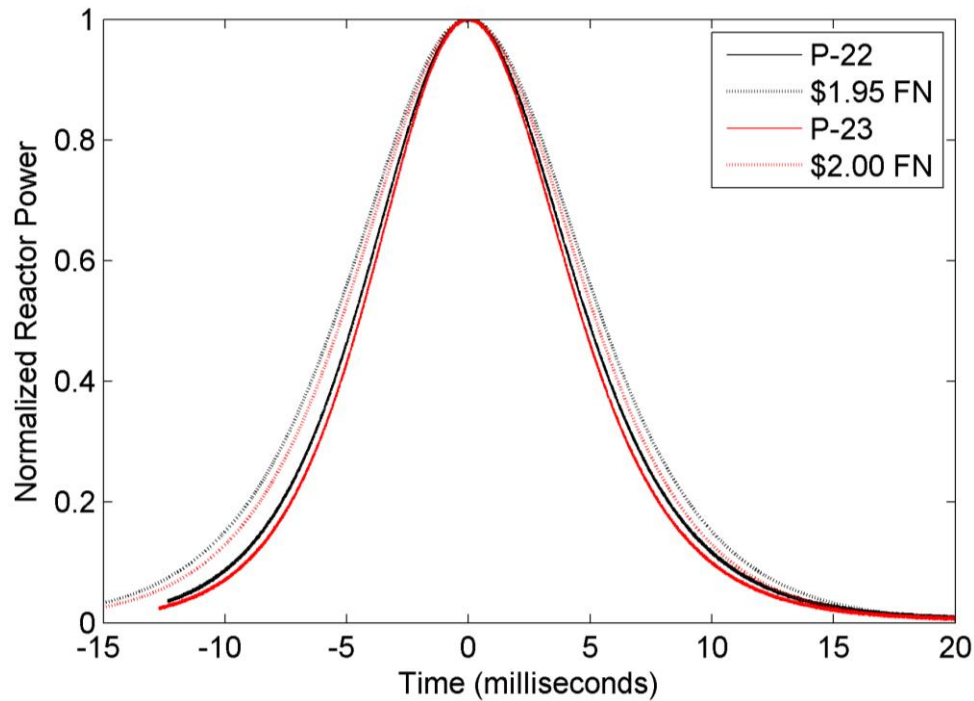


Figure 6-16. Comparison of P-22, P-23, and corresponding FN model

Figure 6-17 through Figure 6-20 present the CRANK system measurements for all pulses in Table 6-4. The larger reactivity insertions represent steeper pulse profiles, and the determination of reactor kinetics parameters may be performed with any combination of the measurements, given that the nominal values of the reactivity insertions are different.

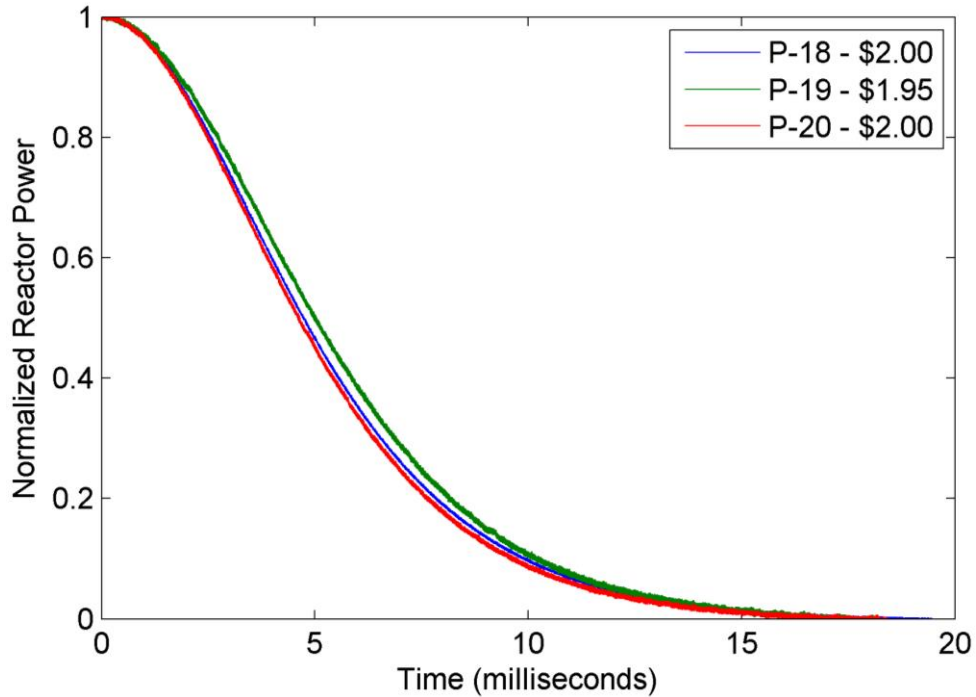


Figure 6-17. Comparison of P-18, P-19, and P-20 measurements

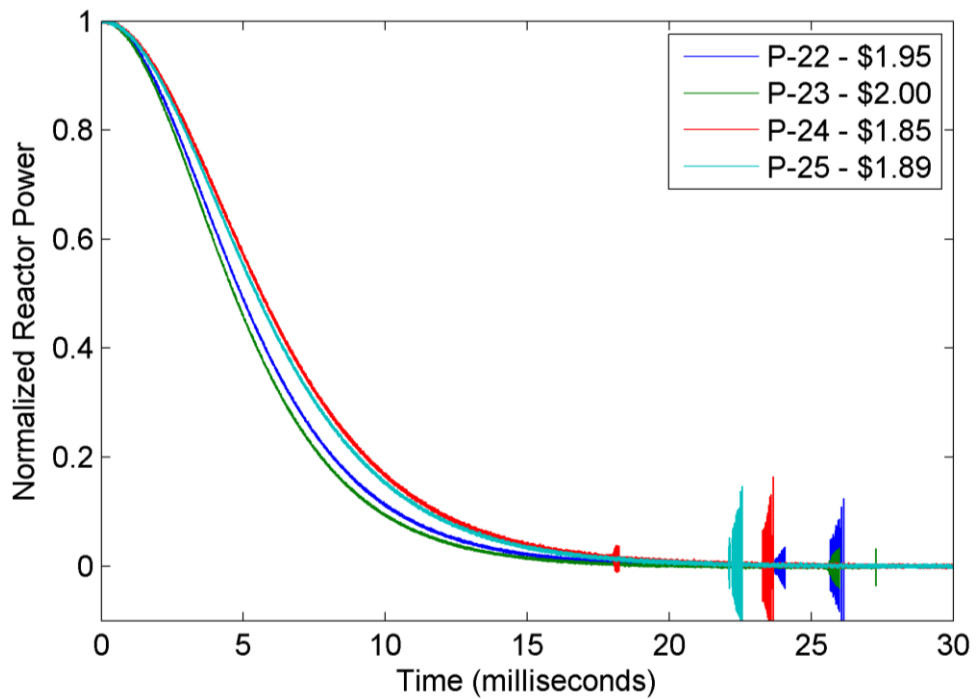


Figure 6-18. Comparison of P-22, P-23, P-24, and P-25 measurements

With respect to Figure 6-18, two phenomena are of importance. In each reactivity insertion at approximately 25 milliseconds following the pulse, a large oscillation occurs that does not reflect changes in the reactor power or Cherenkov light intensity. Instead, the oscillation is hypothesized to be caused by the SCRAM, or reactor shut down, signal based on the OSTR safety limits. Recall from Figure 4-15 that the PD is not submerged in the reactor pool, but is secured to the control rod housing to prevent instrumentation from inadvertently falling into the reactor pool. During the automated SCRAM signal initiated by the OSTR safety limits, the electric current generated in the control rod instrumentation interferes with the PD response voltage and alters its output. However, this oscillation caused by interference is symmetric about the axis of the pulse shape profile, so each oscillation contributes nil to the integral of each pulse profile, and the transfer of the PD to a different location was not required.

The second important phenomenon is the reduced transient rod worth for repeated, large \$ reactivity insertions. Figure 6-18 displays the pulse shape profiles for four separate reactivity insertions, with approximately 10-15 minutes elapsed between the initiations of each subsequent reactor transient. However, the pulse shapes of P-24 and P-25 did not reflect the anticipated pulse shape based on the profiles of P-22 and P-23, and instead exhibited a bias of approximately \$0.015 and \$0.02, respectively. Since P-22 and P-23 were reactivity insertions larger than those of P-24 and P-25, it is hypothesized the reduced reactivity observed could be caused by reactivity effects from decay of fission products generated or slight temperature increases from previous large \$ reactivity insertions. As a result, the time between pulses was extended to approximately 20-25 minutes in pulses after P-28 to mitigate this effect.

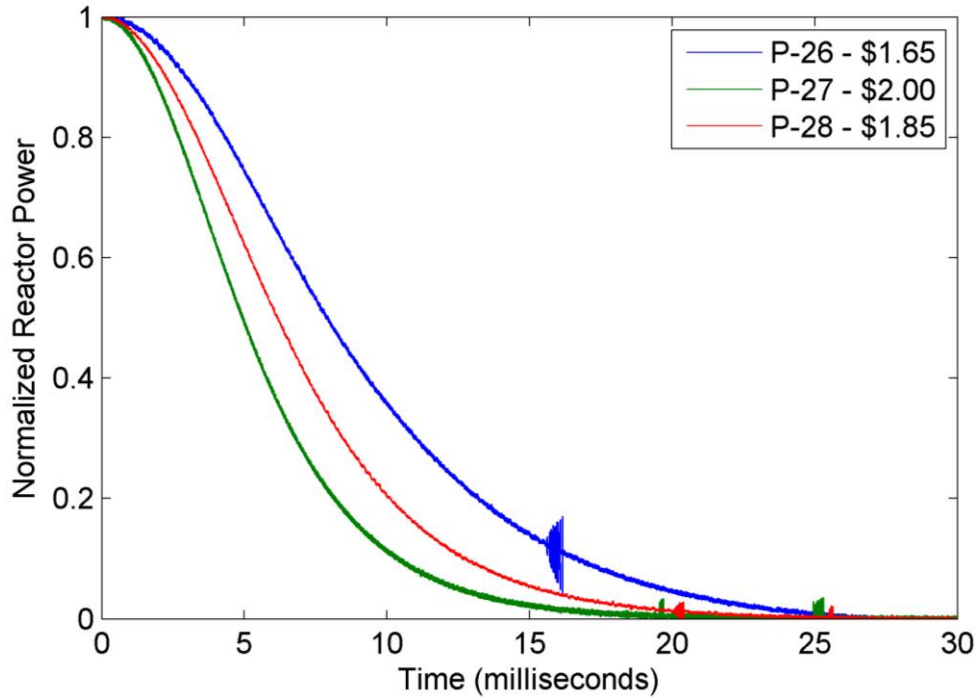


Figure 6-19. Comparison of P-26, P-27, and P-28 measurements

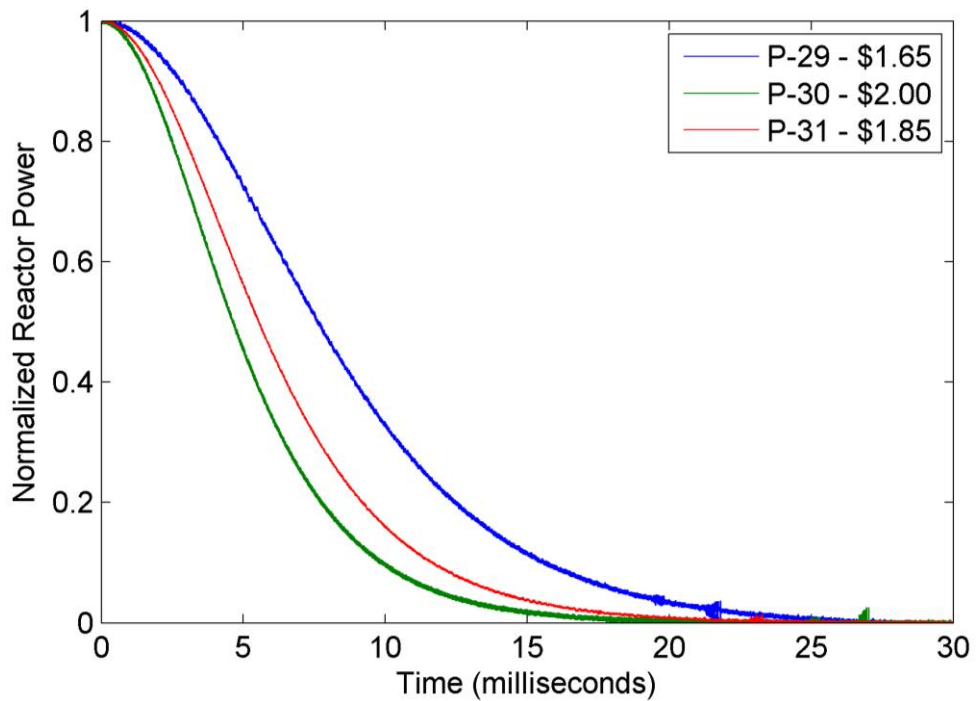


Figure 6-20. Comparison of P-29, P-30, and P-31 measurements

Earlier in Section 6.2.2, it was shown that differences occur in total control rod worth over the course of a week in the OSTR when it operates at maximum steady-state power of 1 MW for a day or more. Figure 6-21 depicts four pulses, P-26, P-27, P-29, and P-30, measured with the CRANK system, with two in a low core excess condition (Wednesday) for P-26 and P-27 and two in a high core excess condition (Monday) for P-29 and P-30. P-26 and P-29 were obtained during reactivity insertions of \$1.65, while P-27 and P-30 were obtained during reactivity insertions of \$2.00. Figure 6-21 also includes the FN model with OSTR BOL kinetics parameters, provided in Table 3-1, for comparison. For both sets of reactivity insertions, the pulse profile shapes in a high core excess condition are steeper and possess a smaller pulse width than the comparable pulse shapes with a low core excess, indicating that the transient control rod worth is greater in a high core excess condition as compared to a low core excess condition, which confirms the observations from the core excess plots in expected based on Figure 6-12 and Figure 6-13. In fact, P-26 and P-27 (low core excess conditions) represent pulse shape profiles that are offset from their respective high core excess condition pulses (P-29 and P-30) by the same reactivity value, approximately \$0.025, which indicates a discrepancy in the actualized reactivity insertion rather than inconsistency in the measurement method or intended reactivity insertion by the OSTR operators.

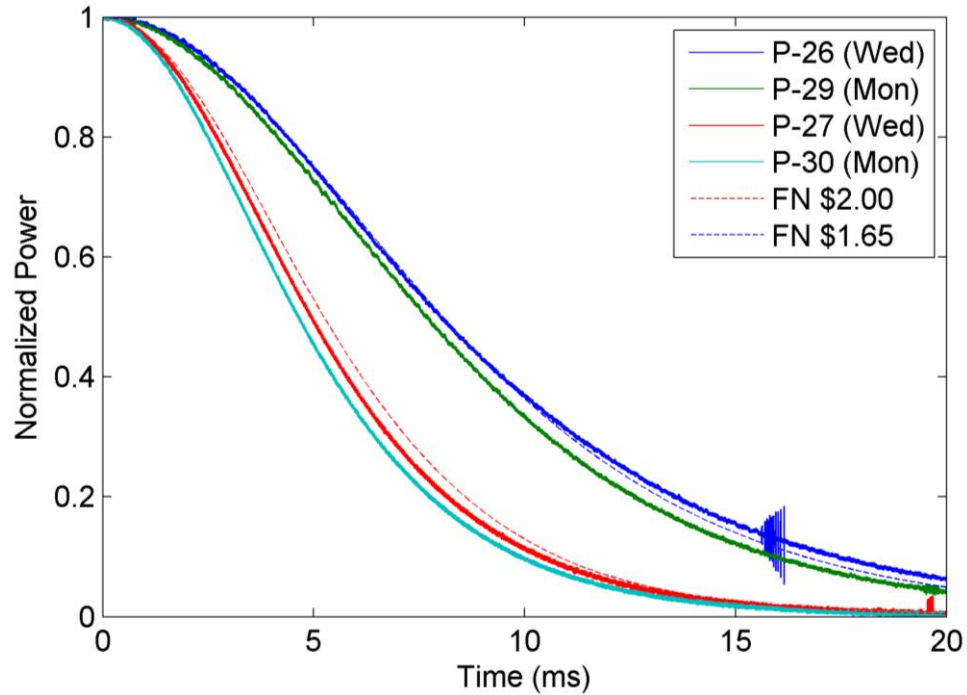


Figure 6-21. Comparison of Monday and Wednesday pulse measurements

The OSTR possesses three instruments to monitor reactor power during operations, and, during pulse operations, the ion chamber (IC) is used to measure the reactor power. Therefore, to provide a comparison against existing OSTR instrumentation, all \$2.00 pulse data from Table 6-4 is displayed in Figure 6-22 along with OSTR IC data from 26 May 2016. Additionally, the FN model is plotted for a \$2.00 reactivity insertion with OSTR BOL kinetics parameters from Table 3-1 and with $\pm 2\sigma$ uncertainty, found in Table 4-2. Measurements with the CRANK system are nearly indistinguishable from one another and the OSTR IC data, all of which are well within the 2σ uncertainty associated with the FN model using OSTR BOL values and associated uncertainty.

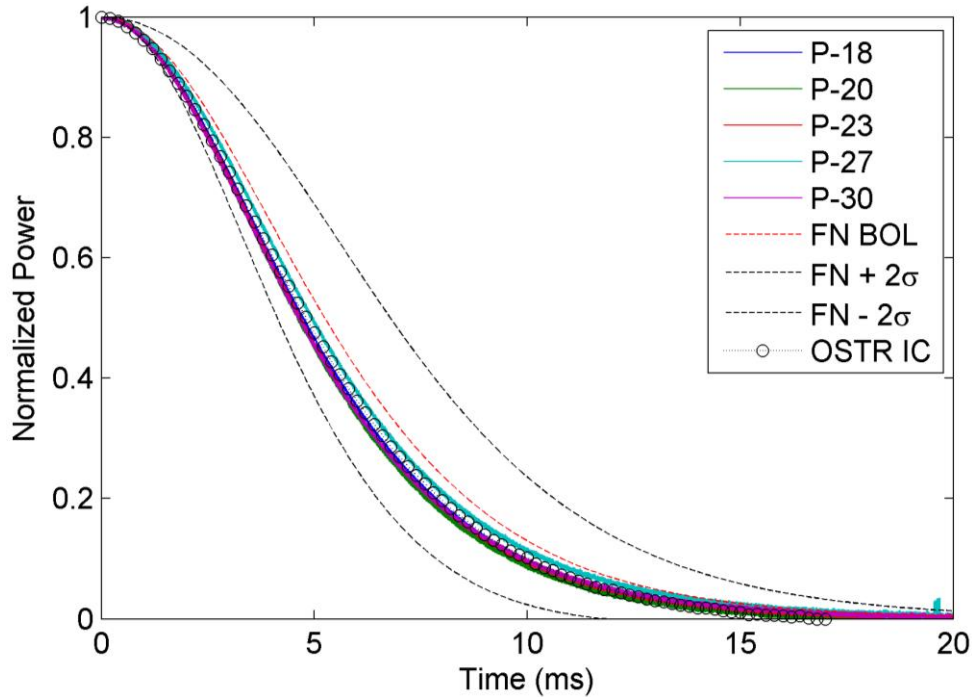


Figure 6-22. \$2.00 pulse comparison with OSTR BOL uncertainty

Figure 6-23 provides the same comparison for \$2.00 pulses in OSTR from the CRANK system and the OSTR IC, but instead are collated with the FN model using the kinetics parameters for varying core lifetime, provided in Table 3-1. From observation of Figure 6-23, the OSTR IC and CRANK system data appear to more closely align with the FN MOL curve. However, recall that the FN model always predicts a less steep curve than a pulse shape profile from a reactor with varying temperature feedback. Therefore, as the OSTR core ages throughout its lifetime of approximately 70 years, experimental data from the OSTR IC and CRANK system become steeper and then reverse its trend to become less steep, as described previously in Section 3.2. Therefore, safeguards inspections using the CRANK system require a specified periodicity to accurately assess a facility's kinetics parameters.

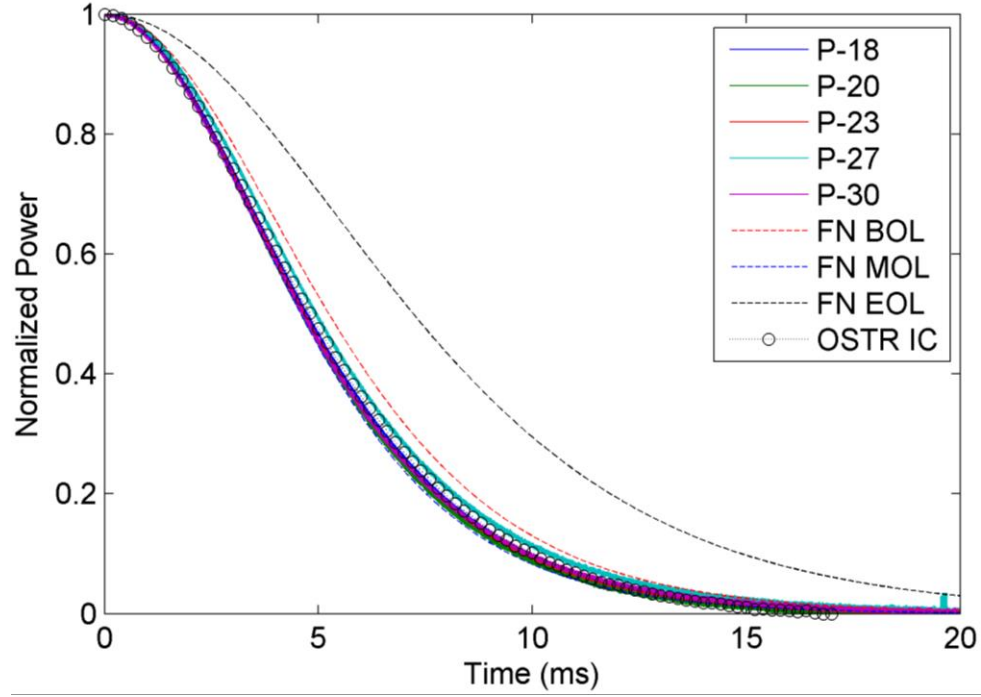


Figure 6-23. \$2.00 pulse comparison with varying core lifetime

The experimental data shown in Figure 6-17 through Figure 6-20 may be analyzed with the integral method for calculating the β/l ratio (3-35), shown below for reference.

$$\frac{\beta}{l} = \left(\frac{1}{(\$_2 - 1)^2 - (\$_1 - 1)^2} \right) \left(\frac{2(\$_2 - 1)^2}{I_1 (\$_1 - 1)} - \frac{2(\$_1 - 1)^2}{I_2 (\$_2 - 1)} \right) \quad (3-35)$$

$$I_n = \int_0^{\infty} \frac{P_n(t)}{P_{\max}} dt = \frac{2l}{\beta (\$_n - 1) (1 + H (\$_n - 1)^2)} \quad (3-33)$$

As shown in two unique measurements from Figure 6-13 and Figure 6-21, the core excess decreases during a typical operating week at OSTR, so the calculation of the β/l ratio using (3-35) is ill-suited to providing accurate results when pulses performed on Wednesday are utilized. Figure 6-24 through Figure 6-28 present a comparison of the calculated β/l ratio with associated uncertainty using two reactor pulses from Table 6-5 based on strength of pulse (large or small reactivity insertion) provided in the X and Y vectors, defined by (6-7) and (6-8), respectively, and core excess condition (high or low core excess). Details of uncertainty calculations are found in

Appendix C. In Figure 6-24 through Figure 6-28, each pair of pulses is used to calculate a β/l ratio by the matrix given as (6-9) and are compared to the declared OSTR FSAR BOL values, provided in Table 4-2. For Figure 6-24 through Figure 6-28, the pulse numbers are provided in green and purple to indicate pulses performed during a high core excess and low core excess condition, respectively.

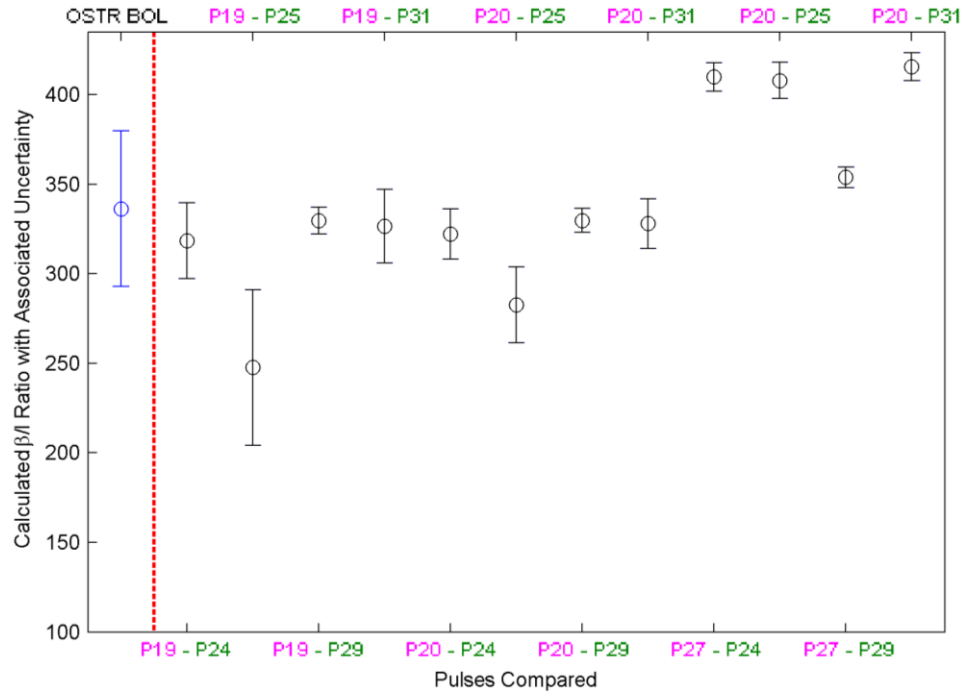


Figure 6-24. Calculation of β/l ratio with X2, Y1 pulse comparisons

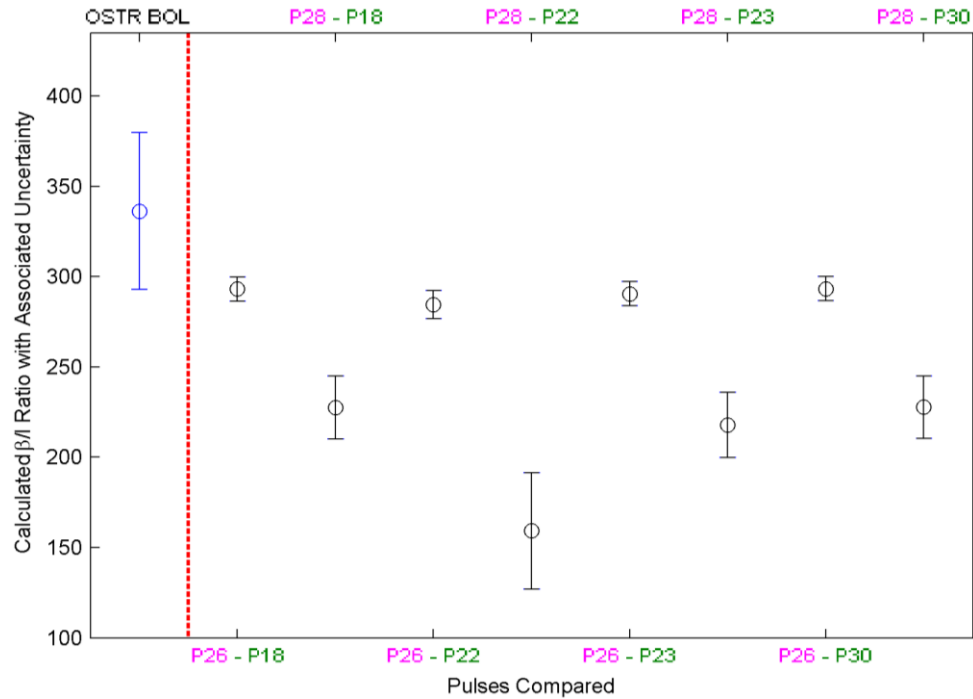


Figure 6-25. Calculation of β/l ratio with X1, Y2 pulse comparisons

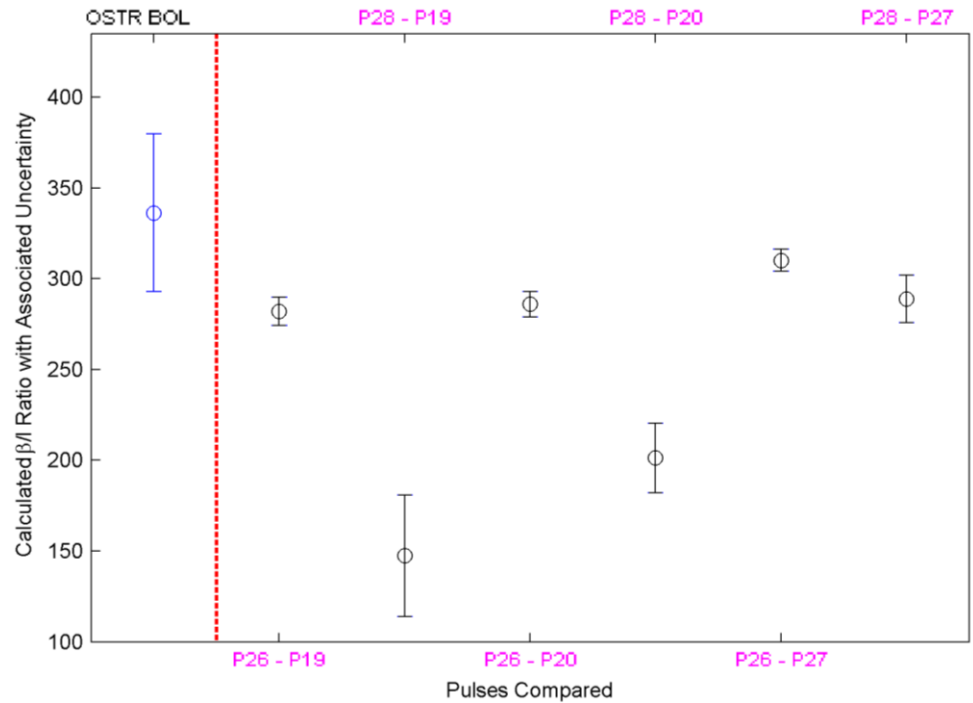


Figure 6-26. Calculation of β/l ratio with X2, Y2 pulse comparisons

For the calculations of the β/l ratio that include a pulse in a low core excess condition (purple), it is clear that the determined values are largely inconsistent as a result of decreasing transient rod worth with increased days of operation in a week at OSTR. However, when only pulses performed in a high core excess condition (green) are compared, displayed in Figure 6-27, the results become much more consistent over a wide variety of reactivity insertions, except for pulse comparisons that involve P-25. As noted earlier in Table 6-4, P-25 was the last performed pulse on 30 January 2017 and four large pulses were performed prior to P-25, reducing the transient rod worth through fission product buildup or slight temperature increase from repeated, large Δ reactivity insertions.

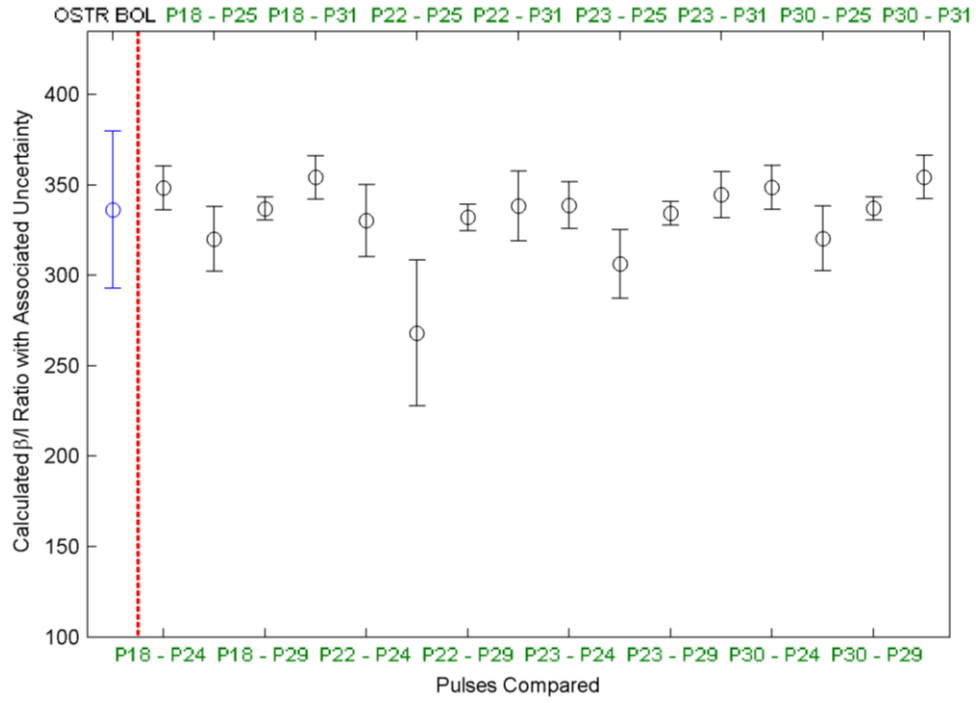


Figure 6-27. Calculation of β/l ratio with X1, Y1 pulse comparisons

Based on this knowledge of OSTR operations and transient control rod worth, it becomes of interest to compare the smallest reactivity inserted in a high core excess condition, P-29, with the largest reactivity insertions in a high core excess condition, P-18, P-22, P-23, and P-30, which reduces Figure 6-27 to Figure 6-28, which reveals

a very consistent measurement of the β/l ratio. The individual values of the β/l ratio and associated uncertainty are provided in Table 6-6.

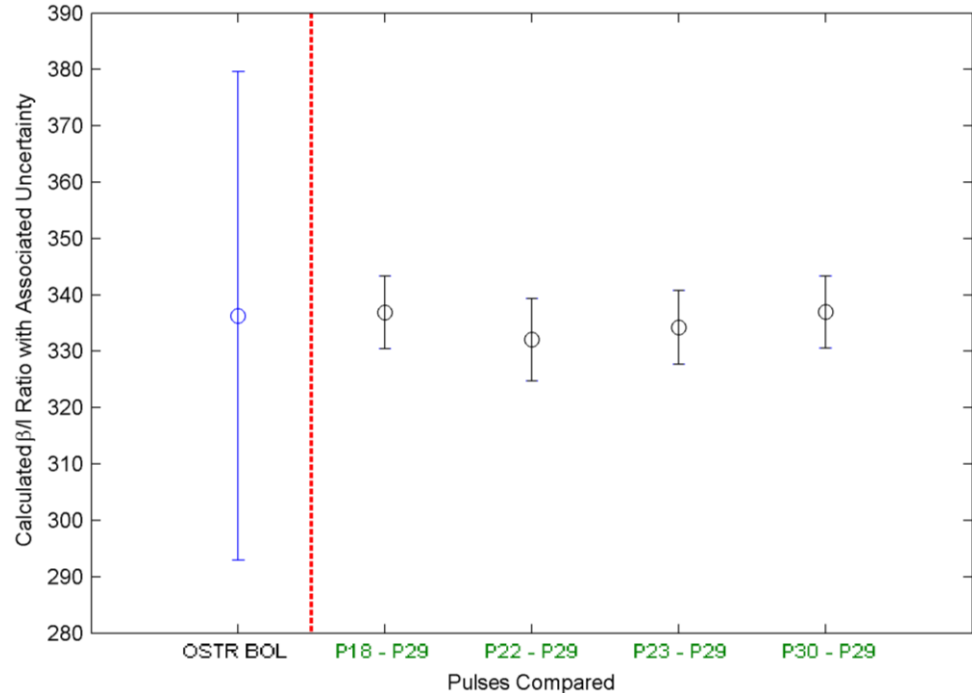


Figure 6-28. Calculation of β/l ratio with selected X1, Y1 pulse comparisons

Table 6-6. Calculated β/l ratio for pulses in Figure 6-28

Pulses Compared	β/l ratio	Uncertainty (2σ)
OSTR FSAR BOL [106]	336	43
P18 – P29	336.9	6.4
P22 – P29	332.0	7.3
P23 – P29	334.3	6.5
P30 – P29	337.0	6.4

The values in Table 6-6 represent individual measurements of the β/l ratio of the OSTR at distinct times in its core lifetime, and cannot be combined to create an average value of β/l for the OSTR. In fact, this result shows the potential for the CRANK system to be utilized as a facet of safeguards inspections at nuclear facilities, since the value of β/l is largely unchanged in the OSTR, which does not possess any

material diversion motivations. The values in Table 6-6 are very similar, despite undeniable, small changes in fissile material content even over a short timespan (~ 1 year) when compared to its core lifetime (~ 70 years). The NI PXIe-5171R allowed the collection of the Thorlabs PDA25K voltage output at a maximum sample rate of 250 MHz for all pulses specified in Table 6-4. However, it is of interest to examine the impact of reducing the sample rate to provide a limit for instrumentation requirements in the context of a safeguards inspection, since the calculated β/l ratio and the measurement uncertainty has an impact on the ability to detect a significant quantity of fissile material of interest in a timely manner. Figure 6-29 depicts the effect of decreasing sample rate from a maximum of 250 MHz on the β/l ratio and associate uncertainty. The data for Figure 6-29 were computed by reducing the number of data points in P-29 and P-30 and recalculating the β/l ratio using (3-35), which utilized the trapezoidal integration method, and uncertainty analysis in Appendix C.

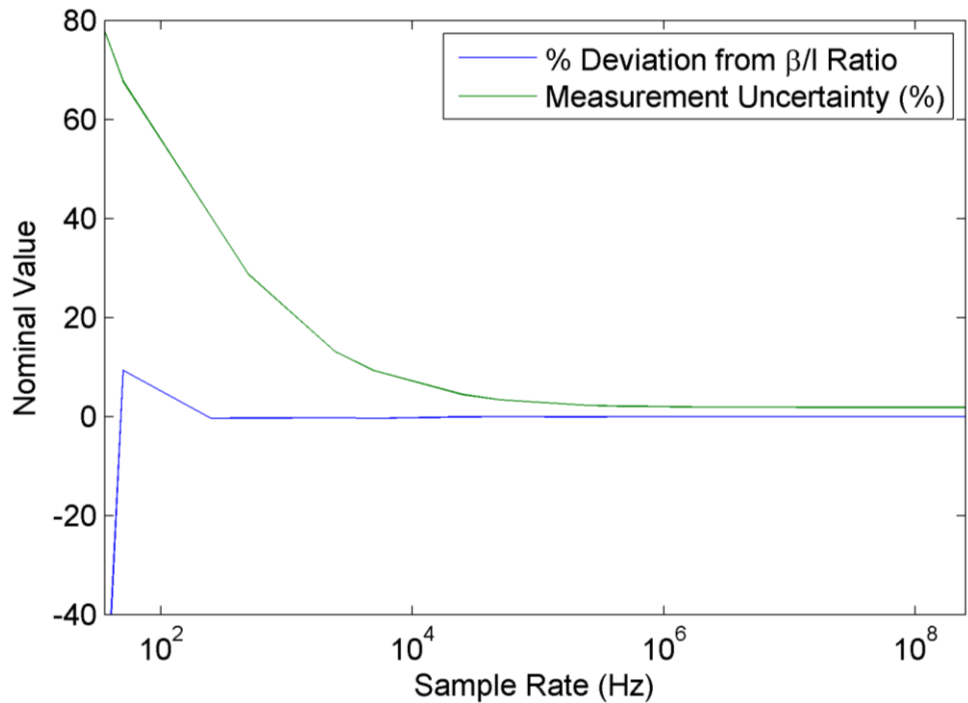


Figure 6-29. Calculation of β/l and uncertainty with varying sample rate

6.2.3 Simulations

It is imperative to explore the viability of an experimental situation with computational simulations to confirm the physical phenomena observed by instrumentation, and confirmation allows the further simulation of experiments with confidence. Figure 6-30 provides a tally using MCNP6.1.1 [95] for Cherenkov photons using the index of refraction based on the Sellmeier relation [92]. The MCNP geometry included the entire OSTR along with a single tally for photons with energy characteristic of Cherenkov light at a reactor power level of 1 MW. The tally was positioned at the approximate location of the optical lens for the CRANK system per the depiction in Figure 4-15 and Figure 4-16. From observation of Figure 6-30, the normalized photon intensity provided by the MCNP simulation (red) is compared to the responsivity of the Thorlabs PDA25K (blue), with the product of the two curves shown in black to provide the spectral detection efficiency of the CRANK system based on the MCNP simulation.

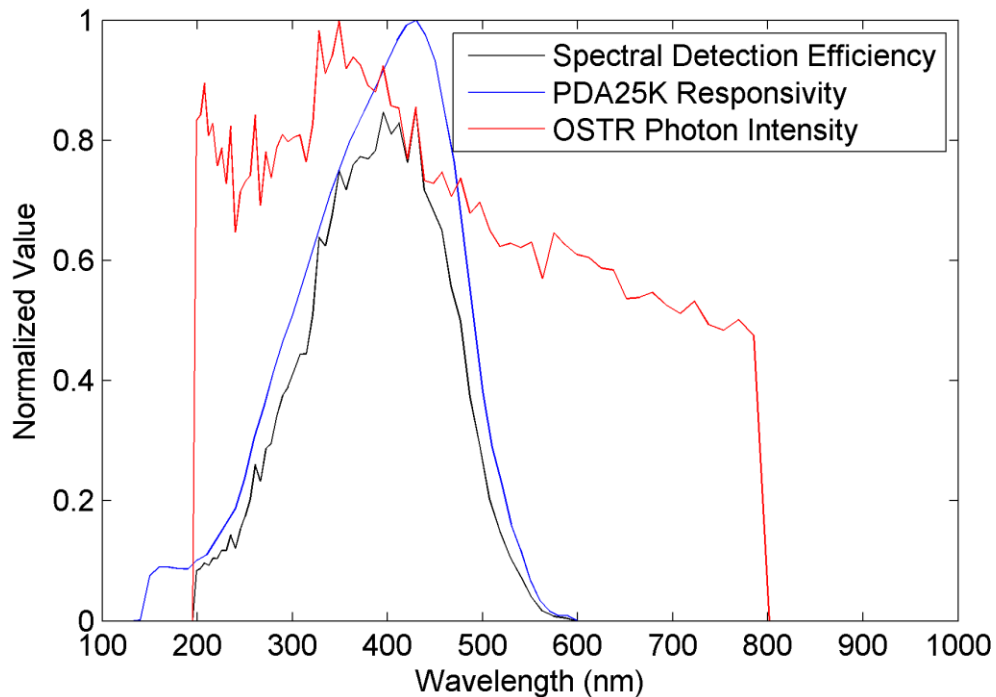


Figure 6-30. Cherenkov photon tally in OSTR at lens position

It is possible to calculate the total photons measured by the Thorlabs PDA25K by integrating the normalized spectral detection efficiency, shown in black in Figure 6-30, across all wavelengths and multiply by the total number of Cherenkov photons tallied by MCNP6.1.1 at the approximate location of the PDA25K photodiode during OSTR experiments. This value can be then compared to the PD response to a known light intensity from the Thorlabs M365FP1 LED light source to confirm the ability of MCNP6.1.1 Cherenkov physics package to accurately predict Cherenkov light intensity during reactor operations, validating the future use of MCNP simulations to predict PD response in the CRANK system configuration. From Section 4, the instrumentation used as part of the CRANK system attenuates the Cherenkov light observed in the reactor, and it was found that a \$2.00 reactivity insertion in the OSTR elicited a peak response of 2.5 V from the Thorlabs PDA25K photodiode.

Table 6-7 provides MCNP Cherenkov tally and conversion factors to estimate the number of Cherenkov photons detected by the CRANK system during OSTR experiments. The MCNP6.1.1 simulation from OSTR geometry emitted 2.82×10^9 Cherenkov photons, with a tally fraction of 0.0012127 at the approximate position of the Ocean Optics lens about 6 feet above the OSTR reactor core. Additionally, the number of source neutrons used in the MCNP simulation was 1×10^7 , as compared to a typical neutron flux of 1×10^{13} neutrons per $\text{cm}^2\text{-s}$ at an OSTR power level of 1 MW, with the MCNP6.1.1 simulation specified control rod heights based on the OSTR rod worth curves. However, during a \$2.00 reactivity insertion with a high core excess condition, the OSTR reactor power can reach 1800 MW. Using these conversion factors and the MCNP Cherenkov tally value, it is possible to estimate the number of Cherenkov photons that are incident on the face of the Ocean Optics lens, the first component of the CRANK system to interact with the Cherenkov light emitted by the OSTR. The result of this calculation yields approximately 6.15×10^{15} Cherenkov photons, as shown in the last entry in Table 6-7.

Table 6-7. MCNP Cherenkov tally and conversion factors

Parameter	Value
MCNP Cherenkov production	$2.82 \times 10^9 \gamma$
MCNP tally fraction	1.2127×10^{-3}
Neutron source	1×10^7 neutrons
Typical neutron flux in OSTR at 1 MW	$1 \times 10^{13} \text{ n}/(\text{cm}^2\text{-s})$
MCNP power level	1 MW
Peak power level in \$2.00 transient	1800 MW
Approximate number of Cherenkov photons incident on CRANK system	$6.15 \times 10^{15} \gamma$

To determine the number of photons that are recorded by the CRANK system, it is necessary to account for attenuation of Cherenkov light in each system component, listed in Table 6-8. The Ocean Optics lens used in the CRANK system, detailed in Section 4.4, is composed of Suprasil glass, and Figure 4-10 provides the approximate transmission percentage of light at typical Cherenkov wavelengths. Next, the Thorlabs BF20HSMA01 fiber bundle, detailed in Section 4.3, constitutes of 7 individual fiber bundles, with an active area of 56 percent of its total area. Additionally, the fiber bundle attenuates Cherenkov light, shown in Figure 4-7, with a loss of approximately -0.6 dB for a 4 meter length of cable. Finally, the Thorlabs PDA25K GaP photodiode, detailed in Section 4.2, is composed of gallium phosphide, which possesses a quantum efficiency of approximately 40 percent. Then, the spectral detection efficiency of the PDA25K photodiode, found from the integration of the black curve in Figure 6-30. The ratio of the detectable light fraction to the total emitted Cherenkov light photons is computed to determine the spectral detection efficiency of approximately 0.42. The inclusion of the attenuation factors in Table 6-8 allows for the total number of photons recorded by the CRANK system to be

calculated from the number of Cherenkov photons incident on the Ocean Optics lens, equivalent to approximately 2.7×10^{14} photons.

Table 6-8. Instrumentation attenuation factors

Parameter	Instrument	Value
Suprasil glass transmission fraction	Ocean Optics Lens	0.92
Area Ratio of fiber bundle	Fiber Bundle	0.56
Fiber bundle attenuation	Fiber Bundle	-0.6dB = 0.502
Quantum efficiency of gallium phosphide	Photodiode	0.4
Spectral detection efficiency	Photodiode	0.42465
Approximate Cherenkov number of photons recorded by CRANK system		$2.7 \times 10^{14} \gamma$

The result in Table 6-8 can be compared to the Cherenkov light intensity in a desktop setting by employing the Thorlabs M365FP1 LED light source, which is calibrated at Thorlabs by applying a 1400 mA current to LED and measuring photon output through a single strand 400 μm diameter core fiber (Thorlabs FT400EMT). The output area of the LED is greater than this fiber strand (area 2.0 mm^2), so the fiber effectively blocks a large amount of signal. The fiber bundle purchased as part of this work (Thorlabs BF20HSMA01) has a diameter of 2.0 mm, so the amount of light that travels through the fiber from the LED is increased by the ratio of the fiber bundle diameters.

Table 6-9 provides the PD and LED conversion factors for calculation of number of photons recorded by the CRANK system. From a 1400 mA current input, the Thorlabs LED light source emits approximately 15.5 mW of optical power. However, to elicit a 2.5 V signal output from the Thorlabs PDA25K, equivalent to the response

from a \$2.00 reactivity insertion in the OSTR, it is necessary to apply 1.6 mA of optical power, reducing the optical power output. The fiber bundle used in the CRANK system has an area ratio of 7.41125 as compared to the fiber strand used by Thorlabs to calibrate their optical power output. From these factors, the optical power output of the M365FP1 LED light source using the BF20HSMA01 fiber bundle may be calculated. The LED emits photons at wavelengths of approximately 365 nm, or photons with energy of 3.3 eV. Then, the approximate number of photons recorded by the CRANK system in a desktop setting may be calculated as 2.48×10^{14} , which shows good agreement with the estimated 2.7×10^{14} photons observed as part of the OSTR experiments at the pulse peak of a \$2.00 reactivity insertion with a similar response in the PDA25K for an applied current of 1.6 mA to the LED light source.

Table 6-9. PD conversion factors

Parameter	Value
Thorlabs tested amperage	1400 mA
Thorlabs optical power output	15.5 mW
Current to elicit 2.5 V signal	1.6 mA
Area Ratio	7.41125
Energy of photon at 365 nm	3.3 eV
Approximate number of photons recorded	$2.48 \times 10^{14} \gamma$

6.2.4 OSTR Conclusions

The results from the OSTR experiments, found in the Figure 6-24 through Figure 6-28, with the most qualified experiments detailed in Table 6-6, have shown that the CRANK system is capable of determining the ratio of reactor kinetics parameters in a NDA assay of a research reactor capable of pulsing through the measurement of Cherenkov light. There exists excellent agreement between the declared value of the

β/l ratio in the OSTR FSAR for BOL values and four separate reactor pulse comparisons using the CRANK system in Table 6-6.

The introduction of a modification to the existing FN model has provided the ability to estimate the temperature feedback based on a feedback coefficient and the dollar value of reactivity insertion to accommodate the variable heat capacity in an operating reactor with a strongly negative temperature coefficient of reactivity.

7 PROLIFERATION RESISTANCE

As discussed in the original objectives, the goal of the CRANK system is to create a specific methodology to determine the reactor kinetics parameters, which is ultimately a measure of reliability for the absence of material diversion activities. Reactor fuel in its initial state prior to introduction into a reactor core usually is composed of a specified amount of uranium. The ratio of the two main isotopes of uranium, U-235 and U-238, composes the enrichment percentage. The OSTR was converted in 2008 to Low Enriched Uranium (LEU) fuel, or a ratio of U-235 to U-238 of less than 20 percent; in the case of the OSTR, this ratio is 19.75 percent at BOL. As the reactor is operated, U-235 is fissioned by neutrons, creating fission products, thermal heat, and more neutrons, allowing for a chain reaction to occur. At the same time, U-238, though its fission cross section is not large for thermal neutrons, can absorb neutrons and transmute into U-239 with a half-life of 23 minutes [6] and decays into Np-239, which then decays with a half-life of 2.3 days [6] into Pu-239, a fissile isotope that is capable of being reprocessed using separation techniques. Different isotopes of fissile material possess differing, unique values of β , the delayed neutron fraction, and inference of this parameter through measurement techniques can lead to identification of the fissile material present in a specimen. In a nuclear reactor, as the quantity of U-235 is depleted as a result of facility operations, the quantity of Pu-239 is increased, changing the β value over the core lifetime. Additionally, if fissile material is removed during the core lifetime, the result is an impact on the value of β . Increased power levels to obtain a faster production of Pu-239 also alters the value of β .

The objectives of IAEA safeguards include maintaining continuity of knowledge of fissile material, including U-235 and Pu-239, in non-nuclear weapon states, and the amount of material determined to be of interest to the IAEA, a significant quantity, governs the time interval of inspections for a facility under IAEA safeguards. Therefore, it of interest to the IAEA to determine the β value to ascertain the relative fissile material content in the reactor, per (3-5). The CRANK system is uniquely

qualified to provide a repeatable NDA technique in a pulsed reactor facility with minimal reliance on facility operations through analysis of the transient pulse shape.

However, recall that the CRANK system does not measure β . Instead, the β/l ratio is measured, and, according to the (2-2) and (2-4), the prompt neutron lifetime is impacted by a variety of factors, which makes its characterization at a given point in core lifetime difficult to perform. As a result, it is recommended that as part of safeguards regime, the CRANK system be implemented in a periodic interval to provide measurements over a reactor core's history and minimize the proliferation risk of a reactor facility.

If the CRANK system is utilized in a safeguards program for a facility, it is then necessary to address the impact of falsified documentation and intentional facility actions to prevent detection of material diversion. Acts of material diversion in a reactor core have an impact on the β/l ratio, and during an inspection and measurement with the CRANK system, there are two scenarios to be detailed. If facility operators implement the requested reactivity insertion and have been performing material diversion activities, there is an obvious, distinct difference in the resulting β/l ratio. Recall Figure 6-26, in which the CRANK system measurements were used to calculate β/l ratios substantially different from the declared OSTR values due to the difference in transient control rod worth on a Wednesday as compared to its calibration on a Monday. In this case, the IAEA safeguards program would be able to report a discrepancy in the facility operations.

Next, the facility operators could potentially falsify documents, including the rod worth calibration curves and the declared reactor kinetics parameters. By falsifying the rod worth calibration and inserting a “compensated” amount of reactivity in an attempt to mask material diversion activities, the pulse shape and maximum power are altered. These properties of a reactor pulse are inversely proportional, and can

provide evidence of material diversion through the concepts in (7-1) and (7-2), which are found through the derivation of (3-35) for two measured reactor pulses.

$$\frac{P_{\max,1}}{P_{\max,2}} = \frac{(\$_1 - 1)^2 (1 + H (\$_1 - 1)^2)}{(\$_2 - 1)^2 (1 + H (\$_2 - 1)^2)} \quad (7-1)$$

$$\begin{aligned} \int_0^{\infty} \frac{P_1(t)}{P_{\max,1}} &= \frac{(\$_2 - 1)(1 + H (\$_2 - 1)^2)}{(\$_1 - 1)(1 + H (\$_1 - 1)^2)} \\ \int_0^{\infty} \frac{P_2(t)}{P_{\max,2}} &= \end{aligned} \quad (7-2)$$

The formulation in (7-2) has been previously discussed and is the source of the CRANK system's methodology for determining the β/l ratio, and additional analysis of the reactor pulses with (7-1) showed excellent agreement with measurements in the OSTR from Table 6-4, and allowed the prediction of a high/low core excess reactivity insertion simply based on its relationship to pulses performed in the same day. However, in a safeguards capacity, (7-1) predicts a slightly different relationship from (7-2) in the properties from two reactor pulses and makes it increasingly difficult to ensure agreement with both relations when measurements from two reactor pulses are compared to calculate the β/l ratio.

Through manipulation of the intended reactivity insertion (\$), it is possible to produce a reactor pulse profile identical to that of the requested reactivity insertion. In this way, the calculation of the β/l ratio does not indicate material diversion per the calculation in (3-35), used previously in Section 6.2.2 to compute the β/l ratio in the OSTR.

The relation in (7-2) is rearranged to find the quantity H in (7-3), which represents a deviation from the FN model and is constant for a particular reactor under the same operating conditions (i.e. reactor pulses performed in a high core excess condition), a property used to determine the β/l ratio in Section 6.2.2.

$$H = \frac{I_2(\$_2 - 1) - I_1(\$_1 - 1)}{I_1(\$_1 - 1)^3 - I_2(\$_2 - 1)^3} \quad (7-3)$$

Following the determination of this quantity, data collected during OSTR experiments are used to compute the ratio of the pulse peaks, which showed excellent agreement with OSTR instrumentation for monitoring power during OSTR experiments. In order to conceal material diversion activities, it is expected that reactor operators would attempt to insert a compensated amount of reactivity, which alters (7-1) and (7-2) to (7-4) and (7-5) through the replacement of $(\$-1)$ by $N(\$-1)$, where N is the adjustment to the requested reactivity insertion for each respective reactivity insertion.

$$R_2 = \frac{P_{\max,1}}{P_{\max,2}} = \frac{N_1^2 (\$_1 - 1)^2 (1 + HN_1^2 (\$_1 - 1)^2)}{N_2^2 (\$_2 - 1)^2 (1 + HN_2^2 (\$_2 - 1)^2)} \quad (7-4)$$

$$\frac{I_1}{I_2} = \frac{\int_0^\infty \frac{P_1(t)}{P_{\max,1}}}{\int_0^\infty \frac{P_2(t)}{P_{\max,2}}} = \frac{N_2 (\$_2 - 1) (1 + HN_2^2 (\$_2 - 1)^2)}{N_1 (\$_1 - 1) (1 + HN_1^2 (\$_1 - 1)^2)} \quad (7-5)$$

In a material diversion scenario, it is desirable to choose N values to make the quantity in (7-5) identical to the quantity based on the requested reactivity insertion values in (7-2). If the values of N are not chosen adequately, the value of the β/l ratio will not match the declared reactor kinetics parameters, and the detection of material diversion activities will be readily obvious. However, in a facility with a smart, focused adversary and a dedicated objective of material diversion, it is possible to choose N effectively for each reactor pulse. But, even if N is chosen to match the relations in (7-2) and (7-5), a discrepancy will exist between the relations in (7-1) and (7-4). Therefore, the detection limit for fissile material mass corresponds to the compensated reactivity insertion (N) resulting in a calculated ratio of the maximum peak values exceeding the predicted value of (7-1) including predicted uncertainty.

It is also important to remember that a safeguards program has a multitude of tools to implement, and the CRANK system, though it is capable of a beneficial impact, is only a single instrument. The strength of an IAEA safeguards program is the comprehensive assessment allowed by a variety of instruments and techniques.

7.1 Case Study – OSTR

In a facility under IAEA safeguards, each technique is designed to determine characteristics of a specific attribute of the facility operations. For the demonstration of the CRANK system's capabilities in the OSTR, the relationships provided in (7-1) and (7-2) are used to determine the detectable amount of fissile material as a result of material diversion. In a facility that is attempting to divert fissile material or produce additional fissile material as a result of sample irradiations, the total fissile material content of the reactor will be altered from its declared state. The OSTR properties found in Table 7-1 are used to calculate the total mass of fissile material in the OSTR at BOL [106].

Recall from Section 6.2.2 that Cherenkov light measurements in the OSTR were kept or discarded based on the reliability of the control rod worth for each pulse (i.e. core excess condition and repetition of large \$ pulses). For the case study of proliferation resistance in the OSTR, the comparison of P-29 and P-30 provided excellent agreement of the β/l ratio from the OSTR FSAR [106] and can be used to determine the quantity of fissile material that must be displaced to exhibit a quantifiable difference in the ratio of pulse peaks.

Table 7-1. OSTR Fuel Rod Properties

Dimension	Quantity
Fuel Element Inner Diameter (cm)	0.635
Fuel Element Outer Diameter (cm)	3.6449
Fuel Element Height (cm)	38.1
TRIGA Fuel Density (g/cm ³)	7.18
Number of Fuel Elements	85 + 2 (FFCR)
Weight Percent of Uranium in TRIGA Fuel	30
Weight Percent of U-235 in Uranium	19.75
U-235 Mass per Fuel Element (g)	163.99
Total U-235 Mass in OSTR (kg)	14.26

For the OSTR, a facility with no material diversion ambitions, the data collected during OSTR experiments are assessed for the potential amount of material that could be diverted without exceeding the limit determined by (7-4) and (7-5). The value of H is determined by (7-3) utilizing experimental data from OSTR experiments P-29 and P-30. However, the propagation of uncertainty through (7-3) must be included when assessing the detectable fraction of fissile material, with the detailed sensitivity analysis of H is found in Appendix C. Optimal values of N_1 and N_2 are found by matching the integral in (7-6) through (7-7) for a given deviation in the β/l ratio, denoted as X . The detection limit of the CRANK system applied in this capacity is calculated by the maximum values of X , N_1 , and N_2 that satisfy (7-4) within experimental uncertainty of (7-1).

$$I_1 = \int_0^{\infty} \frac{P_1(t)}{P_{\max,1}} dt = \frac{2X \left(\frac{l}{\beta} \right)}{N_1 (\$_1 - 1) \left(1 + H N_1^2 (\$_1 - 1)^2 \right)} = \frac{2 \left(\frac{l}{\beta} \right)}{(\$_1 - 1) \left(1 + H (\$_1 - 1)^2 \right)} \quad (7-6)$$

$$N_1^3 \left(H X (\$_1 - 1)^2 \right) + N_1 X - \left(1 + H (\$_1 - 1)^2 \right) = 0 \quad (7-7)$$

In a research reactor, a relevant material diversion scenario is the disposition of reactor fuel or the introduction of fertile isotopes to obtain plutonium, and ultimately

Pu-239. For nonproliferation and safeguards purposes, the value of X represents the detectable limit of the CRANK system for this case study, with final results shown in Table 7-2. The result in Table 7-2 indicates that a difference in fissile material content of approximately 200 g of results in irreconcilable differences in the pulse peak ratios while maintaining the correct pulse shape. It is important to recognize that the results in Table 7-2 are found from a comparison of a single pair of reactor pulses, P-29 and P-30, in the OSTR and should not be used as an advertised detection limit, but instead to demonstrate the capability of the method. Additional reactor pulses performed at other pulse-type research reactors would need to be completed as part of a rigorous validation and verification campaign for the CRANK system to obtain a high confidence in the CRANK system as an IAEA inspection technique.

Table 7-2. Detectable Limit using P-29 and P-30

Dimension	Quantity
Detectable Fraction of β/l ratio (X)	0.986
Detectable Fraction of Fissile Material (g)	198.4

7.2 Proliferation Resistance Summary

The CRANK system methodology, as applied to nuclear safeguards, is summarized in Figure 7-1. Recall that the CRANK system is applicable to a research reactor facility with an open-pool configuration with pulsing capabilities that is under IAEA safeguards. As part of its facility obligations to the NPT and Additional Protocol, the research facility will declare its total amount of fissile material and its ratio of reactor kinetics parameters. The CRANK system will then measure the Cherenkov light emitted by two unique reactor pulses. Based on the pulse integrals and the associated system uncertainty, the measured ratio of kinetics parameters may be compared against the declared values. Then, the peak ratios and associated uncertainty may be applied with the declaration of fissile material amount to create the detection limit, or

the relative detectable fraction of fissile material, shown previously for the OSTR case study in Table 7-2.

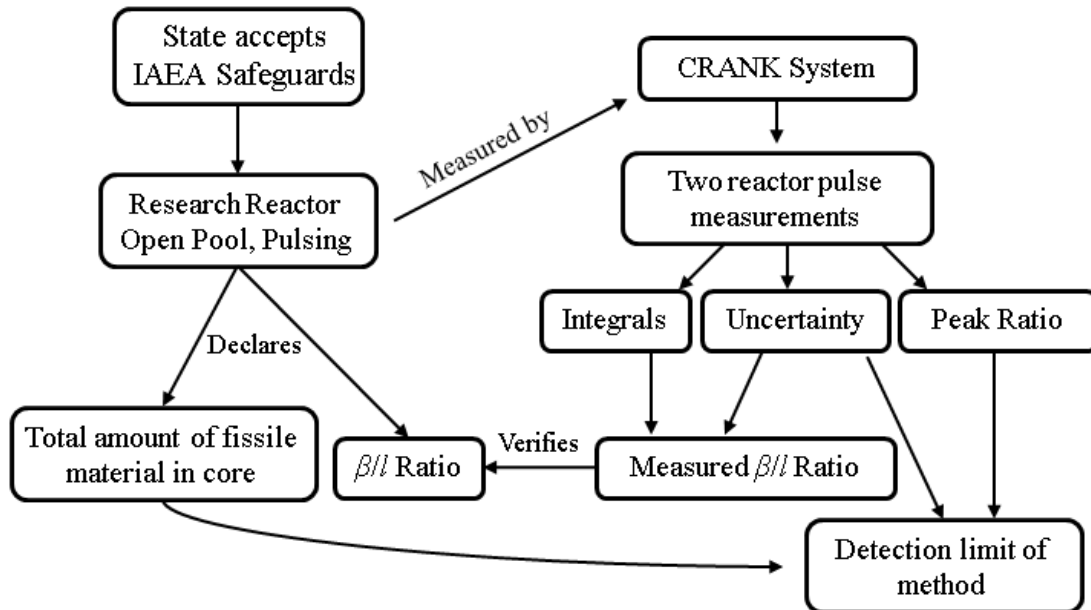


Figure 7-1. CRANK System Detection Methodology

8 CONCLUSIONS

The development of the CRANK system has shown the viability of determining reactor kinetics parameters for nonproliferation in an operating research reactor based on the limitations presented in Section 8.3. This investigation leads a novel method for determining reactor kinetics parameters in an operating research reactor for the purpose of nonproliferation through the NDA technique of a naturally-occurring phenomenon. Although many inspection techniques currently exist, this method fulfills a recognized need by the international safeguards community, which is the identification of bias defects in research reactors.

Additionally, the methodology identified as part of the CRANK system's function can be applied to research reactors without material diversion aspirations to determine the facility's reactor kinetics parameters with higher confidence by independently confirming computational tools or other experimental methods.

8.1 Observations

An extensive review of NDA inspection techniques employed by the IAEA was performed, with a specific emphasis on the current methods that utilize the measurement of Cherenkov light. Additionally, a review of the current methods for the determination of reactor kinetics was conducted. Despite the vast literature on these two topics, there is yet to be a reliable method to accurately determine reactor kinetics parameters independent of a facility's instruments with the intent of nuclear nonproliferation. There were three objectives that governed the development of the CRANK system.

1. Leverage existing technology to measure Cherenkov light with a non-intrusive, in-core technique through assembly of a new detecting system.
2. Validate measurement of Cherenkov light as a safeguards technique to observe reactor power during reactivity insertions above delayed critical.
3. Analyze results based on fundamental reactor kinetics relationships

All three objectives were met. Cherenkov light was shown to provide a proportional response to reactor power above a lower limit of detection in a repeatable fashion, which was used to analyze Cherenkov light measurements with a theoretical reactor power equation, the PRKEs. The most impactful outcome of this work is in regards to the CRANK system methodology, which employs a modified version (varying temperature feedback) of the traditional FN model, a solution to the PRKEs that assumes constant temperature feedback terms. The methodology developed herein is not limited to a safeguards technique. In fact, a research reactor with pulsing capabilities can utilize the method to independently acquire an experimental reactor kinetics parameter ratio.

8.2 Relevance of Work

The CRANK system and associated methodology developed herein represents an initial step in the deployment of a novel inspection technique for international safeguards that fulfills the ideal requirement of non-intrusive, in-core measurements. This study objectively provides a new solution to the PRKEs when modeling a reactor transient through modifications based on empirical evidence to estimate varying temperature feedback.

8.3 Assumptions and Limitations

The CRANK system has provided valuable insights for the ability to discern reactor kinetics parameters using Cherenkov light for the purpose of nuclear safeguards and nonproliferation, but is limited by a few factors.

8.3.1 Reactor Type

The OSTR experiments utilized during the CRANK system's testing campaign were performed in the OSTR, which is an open-pool, TRIGA Mk-II reactor, as described previously in Section 4.1. Since the CRANK system is designed to detect the

wavelengths of Cherenkov light to provide a proportional response to reactor power, a direct line of sight must be maintained throughout the reactivity transient.

Additionally, the CRANK system may be implemented only in reactors that possess a pulsing capability. The pulse shape from a reactivity insertion exceeding the delayed neutron fraction is necessary to assess the β/l parameter ratio.

8.3.2 Reactivity Limitations

The reactivity insertions requested during the OSTR experiment were specifically chosen to verify the OSTR reactor kinetics parameters with a low value of uncertainty, shown in Figure 6-11. From Table B-2 in Appendix C, pulse values as low as \$1.05 were attempted as part of the validation of the CRANK system. However, a low S/N ratio was observed, and, potentially, the relatively long duration of a small \$ reactor pulse might preclude the use of the FN or modified FN model proposed in this work due to the contribution of delayed neutrons to reactor power and, therefore, Cherenkov light during the reactor pulse.

8.4 Future Work

To expand upon the viability of the CRANK system and its potential application for safeguards, future work would involve a testing campaign utilizing research reactors in the U.S., ideally pulsed-type reactors similar to the OSTR TRIGA Mk-II in order to further validate the methodology used by the CRANK system in the OSTR.

Additionally, other modes of detection using neutron- or gamma-sensitive detection equipment at a high sample rate based on Figure 6-29 are plausible by implementing the novel mathematical model in 3.2.3 considering the excellent agreement between the measurement comparison of OSTR IC and CRANK experimental data in Figure 6-22 and Figure 6-23. These methods may be necessary in a reactor with pulsing capacity, but without a dielectric medium to create Cherenkov light during the reactor

pulse. Additionally, in the case of neutron detectors, it is critical to determine proper measurement locations, since the neutron mean free path changes with neutron energy and produce a “smeared” pulse, which will not produce an accurate representation of the pulse shape.

9 BIBLIOGRAPHY

1. Doyle, J.E., *Nuclear Safeguards, Security, and Nonproliferation*. 2008, New York: Elsevier Press.
2. Reilly, D., et al., *Passive Nondestructive Assay of Nuclear Materials*. NUREG/CR-5550 (LA-UR-90-732). 1991: Washington, DC.
3. Albright, D., *North Korean Plutonium Production*. Science & Global Security, 1994. **5**: p. 63-87.
4. Dreicer, J., *Estimated Feasible Plutonium Production in North Korea's Research Reactor, IRK-DPRK*. LA-13211-MS, 1997: Los Alamos, NM.
5. Attas, E.M., Chen, J.D., Young, G.J., *A Cherenkov Viewing Device for Used Fuel Verification*. Nuclear Instruments and Methods in Physics Research A, 1990. **299**(1-3): p. 88-93.
6. Duderstadt, J.J., Hamilton, L.J., *Nuclear Reactor Analysis*. 1976, New York: John Wiley & Sons, Inc.
7. Arkani, M., Gharib, M., *Reactor Core Power Measurement Using Cherenkov Radiation and Its Application in Tehran Research Reactor*. Annals of Nuclear Energy, 2009. **36**(7): p. 896-900.
8. Cerenkov, P.A., *Visible Radiation Produced by Electrons Moving in a Medium with Velocities Exceeding that of Light*. Physical Review, 1937. **52**: p. 378-381.
9. *The Statute of the IAEA – As Amended up to 28 December 1989*. Vienna, Austria.
10. *The Agency's Safeguards*. INFCIRC/26. 1961: Vienna, Austria.
11. *The Agency's Safeguards System*. INFCIRC/66. 1965: Vienna, Austria.
12. *The Structure and Content of Agreements Between the Agency and States Required in Connection with the Treaty on the Non-proliferation of Nuclear Weapons*. INFCIRC/153. 1972: Vienna, Austria.
13. *Safeguards Techniques and Equipment: 2011 Edition*. International Nuclear Verification Series, Revision 2. **1**, 2011: Vienna, Austria.
14. Nassef, M.H., et al., *Determination of Plutonium Isotopes in Standard IAEA Reference Materials by Destructive Analytical Technique*. Journal of Nuclear and Radiation Physics, 2008. **3**(1): p. 21-30.

15. IAEA *Safeguards Glossary, 2001 Edition*. International Nuclear Verification Series No. 3, International Atomic Energy Agency, Vienna, Austria, 2002.
16. Boyer, B.D., *The Rudiments of IAEA Safeguards and an Introduction to the Key Role of the Inspector*, in *Nuclear Forensics Undergraduate Summer School 2010*. LA-UR-09-00207. 2009: Las Vegas, Nevada.
17. Croft, S., Nicholson, A., Favalli, A., *The Art of Uncertainty Quantification for Nondestructive Assay*, Nuclear News, **59** (10), September 2016, p. 40-42.
18. Tobin, S.J., et al., *Next Generation Safeguards Initiative Research to Determine the Pu Mass in Spent Fuel Assemblies: Purpose, Approach, Constraints, Implementation, and Calibration*. Nuclear Instruments and Methods in Physics Research A, 2011. **652**: p. 73-75.
19. Chichester, D., *Introduction to Nuclear Safeguards – Nondestructive Analysis*, in *Oregon State University Nonproliferation Seminar Series*. INL/CON-09-16307. 2013: Corvallis, OR.
20. Khalafi, H., Mosavi, S.H., Mirvakili, S.M., *Design & Construction of a Digital Real Time Reactivity Meter for Tehran Research Reactor*. Progress in Nuclear Energy, 2011. **53**: p. 100-105.
21. Henzl, V., et al., *Determination of the Plutonium Content in a Spent Fuel Assembly by Passive and Active Interrogation Using a Differential Die-Away Instrument*. Nuclear Instruments and Methods in Physics Research A, 2013. **712**: p. 83-92.
22. Kaplan, A.C., et al., *Determination of Spent Nuclear Fuel Assembly Multiplication with the Differential Die-Away Self-Interrogation Instrument*. Nuclear Instruments and Methods in Physics Research A, 2014. **757**: p. 20-27.
23. Kaplan, A.C., et al., *Determination of Total Plutonium Content in Spent Nuclear Fuel Assemblies with the Differential Die-Away Self-Interrogation Instrument*. Nuclear Instruments and Methods in Physics Research A, 2014. **764**: p. 347-351.
24. Lestone, J.P., et al., *The Passive Nondestructive Assay of the Plutonium Content of Spent-Fuel Assemblies from the BN-350 Fast-Breeder Reactor in the City of*

- Aqtau, Kazakhstan.* Nuclear Instruments and Methods in Physics Research A, 2002. **490**: p. 409-425.
25. Willman, C., et al., *Nondestructive Assay of Spent Nuclear Fuel with Gamma-Ray Spectroscopy*. Annals of Nuclear Energy, 2006. **33**: p. 427-438.
 26. Mora, M.V., et al., *Nondestructive Burnup Measurements by Gamma-Ray Spectroscopy on Spent Fuel Elements of the RP-10 Research Reactor*. Progress in Nuclear Energy, 2011. **53**: p. 344-353.
 27. Turunen, J., et al., *Comprehensive Radioassays of Samples Using the PANDA Device*. Nuclear Instruments and Methods in Physics Research A, 2012. **678**: p. 78-82.
 28. Hayakawa, T., et al., *Nondestructive Assay of Plutonium and Minor Actinide in Spent Fuel Using Nuclear Resonance Fluorescence with Laser Compton Scattering γ -rays*. Nuclear Instruments and Methods in Physics Research A, 2010. **621**: p. 695-700.
 29. Shizuma, T., et al., *Statistical Uncertainties of Nondestructive Assay for Spent Nuclear Fuel by Using Nuclear Resonance Fluorescence*. Nuclear Instruments and Methods in Physics Research A, 2014. **737**: p. 170-175.
 30. Armozd, H.R., et al., *Determination of Tehran Research Reactor Power by ^{16}N Gamma Detection*. Annals of Nuclear Energy, 2011. **38**: p. 2667-2672.
 31. Jalali, M., Abdi, M.R., Mostajaboddavati, M., *Prompt Gamma Radiation as a New Tool to Measure Reactor Power*. Radiation Physics and Chemistry, 2013. **91**: p. 19-27.
 32. Jalali, M., Abdi, M.R., Mostajaboddavati, M., *Reactor Power Measurement by Gamma and Neutron Radiation in Heavy Water Zero Power Reactor (HWZPR)*. Annals of Nuclear Energy, 2013. **57**: p. 368-374.
 33. Nelson, K.A., et al., *Nuclear Reactor Pulse Calibration Using a CdZnTe Electro-Optic Radiation Detector*. Applied Radiation and Isotopes, 2012. **70**: p. 1118-1120.
 34. Bowden, N.S., et al., *Advances Towards Readily Deployable Antineutrino Detectors for Reactor Monitoring and Safeguards* in *Institute of Nuclear*

- Materials Management Annual Conference*, LLNL-CONF-404568, 2008: Nashville, Tennessee.
35. Sweeney, M., et al., *Large-Scale Gadolinium-Doped Water Cherenkov Detector for Nonproliferation*. Nuclear Instruments and Methods in Physics Research A, 2011. **654**: p. 377-382.
 36. Erickson, A.S., *Remote Detection of Fissile Material: Cherenkov Counters for Gamma Detection*. Presentation, Annual SSGF Meeting, Livermore, California, July 20-22, 2011.
 37. Erickson, A.S., *Remote Detection of Fissile Material: Cherenkov Counters for Gamma Detection*. PhD Dissertation, MIT, June 2011.
 38. Dazeley, S., Sweeney, M., Bernstein, A., *SNM Detection with an Optimized Water Cherenkov Neutron Detector*. Nuclear Instruments and Methods in Physics Research A, 2012. **693**: p. 148-153.
 39. Rippon, S.E., *Cherenkov Detectors for the Measurement of Reactor Power*. Nuclear Instruments and Methods, 1963. **21**: p. 192-196.
 40. Strindehag, O., *Cerenkov Detectors for Fission Product Monitoring in Reactor Coolant Water*. AE-294, 1967: Stockholm, Sweden.
 41. Dowdy, E.J., Nicholson, N., Caldwell, J.T., *Irradiated Fuel Monitoring by Cerenkov Glow Intensity Measurements*. LA-7838-MS. 1979: Los Alamos, New Mexico.
 42. Nicholson, N., Dowdy, E.J., *Irradiated Fuel Examination Using the Cerenkov Technique*. LA-8767-MS. 1981: Los Alamos, New Mexico.
 43. Hildingsson, L., et al., *Cerenkov Viewing Devices with Increased Sensitivity and Image Size*, in *IAEA International Nuclear Safeguards Conference*. IAEA-SM-333/6P: 1994. Vienna, Austria.
 44. Chen, J.D., et al., *Long-cooled Spent Fuel Verification Using a Digital Cerenkov Viewing Device*. IAEA-SM-367/14/07. 2001: Vienna, Austria.
 45. Chen, J.D., et al., *Development of a High Sensitivity Digital Cerenkov Viewing Device*. CSSP Report 123. 2002: Pinawa, Canada.

46. Kuribara, M., Nemoto, K., *Development of New UV-I.I. Cerenkov Viewing Device*. IEEE Transactions on Nuclear Science, 1994. **41**(1): p. 331-335.
47. Kuribara, M., *Spent Fuel Burnup Estimation by Cerenkov Glow Intensity Measurement*. IEEE Transactions on Nuclear Science, 1994. **41**(5): p. 1736-1739.
48. Chen, J.D., et al., *Cerenkov Characteristics of BWR Assemblies Using a Prototype DCVD with a Back-Illuminated CCD*. CSSP Report 2004-01-01. 2003: Pinawa, Canada.
49. Chen, J.D., et al., *Cerenkov Characteristics of PWR Assemblies Using a Prototype DCVD with a Back-Illuminated CCD*. CSSP Report 2004-01-02. 2003: Pinawa, Canada.
50. Attas, E.M., et al., *A Nuclear Fuel Verification System Using Digital Imaging of Cherenkov Light*. Nuclear Instruments and Methods in Physics Research A, 1997. **384**(2-3): p. 522-530.
51. Chen, J.D., *Field Test of a DCVD Using an Ixon Camera with a Lumogen-Coated EMCCD Detector*. CSSP Report 2004-01-03. 2003: Pinawa, Canada.
52. Chen, J.D., et al., *Partial Defect Detection Using a Digital Cerenkov Viewing Device and Image Processing*, in *Symposium on International Safeguards Addressing Verification Challenges*. IAEA-CN-148/69. 2006: Vienna, Austria.
53. Lindberg, B., et al., *Modelling of Cerenkov Light Emission from Spent BWR Nuclear Fuel with Missing or Substituted Rods*, in *Symposium on International Safeguards Addressing Verification Challenges*. IAEA-CN-148/70. 2006: Vienna, Austria.
54. Grape, S., Svaerd, S.J., Lindberg, B., *Verifying Nuclear Fuel Assemblies in Wet Storages on a Partial Defect Level: A Software Simulation Tool for Evaluating the Capabilities of the Digital Cherenkov Viewing Device*. Nuclear Instruments and Methods in Physics Research A, 2013. **698**: p. 66-71.
55. Chen, J.D., Parcey, D.A., Kosierb, R., *Detection of Partial Defects using a Digital Cerenkov Viewing Device*. IAEA-CN-184/338. 2009: Vienna, Austria.

56. Rossa, R., Peerani, P., *Development of a Model for the Approximation of the Neutron and Photon Flux in a BWR Spent Fuel Assembly*. Annals of Nuclear Energy, 2013. **57**: p. 256-262.
57. Arkani, M., Gharib, M., *Residual Heat Estimation by Image Processing Using Cherenkov Radiation in TRR*, in *Research Reactor Fuel Management Conference*. 2007: Lyons, France.
58. Arkani, M., Gharib, M., *Residual Heat Estimation by Using Cherenkov Radiation in Tehran Research Reactor*. Nuclear Instruments and Methods in Physics Research A, 2008. **596**: p. 417-421.
59. Arkani, M., Gharib, M., *Further Comments on Residual Heat Estimation by Using Cherenkov Radiation in Tehran Research Reactor*. Nuclear Instruments and Methods in Physics Research A, 2010. **624**: p. 241.
60. Orndoff, J., *Prompt Neutron Periods of Metal Critical Assemblies*. Nuclear Science and Engineering, 1957. **2**: p. 450-460.
61. Hansen, G.E., *The Rossi Alpha Method*. LA-UR-85-4176, 1985. Los Alamos, New Mexico.
62. Pazsit, I., Demaziere, C., *Noise Techniques in Nuclear Systems, Chapter 14, Handbook of Nuclear Engineering*. 2010. New York: Springer, LLC.
63. Baker, B., *Reactor Parameters for the ISU-AGN-201 Reactor*. 2011, Idaho State University. Thesis.
64. Uhrig, R., *Noise Analysis in Nuclear Systems*. 1964. Washington, D.C.: U.S. Atomic Energy Commission.
65. Degweker, S.B., Rudra, R., *On the relation between Rossi alpha and Feynman alpha methods*. Annals of Nuclear Energy, 2016. **94**: p. 433-439.
66. Croft, S., Favalli, A., Hauck, D.K., Henzlova, D., Santi, P.A., *Feynman variance-to-mean in the context of passive neutron coincidence counting*. Nuclear Instruments and Methods in Physics Research A, 2012. **686**: p. 136-144.
67. Spriggs, G.D., *Two Rossi- α Techniques for Measuring the Effective Delayed Neutron Fraction*. Nuclear Science and Engineering, 1993. **113**: p. 161-172.

68. *MCNP – A General Monte Carlo N-Particle Transport Code, Version 5*, LA-UR-03-1987, April 2003.
69. Leppanen, J., Aufiero, M., Fridman, E., Rachamin, R., van der Marck, S., *Calculation of Effective Point Kinetics Parameters in the Serpent 2 Monte Carlo Code*. Annals of Nuclear Energy, 2014. **65**: p. 272-279.
70. Abou-El-Maaty, T., Abdelhady, A., *Reactor Thermal Behaviors under Kinetics Parameters Variations in Fast Reactivity Insertion*. Annals of Nuclear Energy, 2009. **36**: p. 240-245.
71. Spriggs, G.D., *A Measurement of the Effective Delayed Neutron Fraction of the Westinghouse Idaho Nuclear Company Slab Tank Assembly Using Rossi- α Techniques*. Nuclear Science and Engineering, 1993. **115**: p. 76-80.
72. Por, G., Szappanos, G., Binh, D.Q., *Feynman-Alpha Measurement in a 100 kW Research Reactor*. Progress in Nuclear Energy, 1998. **33**: p. 439-455.
73. Spriggs, G.D., Sakurai, T., Okajima, S., *Rossi- α and β_{eff} Measurements in a Fast Critical Assembly*. Progress in Nuclear Energy, 1999. **35**: p. 169-181.
74. Kuramoto, R.Y.R., dos Santos, A., Jerez, R., Diniz, R., *Absolute Measurement of β_{eff} Based on Feynman- α Experiments and the Two-Region Model in the IPEN/MB-01 Research Reactor*. Annals of Nuclear Energy. **34**(6): p. 433-442.
75. Pepyolyshev, Y.N., *Method of Experimental Estimation of the Effective Delayed Neutron Fraction and of the Neutron Generation Lifetime in the IBR-2 Pulsed Reactor*. Annals of Nuclear Energy, 2008. **35**: p. 1301-1305.
76. Muhammad, A., Iqbal, M., Mahmood, T., Qadir, J., *Calculation and Measurement of Kinetic Parameters of Pakistan Research Reactor-1 (PARR-1)*. Annals of Nuclear Energy, 2011. **38**: p. 44-48.
77. Hosseini, S.A., Vosoughi, N., *Uncertainty Evaluation of Calculated and Measured Kinetics Parameters of Tehran Research Reactor*. Nuclear Engineering and Design, 2010. **240**: p. 2761-2767.
78. Bretscher, M., *Evaluation of Reactor Kinetic Parameters without the Need for Perturbation Codes*. In *1997 International Meeting on Reduced Enrichment for Research and Test Reactors*. 1997: Jackson Hole, Wyoming.

79. Zaker, M., *Effective Delayed Neutron Fraction and Prompt Neutron Lifetime of Tehran Research Reactor*. Annals of Nuclear Energy, 2003. **30**: p. 1591-1596.
80. Jonah, S.A., Liaw, J.R., Matos, J.E., *Monte Carlo Simulation of Core Physics Parameters of the Nigeria Research Reactor-1 (NIRR-1)*. Annals of Nuclear Energy, 2007. **34**: p. 953-957.
81. Iqbal, M., Tayyab, M., Pervez, S., *Flow of Kinetics Parameters in a Typical Swimming Pool Type Research Reactor*. Annals of Nuclear Energy, 2008. **35**: p. 518-524.
82. Hosseini, S.A., et al., *Calculation, Measurement, and Sensitivity Analysis of Kinetics Parameters of Tehran Research Reactor*. Annals of Nuclear Energy, 2010. **37**: p. 463-470.
83. Hosseini, S.A., et al., *Monte Carlo Simulation of Feynman- α and Rossi- α Techniques for Calculation of Kinetics Parameters of Tehran Research Reactor*, Annals of Nuclear Energy, 2011. **38**: p. 2140-2145.
84. Abtin, F., Feghhi, S.A.H., Jafarikia, S., *Neutronic Evaluations for MNSR Research Reactor Core Conversion from HEU to LEU*. Annals of Nuclear Energy, 2013. **51**: p. 69-73.
85. Khan, M.J.H, Sarker, M.M., Islam, S.M.A., *Analysis of kinetics parameters of 3 MW TRIGA Mark-II research reactor using the SRAC2006 code system*. Annals of Nuclear Energy, 2013. **60**: p. 181-186.
86. Yamamoto, T., Sakamoto, H., *A New Concept of Monte Carlo Kinetics Parameter Calculation Using Complex-valued Perturbation*. Annals of Nuclear Energy, 2014. **71**: p. 480-488.
87. Jelley, J.V., *Cerenkov Radiation and Its Applications*. 1958, London, UK: Pergamon Press.
88. Collins, G.B., Reiling, V.G., *Cerenkov Radiation*. Physical Review, 1938. **54**: p. 499-503.
89. Cerenkov, P.A., *Radiation of Particles Moving at a Velocity Exceeding that of Light, and Some of the Possibilities for Their Use in Experimental Physics*. Nobel Lecture, 1958.

90. Tamm, I.E., *General Characteristics of Radiations Emitted by Systems Moving with Super-light velocities with Some Applications to Plasma Physics*. Nobel Lecture, 1958.
91. Ilver, L., *Technical Report on Cherenkov light measurements at CLAB*, Chalmers University of Technology, Gothenburg, Sweden. November 1993.
92. Durkee, Jr., J.W., James, M.R., *MCNP6 Cerenkov Radiation Feature Verification*. LA-UR-13-25416. 2013: Los Alamos, New Mexico.
93. James, M.R., *Implementation of Cerenkov Radiation and Reflection/Refraction into MCNP6*. LA-UR-13-25911. 2013: Los Alamos, New Mexico.
94. Pelowitz, D.B., et al., *MCNP6 User's Manual, Version 1.0*. LA-CP-13-00634. 2013: Los Alamos, New Mexico.
95. Pelowitz, D.B., et al., *MCNP6 User's Manual, Code Version 6.1.1beta, Rev. 0*. LA-CP-14-00745. June 2014: Los Alamos, New Mexico.
96. Johnson, M., Lucas, S., Tsvetkov, P., *Modeling of Reactor Kinetics and Dynamics*. INL/EXT-10-19953. 2010: Idaho Falls, Idaho.
97. Lamarsh, J.R., *Nuclear Reactor Theory*. 1966, Boston: Addison-Wesley Publishing.
98. Hetrick, D., *Dynamics of Nuclear Reactors*, University of Chicago Press, 1971.
99. Muhammad, A., Iqbal, M., Mahmood, T., *Burn-up effect on inherent safety parameters and reactivity insertion transient analysis of Pakistan Research Reactor-1*, Progress in Nuclear Energy, 2012, **58**: p. 1-5.
100. Pavlovitchev, A.M., Gorokhov, A.A., Ivanov, V.K., Styrin, Y.A., *Kinetics Parameters of VVER-1000 Core with 3 MOX Lead Test Assemblies To Be Used for Accident Analysis Codes*, ORNL-SUB-99-B99398V-2, 1999.
101. Gehin, J.C., Carbojo, J.J., Ellis, R.J., *Issues in the Use of Weapons-Grade MOX Fuel in VVER-1000 Nuclear Reactors: Comparison of UO₂ and MOX Fuels*, ORNL-TM-2004-223, 2004.
102. Hassan, M., *A Comparative Study on the Safety and Kinetics Parameters of UO₂ and MOX Fuel*, Arab Journal of Nuclear Science and Applications, **49**(1): p. 53-60, 2016.

103. Hartman, M.R., Keller, S.T., Reese, S.R., Robinsion, B., Stevens, J., Matos, J.E., Marcum, W.R., Palmer, T.S., Woods, B.G., *Neutronic Analysis of the Oregon State TRIGA Reactor in Support of Conversion from HEU Fuel to LEU Fuel*, Nuclear Science and Engineering, 2013, 174: p, 135-149.
104. Massih, A.R., *Models for MOX Fuel Behavior – A selective review*. SKI Report 2006:10, January 2006.
105. Marcum, W.R., et al., *A Comparison of Pulsing Characteristics of the Oregon State University TRIGA Reactor with FLIP and LEU Fuel*. Nuclear Science and Engineering, 2012. **171**: p. 150-164.
106. *Safety Analysis Report for the Conversion of the Oregon State University TRIGA Reactor from HEU to LEU Fuel*, Oregon State University TRIGA Reactor License No. R-106, Docket No. 50-243. November 2007.
107. Chen, W.Z., Kuang, B., Guo, L.F., Chen, Z.Y., Zhu, B., *New Analysis of Prompt Supercritical Process With Temperature Feedback*. Nuclear Engineering and Design, 2006. **236**: p. 1326-1329.
108. Scalettar, R., *The Fuchs-Nordheim Model with Variable Heat Capacity*, Nuclear Science and Engineering, 1963. **16**: p. 459
109. Wolfe, B., *The Nordheim-Fuchs Excursion Model with Non-linear Reactivity Feedback*, Nuclear Science and Engineering, 1964. **20**: p. 238-240.
110. Lewins, J.D., *The Adiabatic Fuchs-Nordheim Model and Non-dimensional Solutions*, Annals of Nuclear Energy, 1995, **22**(10): p. 681-686.
111. Van Dam, H., *Improved One-delayed Group Neutron Kinetics Model for Small Reactivity States*, Annals of Nuclear Energy, 1997, **24**(7): p. 571-573.
112. Oregon State University Radiation Center, *Oregon State TRIGA Reactor Training Manual*, 2014.
113. *Kinetic Behavior of TRIGA Reactors*. GA-7882. 1967.
114. Figliola, R.S., Beasley, D.E., *Theory and Design for Mechanical Measurements*, 5th Ed., John Wiley & Sons, Inc., 2011.
115. *PDA25K- GaP Switchable Gain Detector User Guide, Revision E*. Thorlabs, Inc. June 2015.

116. *Si Photodiodes, Chapter 2.* Hamamatsu, Inc. Web. June 2015.
117. *Multimode Round Fiber Optic Bundle Cables: SMA to SMA.* Thorlabs, Inc. Web. June 2015.
118. Paxton, F., *Solid Angle Calculation for a Circular Disk,* The Review of Scientific Instruments, 1959, **30**(4): p. 254-258.
119. *Air-Spaced Doublet Collimators – FC/PC, FC/APC, & SMA.* Thorlabs, Inc. Web. June 2015.
120. *COL-UV-30 Collimating Lens.* Ocean Optics, Inc. Web. June 2015.
121. *Suprasil 1, 2, 3 and Suprasil Standard.* Heraeus, Inc. POL-O/422M-E, March 1998.
122. *Device Specifications – NI PXIe-5171R,* National Instruments, January 2015.
123. *PXIe Express – NI PXIe-1085 Series User Manual,* National Instruments, January 2017.
124. *Fiber-Coupled LEDs,* Thorlabs, Inc. Web. June 2015.
125. *NI SC Express – NI PXIe-4322 User Manual,* National Instruments, April 2013.
126. Butterworth, S., *On the Theory of Filter Amplifiers,* Experimental Wireless and the Wireless Engineer, 1930: p. 536-541.

10 NOMENCLATURE

Symbols

c	Speed of light
f_{BW}	Frequency bandwidth
l	Prompt neutron lifetime
n	Index of refraction
t	Time
t_r	Cutoff frequency
s_2	Inverse transient period
v	Neutron velocity
\$	Reactivity in dollars
B	Delayed neutron emission source operator
C_i	Precursor concentration for each delayed neutron group
C_p	Total Heat Capacity
D	First derivative
F	Fission operator
I	Integral
N	Number of points in integration
N_q	Concentration of isotope in fuel mixture
N_X	Fraction adjustment in \$ reactivity insertion for X_{th} pulse
P	Reactor power
P_{max}	Maximum reactor power
S	External neutron source strength
T	Temperature
T_e	Kinetic energy
X	Deviation in β/l ratio
α	Prompt neutron decay constant, Temperature coefficient of reactivity

β	Delayed neutron fraction
β_{eff}	Effective delayed neutron fraction
β^i	Delayed neutron fraction for each precursor group, i
Δt	Time step
ϵ	Relative speed of light in a vacuum
θ	Characteristic angle
λ	Neutron precursor decay constant
$v\Sigma_f$	Total fission neutron production cross section
$v_{dj}\Sigma_f$	Delayed fission neutron production cross section
ρ	Reactivity
σ_f	Microscopic fission cross section
σ	Associated parameter uncertainty
χ	Total fission spectrum
χ_{dj}	Delayed neutron emission spectrum
ψ	Angular flux
ψ^+	Adjoint angular flux
ω	Transient reactor period
Λ	Mean neutron generation time
Ω	Solid angle

Acronyms

BOL	Beginning of Life
CCD	Charge-coupled Device
CdZnTe	Cadmium Zinc Tellerium
CRANK	Cherenkov Radiation Assay for Nuclear Kinetics
CVD	Cherenkov Viewing Device
DA	Destructive Assay
DAS	Data Acquisition System
DCVD	Digital Cherenkov Viewing Device

DDA	Differential Die-Away
DDSI	Differential Die-away Self-Interrogation
EOL	End of Life
FN	Fuchs-Nordheim
FWHM	Full-Width Half Maximum
FSAR	Final Safety Analysis Report
GR-S	Gamma-Ray Spectroscopy
HWZPR	Heavy Water Zero Power Reactor
IAEA	International Atomic Energy Agency
IC	Ion Chamber
INFCIRC	Information Circular
LED	Light Emitting Diode
LEU	Low Enriched Uranium
MCNP	Monte Carlo N-Particle
MOL	Middle of Life
MOX	Mixed-Oxide Fuel
N	Nitrogen
NDA	Nondestructive Assay
NGSI	Next Generation Safeguards Initiative
NI	National Instruments
NPT	Nuclear Nonproliferation Treaty
NRF	Nuclear Resonance Fluorescence
O	Oxygen
OSTR	Oregon State TRIGA Reactor
P-X	X _{th} OSTR Experimental Pulse
PD	Photodiode
PJ	Prompt Jump
PMT	Photomultiplier Tube
PNCC	Passive Neutron Coincidence Counting
PRKE	Point Reactor Kinetics Equation

Pu	Plutonium
PXIe	Peripheral Component Interconnect eXtensions for Instrumentation Express
RMS	Root Mean Square
S/N	Signal-to-Noise
SFCC	Spent Fuel Coincidence Counter
SQ-X	X _{th} OSTR Experimental Square Wave
TRIGA	Training, Research, and Isotope – General Atomics
TRR	Tehran Research Reactor
U	Uranium
UQ	Uncertainty Quantification
UV	Ultraviolet
VI	Virtual Instrument
XR-S	X-Ray Spectroscopy

11 APPENDIX A – PD EVALUATION

During the initial evaluation of the photodiodes during development of the CRANK system, it was necessary to evaluate the Thorlabs PDA25K response to the Thorlabs M365FP1 LED light source in a controlled, laboratory environment. Figure 11-1 and Figure 11-2 present the absolute PD response and the S/N ratio as a function of varying LED supply current at different amplifications available for the Thorlabs PDA25K photodiode. Figure 11-3 presents the PD response with respect to LED optical power output by the Thorlabs M365FP1 LED light source using the LED output as a function of supplied current from Figure 5-2.

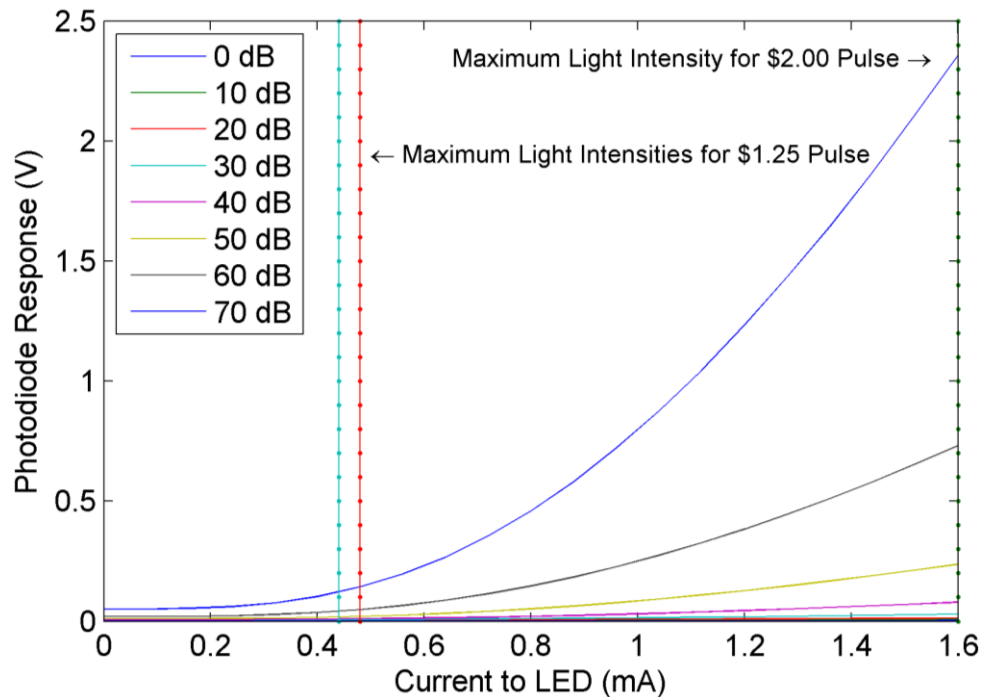


Figure 11-1. Calibration curve for TRIGA-like light intensities

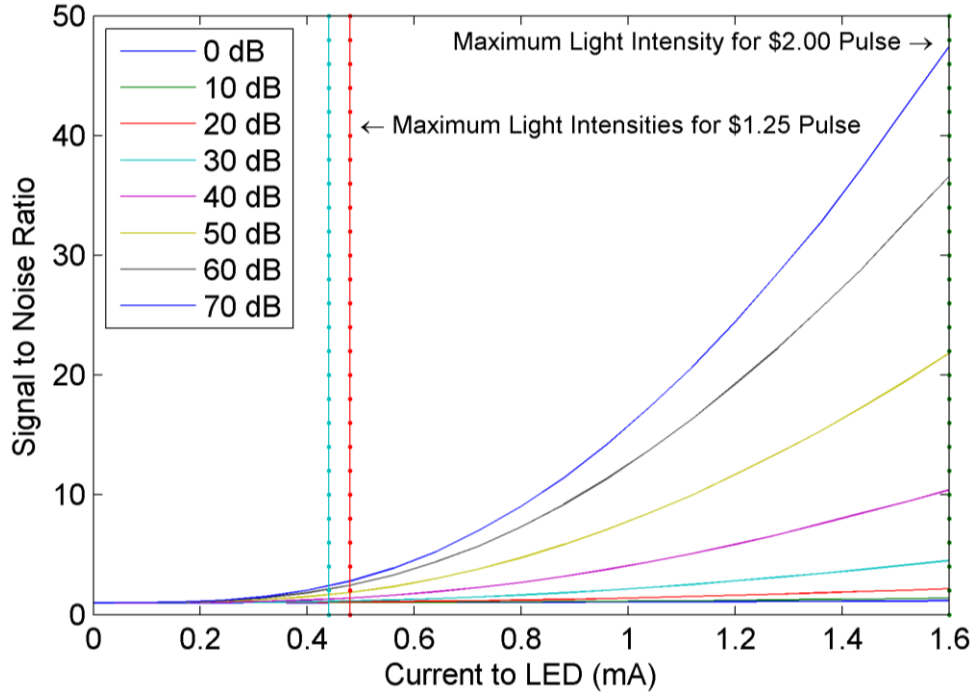


Figure 11-2. Signal to Noise curve for TRIGA-like light intensities

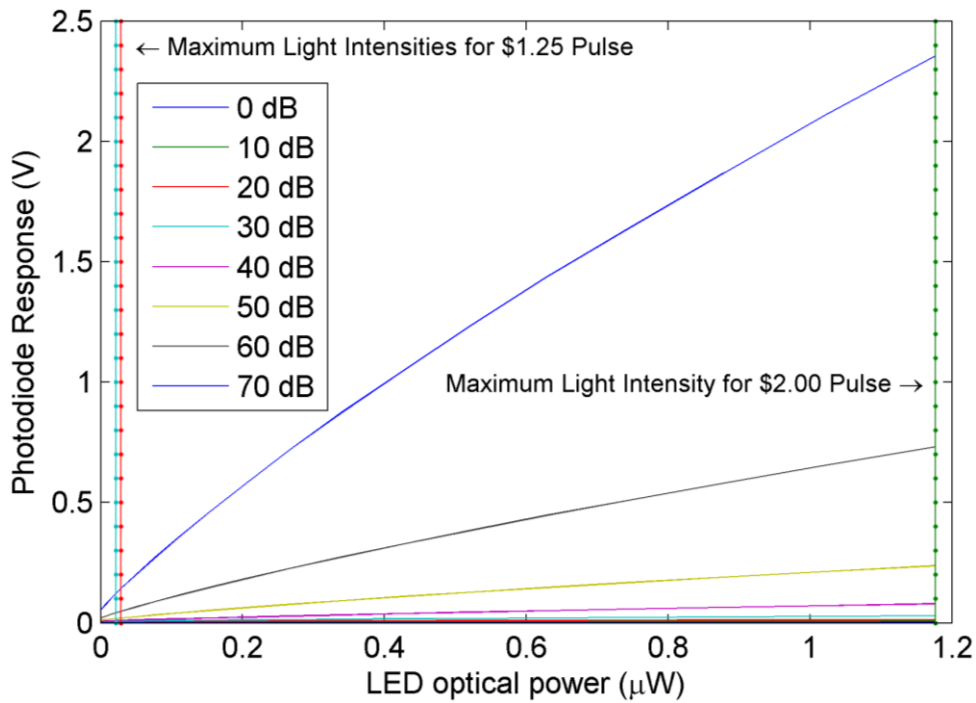


Figure 11-3. PD response curve with varying LED optical power

Figure 11-4 through Figure 11-10 provide the PD response as a function of LED supplied current with associated uncertainty for each specified PD amplification. As can be observed, the S/N ratio decreases with increased amplification. For OSTR experiments, therefore, it is better to increase the S/N ratio by increasing the amplification gain setting on the Thorlabs PDA25K photodiode.

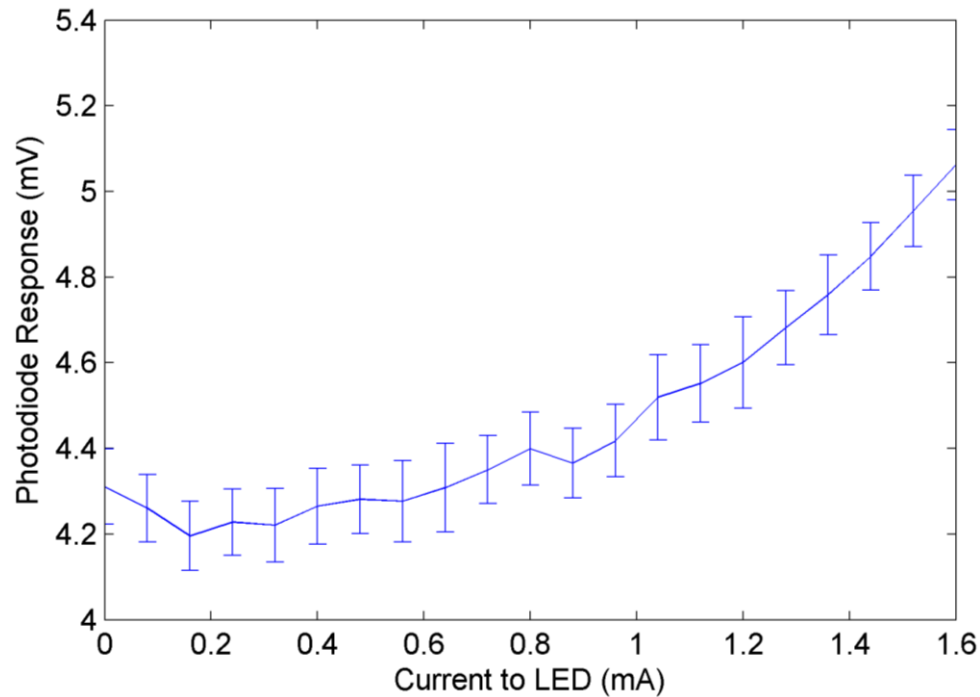


Figure 11-4. PD response as a function of LED supplied current – 0 dB

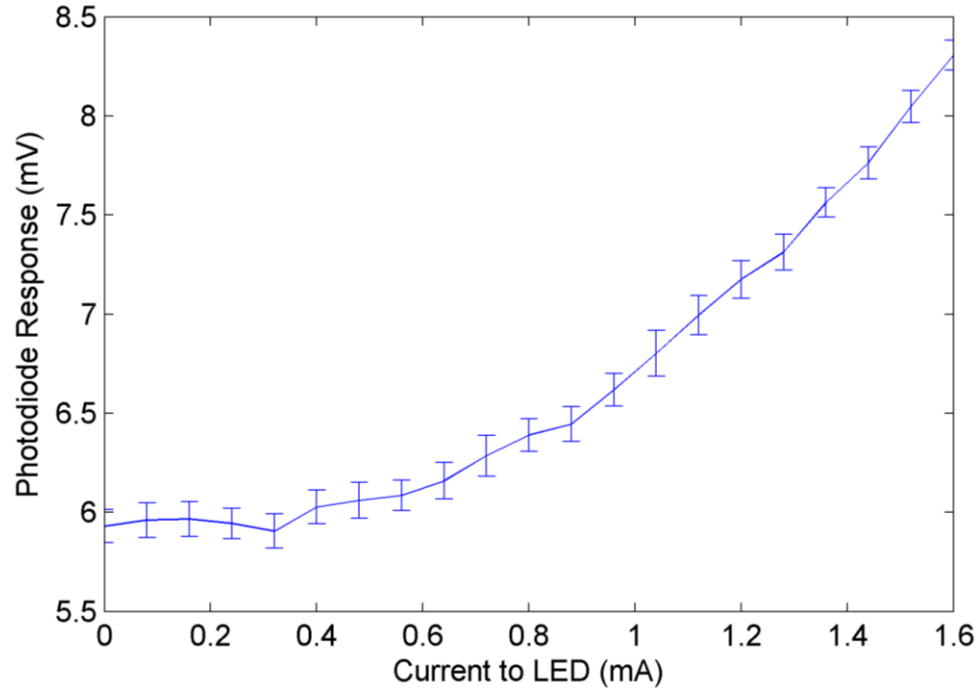


Figure 11-5. PD response as a function of LED supplied current – 10 dB

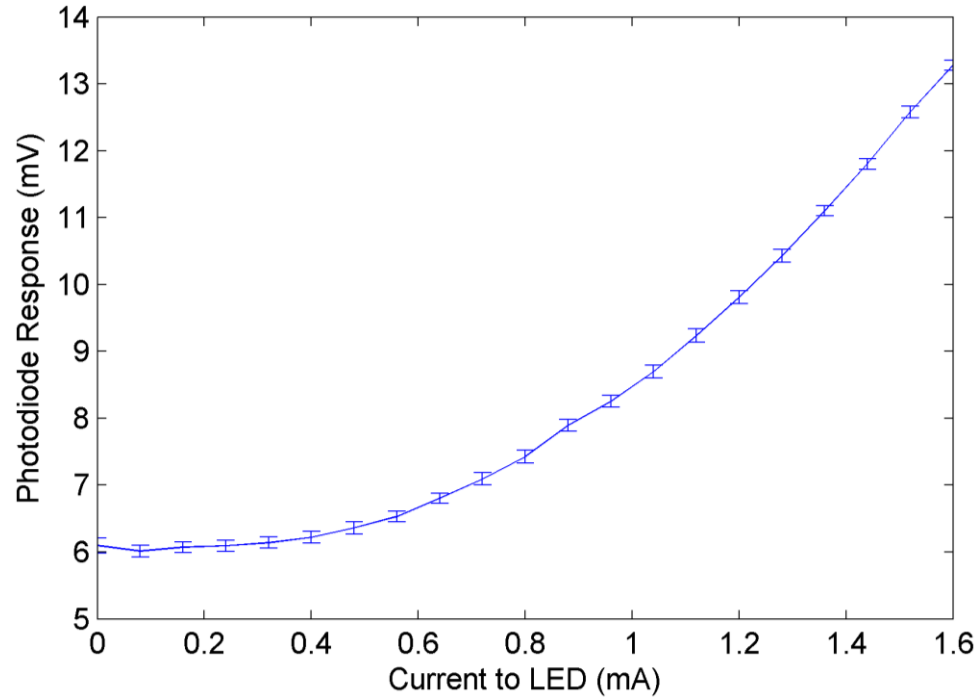


Figure 11-6. PD response as a function of LED supplied current – 20 dB

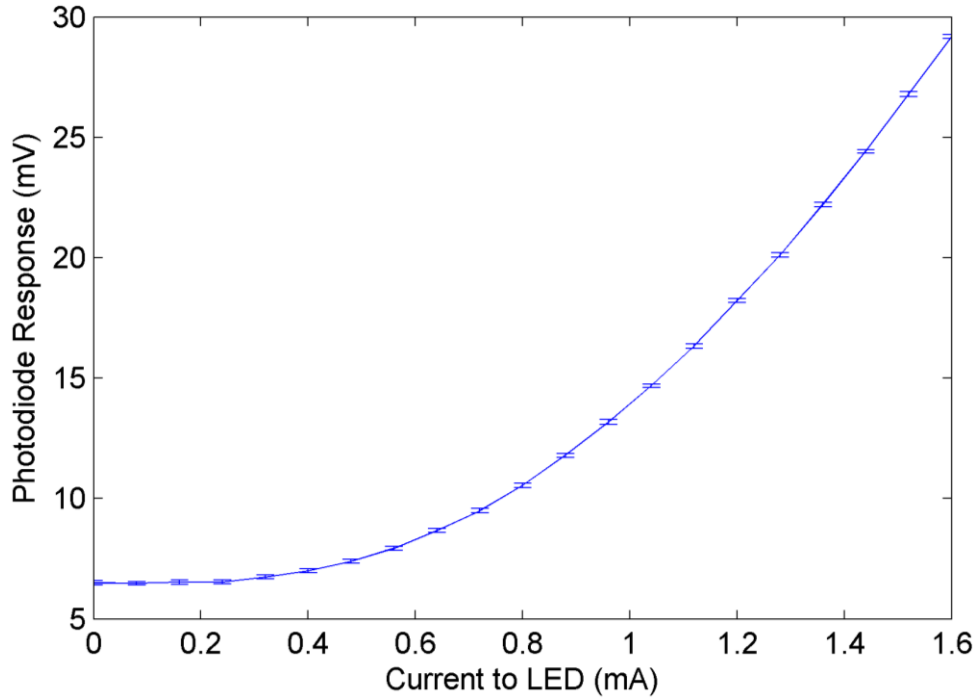


Figure 11-7. PD response as a function of LED supplied current – 30 dB

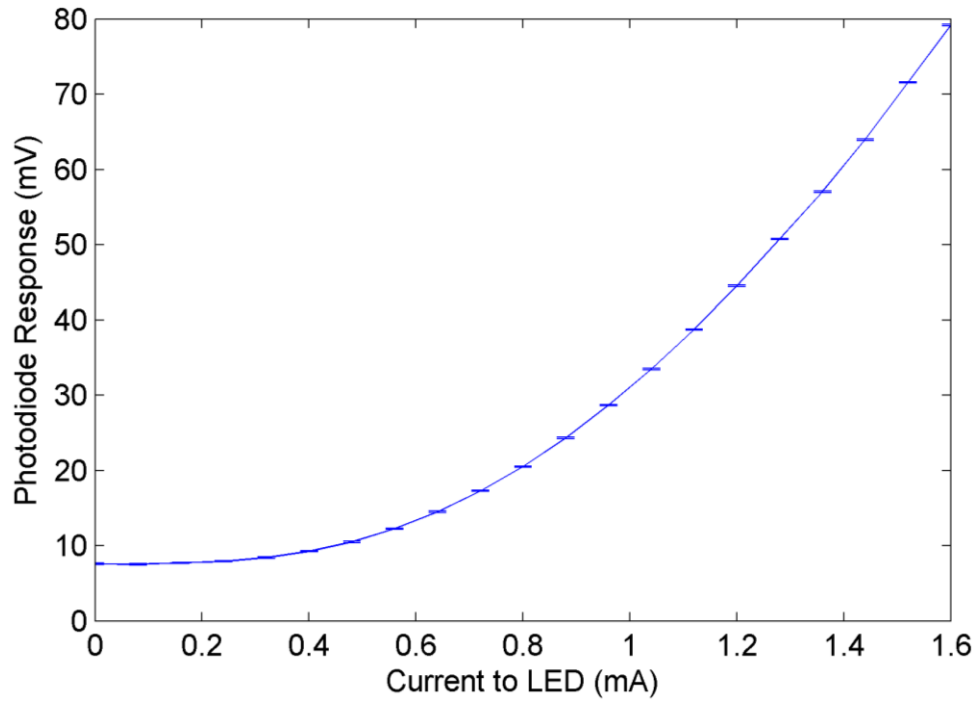


Figure 11-8. PD response as a function of LED supplied current – 40 dB

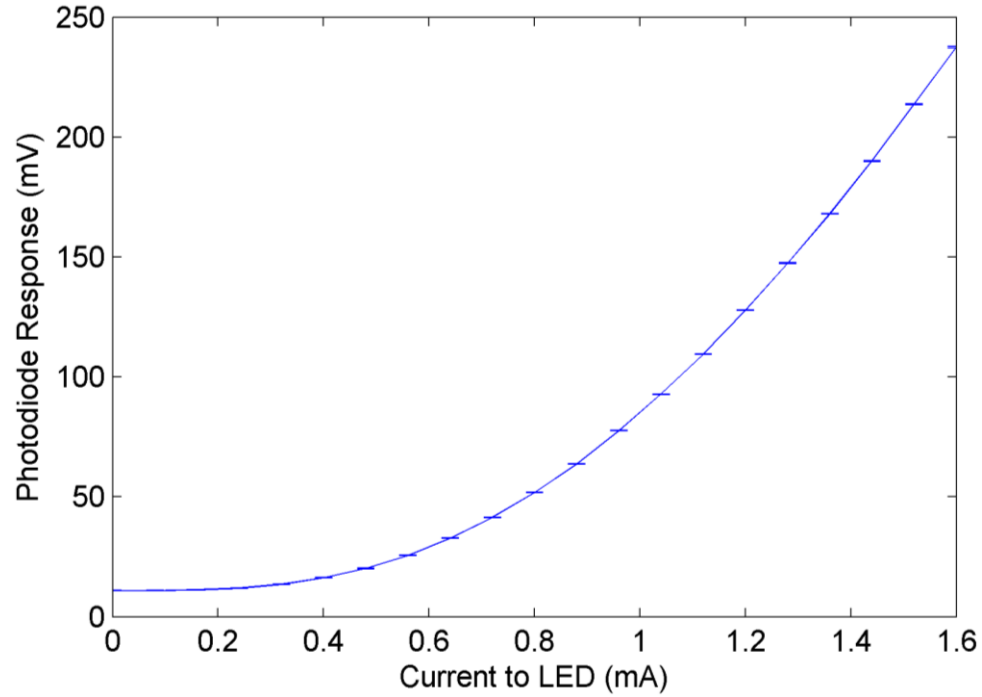


Figure 11-9. PD response as a function of LED supplied current – 50 dB

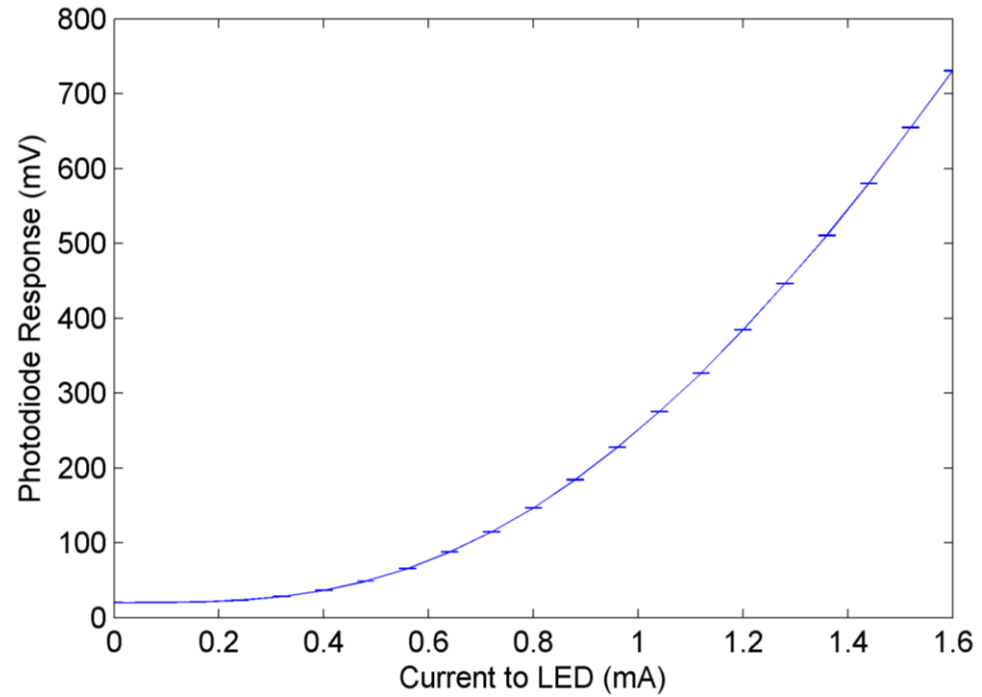


Figure 11-10. PD response as a function of LED supplied current – 60 dB

Figure 11-11 through Figure 11-14 provide similar curves to Figure 6-5 for additional isolated rows and columns to exhibit the behavior of the PD response with increased distance from the LED light source. As can be observed in Figure 11-11 through Figure 11-14, the uncertainty bars are relatively small in comparison to the normalized scale in the figures.

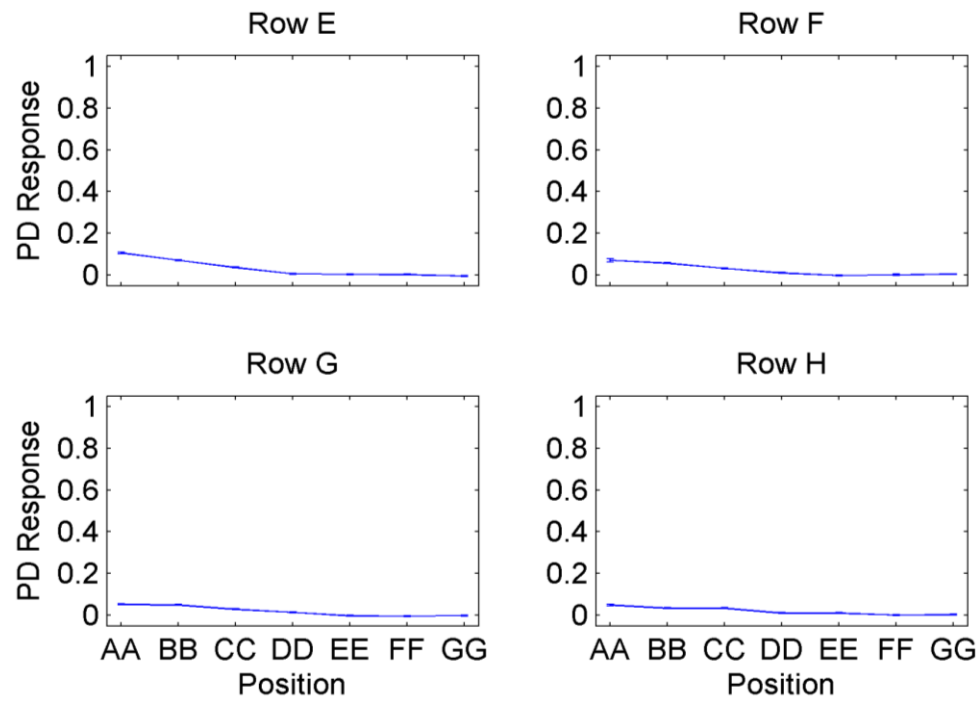


Figure 11-11. Normalized PD response with associated uncertainty (E-H)

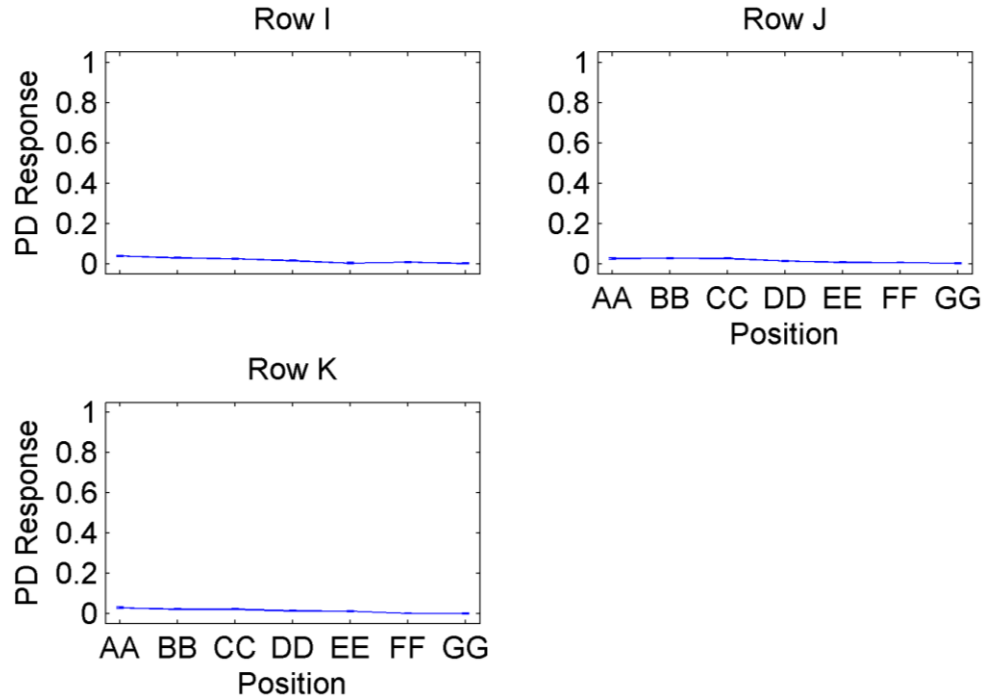


Figure 11-12. Normalized PD response with associated uncertainty (I-K)

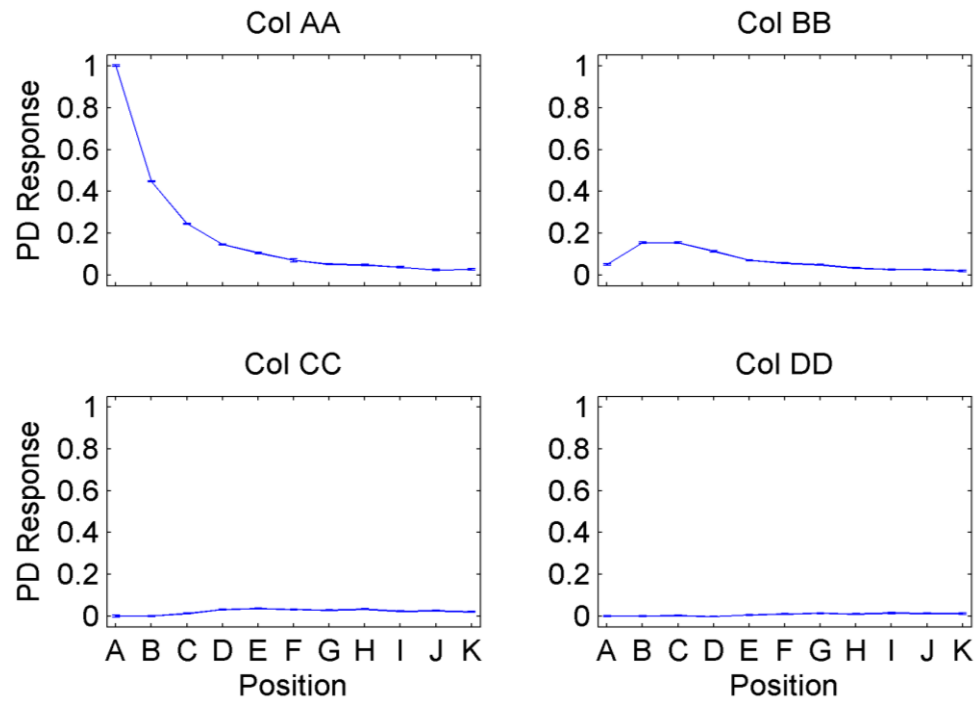


Figure 11-13. Normalized PD response with associated uncertainty (AA-DD)

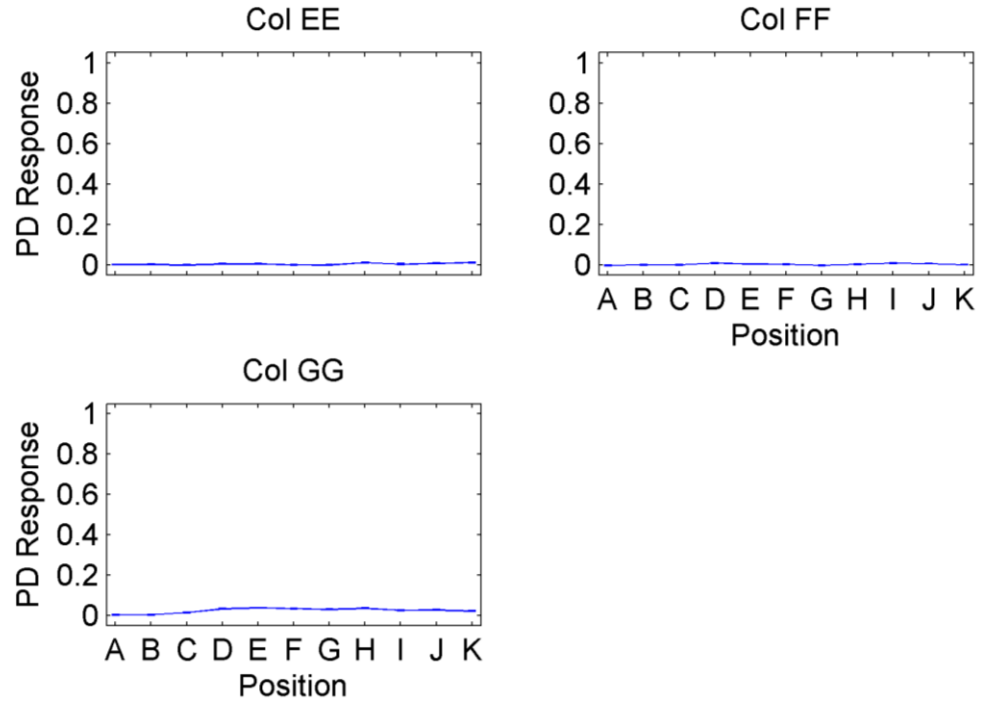


Figure 11-14. Normalized PD response with associated uncertainty (EE-GG)

12 APPENDIX B – COMPLETE ASSESSMENT OF OSTR TRANSIENTS

In Section 6.2, OSTR experimental data were used to calculate the β/l ratio for the OSTR and was compared to the declared reactor kinetics parameter ratio in the OSTR FSAR. However, these results constituted tests that provided enough information to be analyzed with theoretical kinetics relationships. In the initial testing phases of the CRANK system, many tests were performed that did not yield data with an S/N ratio and sample rate that were readily analyzed with the CRANK methodology.

For square waves, the S/N ratio was significantly reduced due to the lack of Cherenkov light at low power levels.

For reactor pulses, experimental data at OSTR were discarded for lack of necessary sample rate for integration due to errors in NI LabVIEW VI development or implementation. Prior to October 2016, the NI PXIe-5171R digital oscilloscope was not utilized to its maximum sample rate of 250 MHz; errors in VI development resulted in a limited sample rate to approximately 375 Hz.

12.2 Square Waves

The initial testing phase for the demonstration of the CRANK system involved reactivity perturbations less than \$1.00, or square waves. The list of square waves (SQ) performed are found in Table B-1.

Table B-1. Record of square waves performed at OSTR

Test Number	Date	Reactivity	Amplification (dB)	Initial Test Power
SQ-1	Jan. 27, 2016	\$0.50	0	15 W
SQ-2	Jan. 27, 2016	\$0.80	0	15 W
SQ-3	Feb. 3, 2016	\$0.50	0	1 kW
SQ-4	Feb. 3, 2016	\$0.80	0	1 kW
SQ-5	Feb. 10, 2016	\$0.50	30	1 kW
SQ-6	Feb. 10, 2016	\$0.80	30	1 kW
SQ-7	Feb. 10, 2016	\$0.80	40	1 kW
SQ-8	March 23, 2016	\$0.50	50	1 kW
SQ-9	March 23, 2016	\$0.80	50	1 kW
SQ-10	May 25, 2016	\$0.80	70	1 kW
SQ-11	July 7, 2016	\$0.80	70	1 kW

Additionally, on 20 September 2016, a staggered increase in reactor power was performed, with the reactor operators maintaining reactor power at a steady state for one minute before increasing the power again. Due to the lack of experimental results attained for analysis during square waves, it was hypothesized that square waves might not provide enough light to be effectively measured, but the threshold for light detection was necessary to ascertain to formally cease efforts with square wave operations. It was found that the threshold occurred at approximately 500 kW, well above the prompt jump in reactor power that occurs following a square wave, though the steady rise in power above the prompt jump was observed in SQ-10 and SQ-11 measurements in Figure 12-5. Recall from Figure 6-10 that SQ-10 measurements were depicted with a filtered signal to assess the limitations of OSTR transient analysis with the PJ approximation. Figure 12-1 through Figure 12-5 provide the measurements for all the square waves provided in Table B-1. It can be observed that there is no discernible “prompt jump” behavior predicted by the prompt jump approximation, theoretically shown previously in Figure 3-6.

It should also be noted that on February 3, 2016 (SQ-3 and SQ-4 in Figure 12-2), the optical lens cap was not removed prior to testing and prevented Cherenkov light photons from interacting in the Thorlabs PDA25K photodiode. It is relevant to observe the similarities between the majority of SQ tests and the SQ-3, SQ-4 test data. During a square wave transient in OSTR, the Cherenkov light intensity is not large enough to elicit a response in the PD beyond that of background noise in the PD, exhibited by SQ-3 and SQ-4.

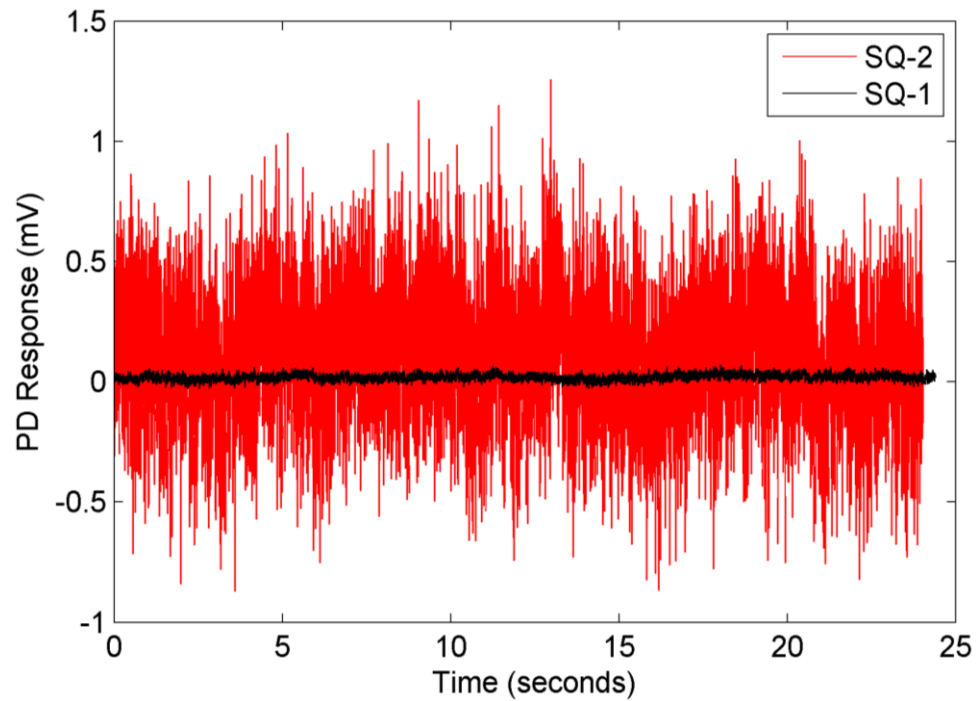


Figure 12-1. Comparison of SQ-1 and SQ-2 measurements

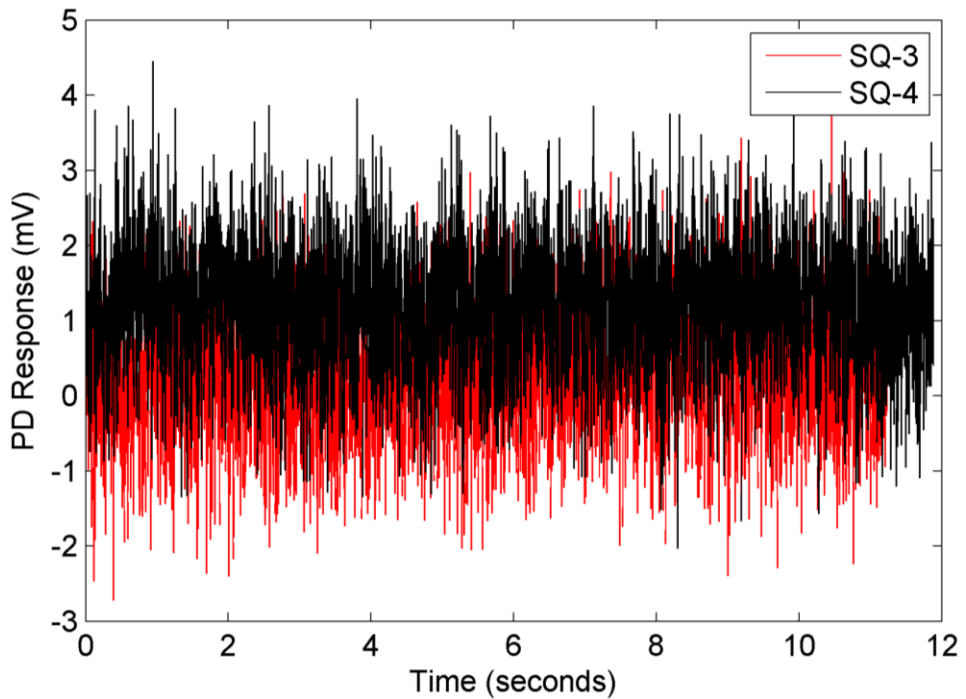


Figure 12-2. Comparison of SQ-3 and SQ-4 measurements

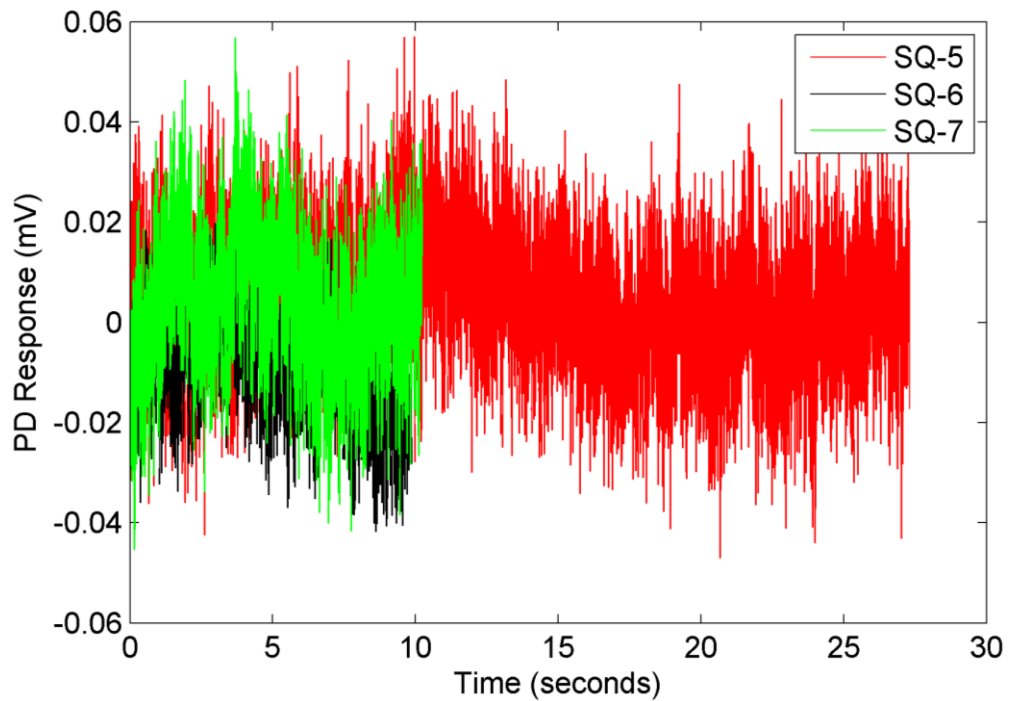


Figure 12-3. Comparison of SQ-5, SQ-6, and SQ-7 measurements

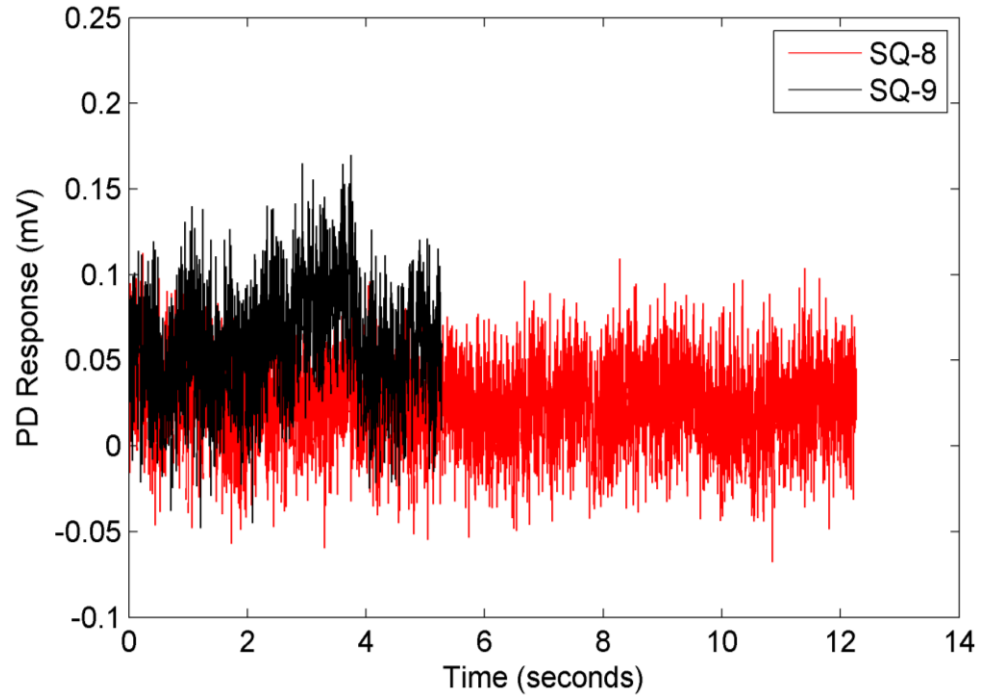


Figure 12-4. Comparison of SQ-8 and SQ-9 measurements

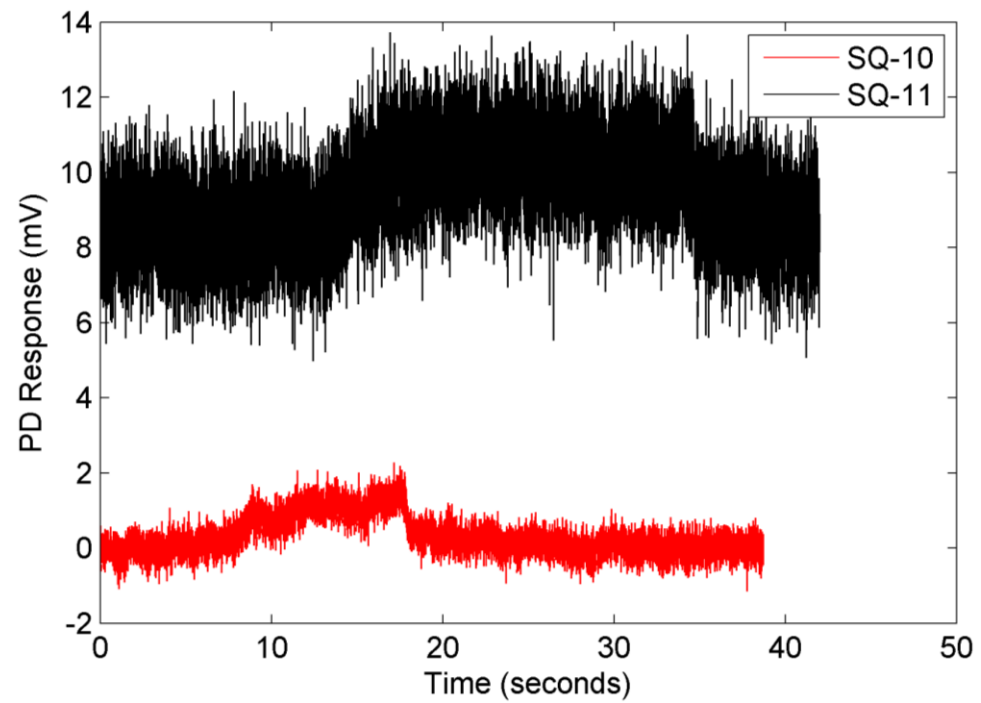


Figure 12-5. Comparison of SQ-10 and SQ-11 measurements

12.3 Reactor pulses

The second type of transient investigations for the demonstration of the CRANK system involved reactivity perturbations greater than \$1.00, or reactor pulses. The list of reactor pulses (P) performed but not included in the OSTR transient analyses from Table 6-4 in Section 6.2.2 is found in Table B-2.

Table B-2. Record of reactor pulses without sufficient data for analysis

Test Number	Date	Reactivity	Amplification (dB)	Initial Test Power
P-1	Feb. 3, 2016	\$1.25	0	15 W
P-2	Feb. 3, 2016	\$2.00	0	15 W
P-3	Feb. 10, 2016	\$1.25	40	15 W
P-4	Feb. 10, 2016	\$2.00	40	15 W
P-5	March 23, 2016	\$1.25	50	15 W
P-6	May 25, 2016	\$1.25	70	15 W
P-7	July 7, 2016	\$1.05	70	15 W
P-8	Sept. 20, 2016	\$1.25	70	15 W
P-9	Sept. 20, 2016	\$1.25	70	15 W
P-10	Sept. 20, 2016	\$2.00	70	15 W
P-11	Oct. 19, 2016	\$1.25	70	15 W
P-12	Oct. 19, 2016	\$1.75	70	15 W
P-13	Oct. 19, 2016	\$2.00	70	15 W
P-14	Dec. 12, 2016	\$1.75	70	15 W
P-15	Dec. 12, 2016	\$1.85	70	15 W
P-16	Dec. 12, 2016	\$1.95	70	15 W
P-17	Dec. 12, 2016	\$2.00	70	15 W
P-21	Jan. 30, 2017	\$1.75	70	15 W

Recall from Section 12.2 that on February 3, 2016 (P-1 and P-2), the optical lens cap was not removed prior to testing and prevented Cherenkov light photons from

interacting in the Thorlabs PDA25K photodiode, resulting in the lack of a distinct reactor pulse peak in Figure 12-6.

In Section 4, it was noted that several instrumentation changes were made over the OSTR testing campaign with the CRANK system. Following the tests on February 2016 (P-4), it was postulated that the intensity of light reaching the fiber bundle was not sufficient to create a large signal to noise ratio. Therefore, a 4 meter fiber bundle was purchased from Thorlabs to replace the original 1 meter fiber bundle. The composition of each fiber bundle was identical, and the 4 meter fiber bundle was used on every test following P-4. With a 4 meter fiber bundle, the fiber bundle was suspended in the water approximately 6 feet above the core.

Furthermore, to collect additional photons, a Thorlabs F810SMA-543 doublet collimator was used to increase the solid angle of light observed during the reactor transient. However, the inclusion of the F810-SMA543 doublet collimator was not beneficial, shown previously by its attenuation as a function of wavelength in Figure 4-10. Following the March 2016 experiments (P-5), it was concluded that the Thorlabs collimator was ill-suited to transmit light at UV-low visible wavelengths. The Ocean Optics UV/COL-30 lens was purchased that possessed a very high transmission of UV light and is utilized for every test after P-5.

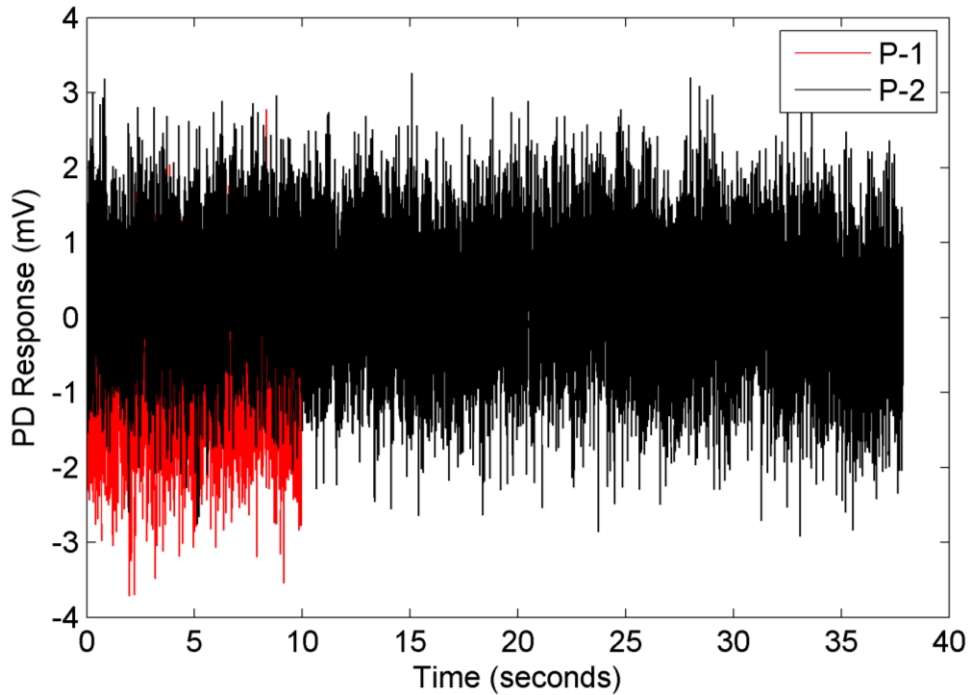


Figure 12-6. Comparison of P-1 and P-2 measurements

Initial pulse measurements at OSTR exhibited a behavior characteristic of a transient, but as discussed previously, errors in the implementation of NI LabVIEW software prevented the accurate characterization of the OSTR pulse shape due to a much smaller sample rate. Figure 12-7 through Figure 12-9 depict pulse measurements with the CRANK system that provided a distinct observation of a reactor pulse but at a limited sample rate, with the individual data points highlighted with asterisks. The PD response curves are plotted with the peak occurring at $t = 0$ per the FN model [98].

Since the CRANK system methodology relies on integration of the pulse to determine the β/l ratio, it is difficult to obtain accurate measurements without an adequate sample rate. The determination of β/l ratio and associated uncertainty as a function of sample rate was shown previously in Figure 6-29. Figure 12-7 through Figure 12-9 depicts OSTR measurements with a sample rate on the order of 10^2 Hz, which severely limits the ability of the CRANK system for its intended purpose.

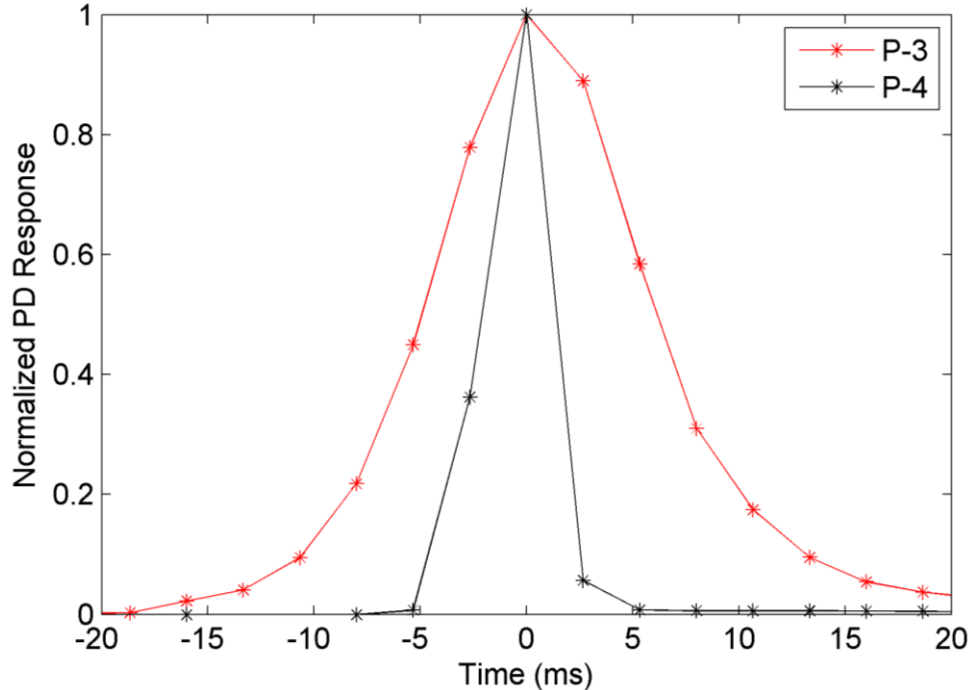


Figure 12-7. Comparison of P-3 and P-4 measurements

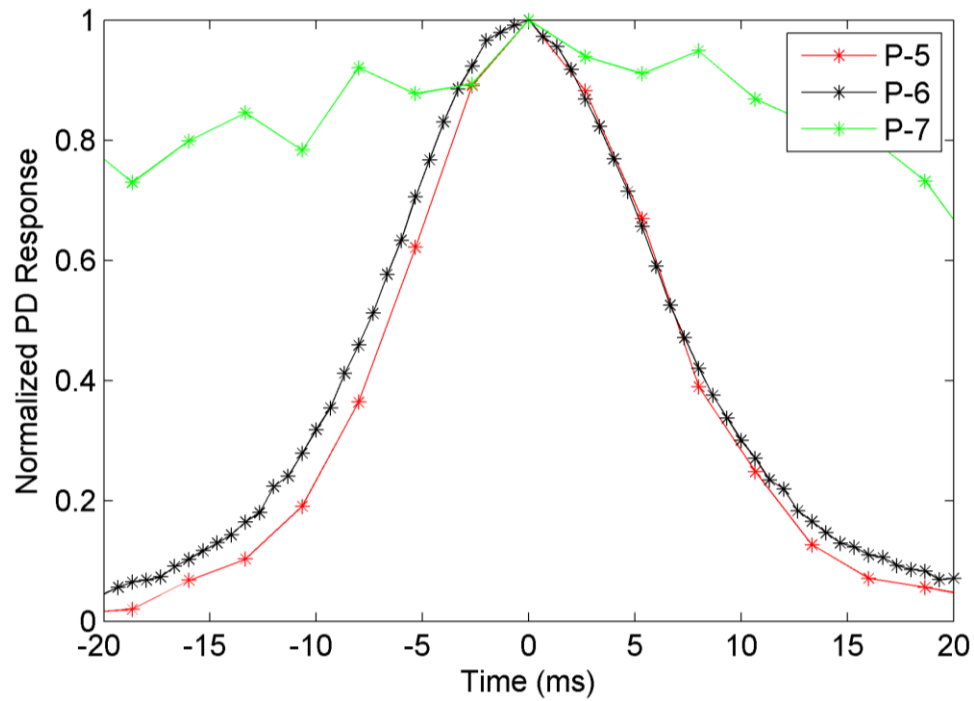


Figure 12-8. Comparison of P-5, P-6, and P-7 measurements

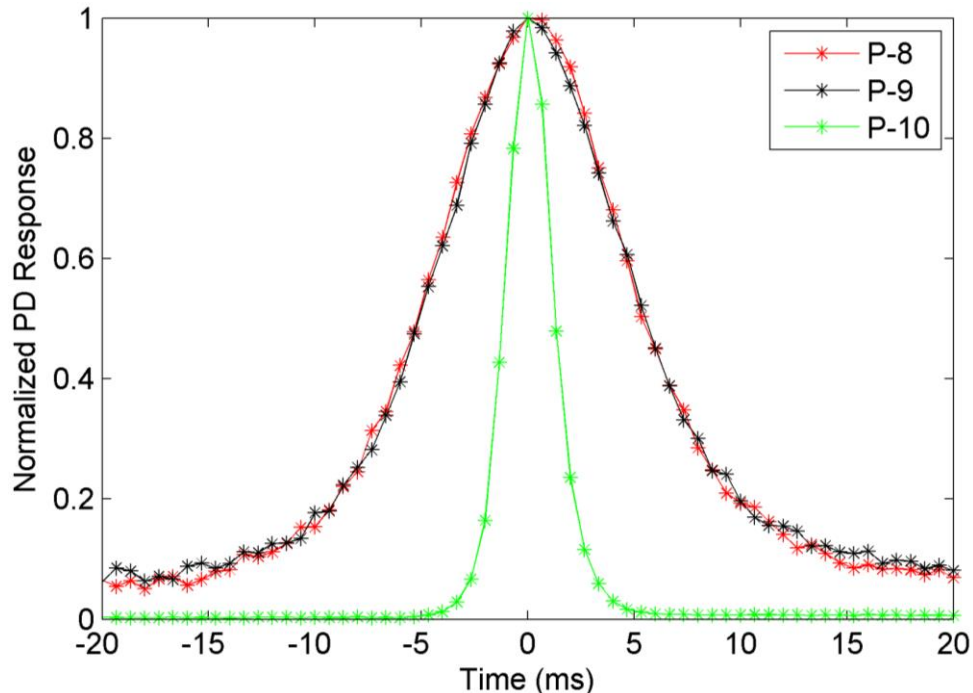


Figure 12-9. Comparison of P-8, P-9, and P-10 measurements

Changes made to the LabVIEW software used for data acquisition after September 2016 (P-10) allowed for the photodiode signal to be sampled at 250 MHz, shown in the vastly greater number of data points in the pulses. The initial approaches of the CRANK system methodology attempted to ascertain the first or second derivative of reactor power with respect to time, described previously in Section 3.2.3. Therefore, it was not necessary to obtain the entire pulse shape during an OSTR transient. However, as the CRANK methodology matured, it became necessary to obtain data over the entire reactor pulse for complete numerical integration. As a result, despite the larger S/N ratio exhibited in Figure 12-10 and Figure 12-11, these OSTR measurements were not utilized in the determination of the β/l ratio in Section 6.2.2. In particular, Figure 12-11 provides measurements for P-14, P-15, P-16, and P-17 in which the maximum voltage in the NI PXIe-5171R digital oscilloscope was exceeded, causing a flat voltage response near the region of maximum reactor power.

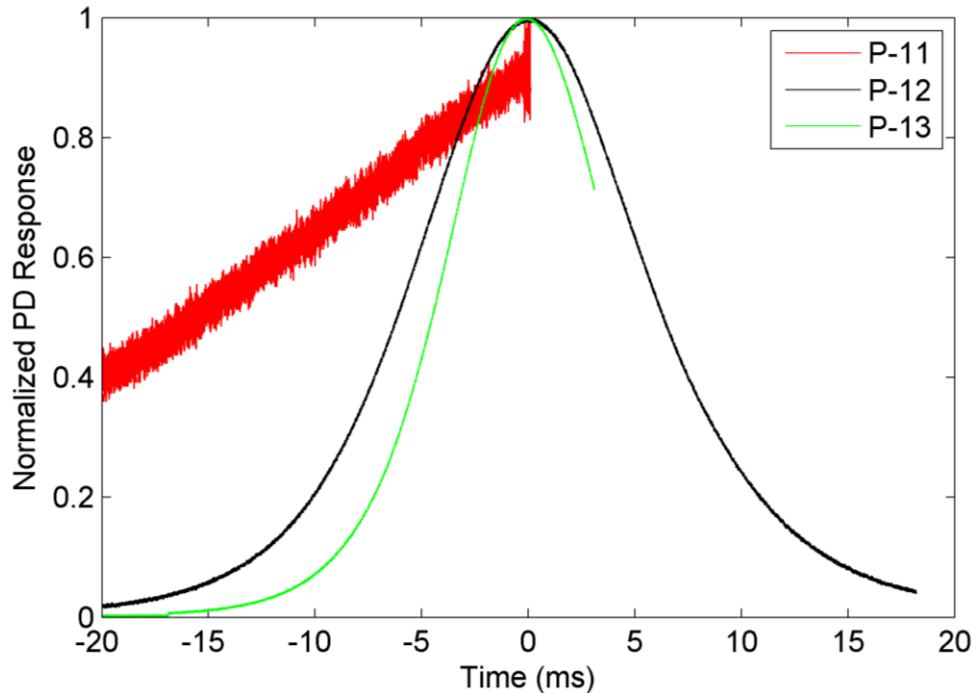


Figure 12-10. Comparison of P-11, P-12, and P-13 measurements

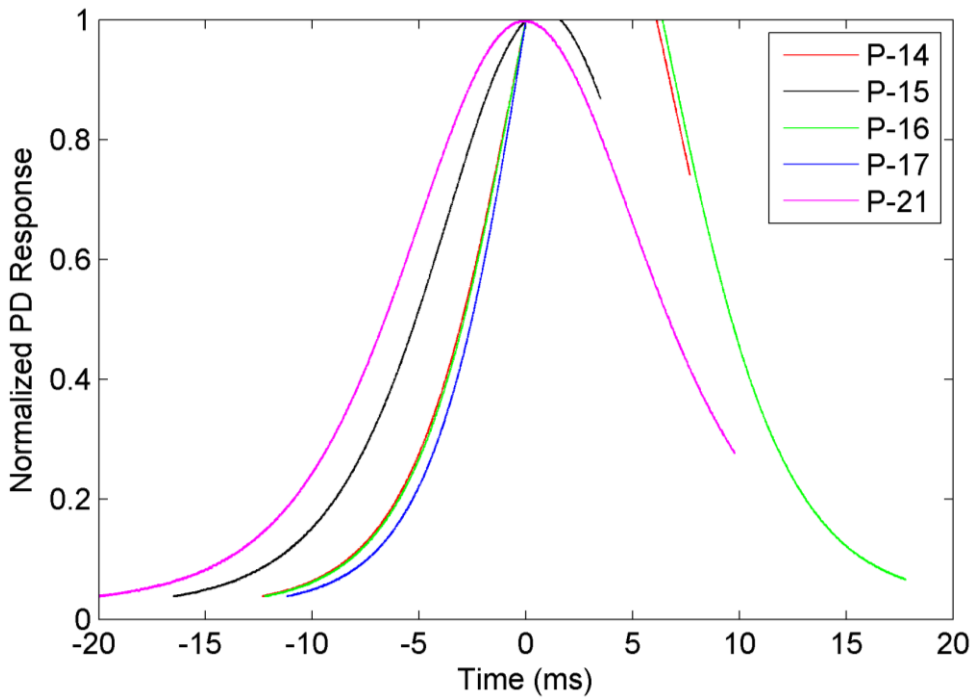


Figure 12-11. Comparison of P-14, P-15, P-16, P-17, and P-21 measurements

Prior to the realization of the finalized CRANK system methodology utilizing the integration of the reactor pulse, it was anticipated that a curve fit will provide an experimenter the ability to determine the reactor kinetics from experimental data. Recall the FN model provided in (3-24). If the FN model is used, it is necessary to determine the portion of the photodiode response to fit to the anticipated pulse shape hypothesized by the FN model. Figure 12-12 attempts to curve fit the data from P-13 by choosing a “time range” centered on the pulse peak to obtain the β/l ratio. As can be observed from Figure 12-12, the experimental measurement only matches the FN model in a single point, and this specified time cannot be determined analytically, preventing its use in determination of reactor kinetics.

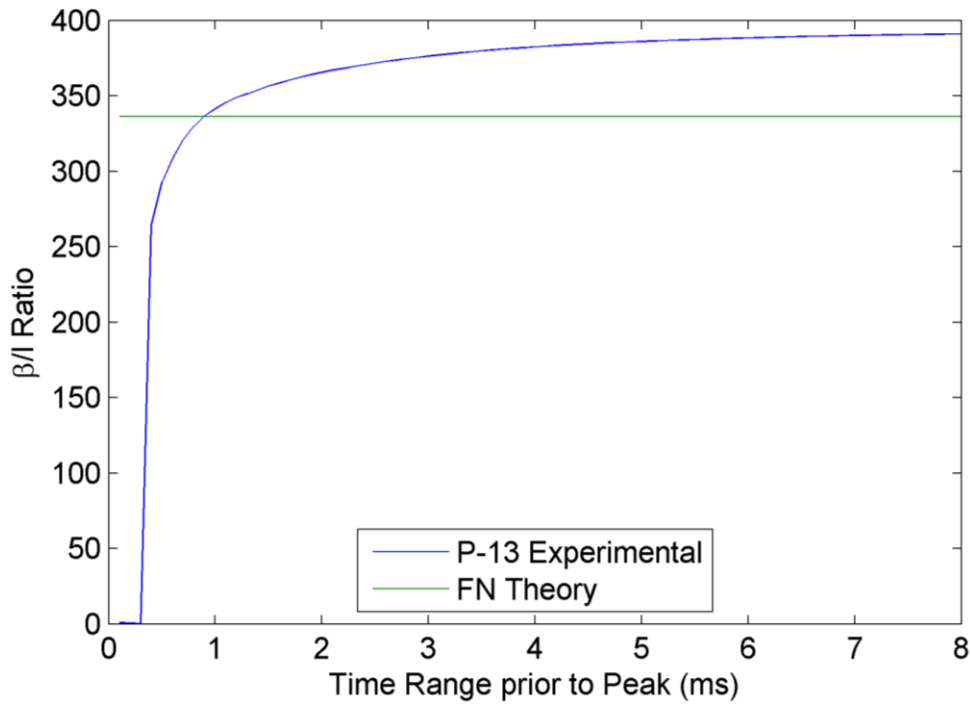


Figure 12-12. β/l ratio measurement using FN model

Similarly, Figure 12-13 attempts to curve fit Cherenkov data from P-13 with the FN model by utilizing a 2nd order polynomial using a Maclaurin series expansion of the FN model about the peak. Figure 12-13 shows that there are two instances in time when this approximation yields the correct value for the β/l ratio, though this cannot

be determined analytically either, preventing its use as part of the CRANK methodology.

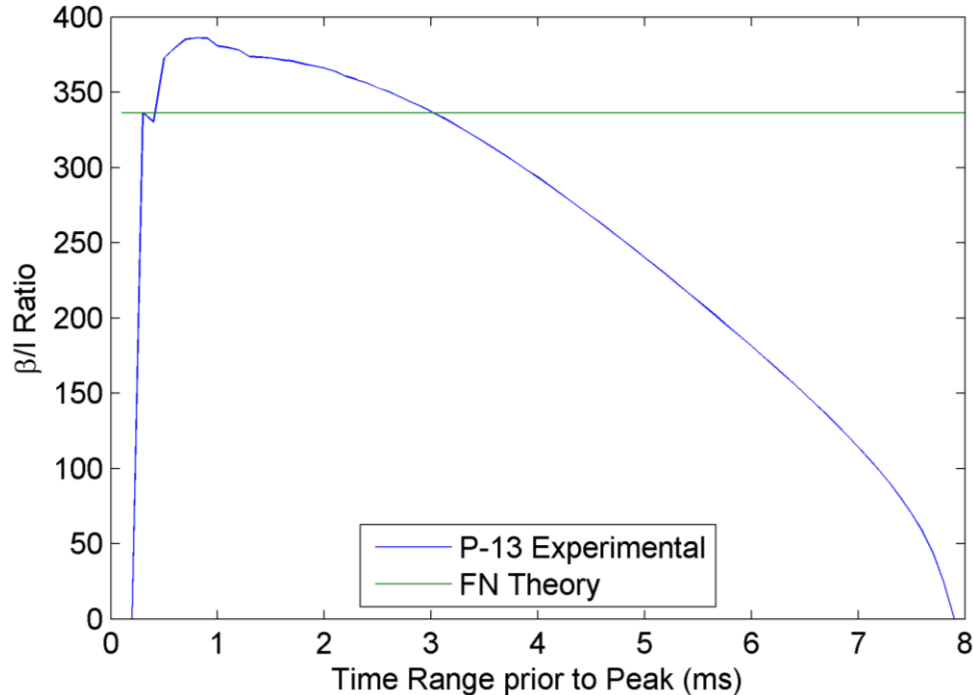


Figure 12-13. β/I ratio measurement using 2nd order polynomial

Once again, recall the methods discussed in Section 3.2.3. From the FN model, it is predicted that the initial derivative (at $t = 0$) reflects the reactivity inserted and the β/I ratio; however, there are two phenomena that negate this argument. The FN model assumes a constant temperature feedback, and the reactivity insertion is not a step change, but rather a ramp insertion. Figure 12-14 attempts to utilize P-12 and P-13 to determine the first derivative of the measured Cherenkov light and compare the results with the first derivative of the theoretical FN model. As can be observed from Figure 12-14, the Cherenkov light data at \$2.00 (P-13) do not accurately reflect the predictions based on the FN model. In fact, the measured slope of the pulse is greater than the predicted slope at the initiation of the reactor pulse, indicating that at the first detectable light intensity during pulses, the transient control rod is still being ejected from the core. At the beginning of each curve, the slope should indicate a value that

reflects $(-\lambda)^* \beta/l$ which corresponds to ~ 330 for \$2.00 (P-13) and ~ 250 for \$1.75 (P-12). Observing the logarithmic derivative curves in Figure 12-14, it is clear that the Cherenkov experimental data from the OSTR do not accurately reflect the predicted values from the FN model, and therefore, it is unlikely that measuring the initial slope will provide an accurate indication of the reactor kinetics. In fact, due to the high acquisition rate of 250 MHz, differentiation is not ideal. Noise can occur due to the discharge of the amplifier in the photodiode circuit, and differentiation acts as a high pass filter, allowing the noise to dominate the overall signal when observing the derivative or second derivative.

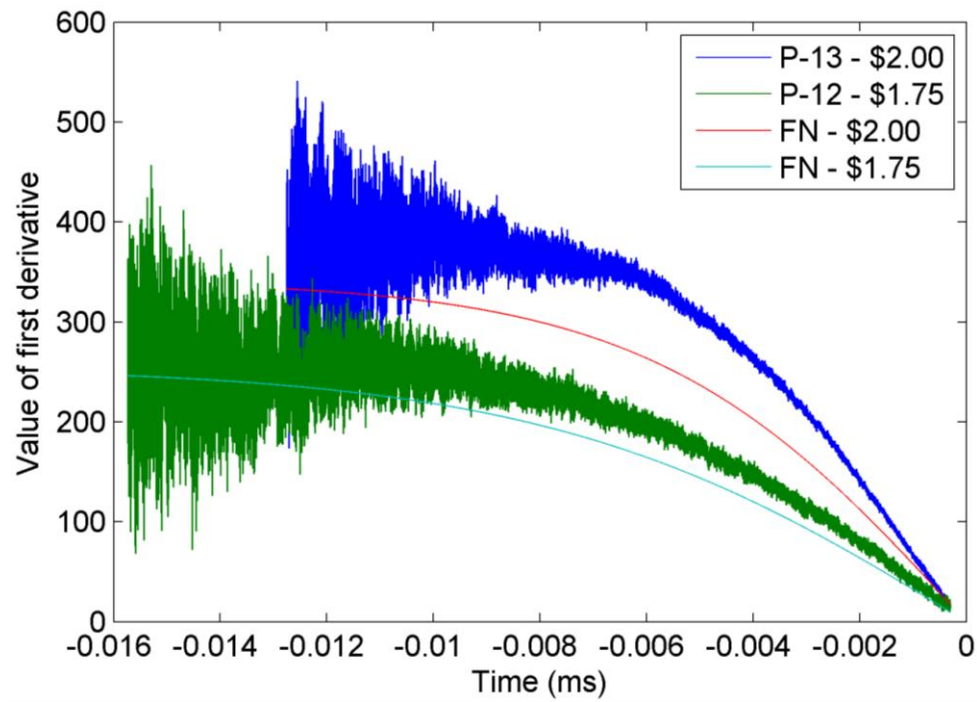


Figure 12-14. First derivative of P-12, P-13, and FN models

Finally, the NI LabVIEW software that was used for the duration of the OSTR experiments went through several revisions to accommodate necessary requirements for pulse analysis using the CRANK system. The final version of the LabVIEW software was very simple, utilizing the NI PXIe-5171R's internal FPGA to acquire data at 250 MHz for a maximum of 40 milliseconds to avoid memory overflow

issues. The measurement time was a variable set by the user up to the maximum of 40 milliseconds following a voltage threshold, also set by the user. The voltage threshold acts like a trigger, preventing data from being recorded until the trigger threshold had been exceeded. In most cases, the pulse peak recorded by the Thorlabs PDA25K photodiode was on the order of volts, so the threshold voltage was often set as low as 25 mV, just above the voltage measured as a result of background noise. Figure 12-15 and Figure 12-16 present the final revision of the LabVIEW block diagram and front panel, respectively.

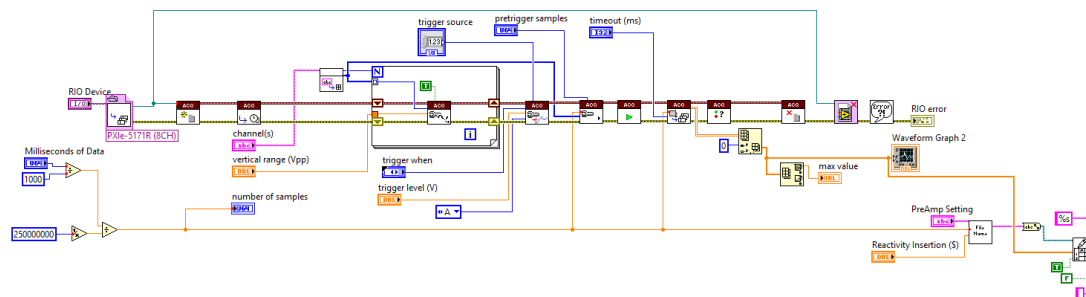


Figure 12-15. Block diagram of NI LabVIEW VI used for OSTR experiments

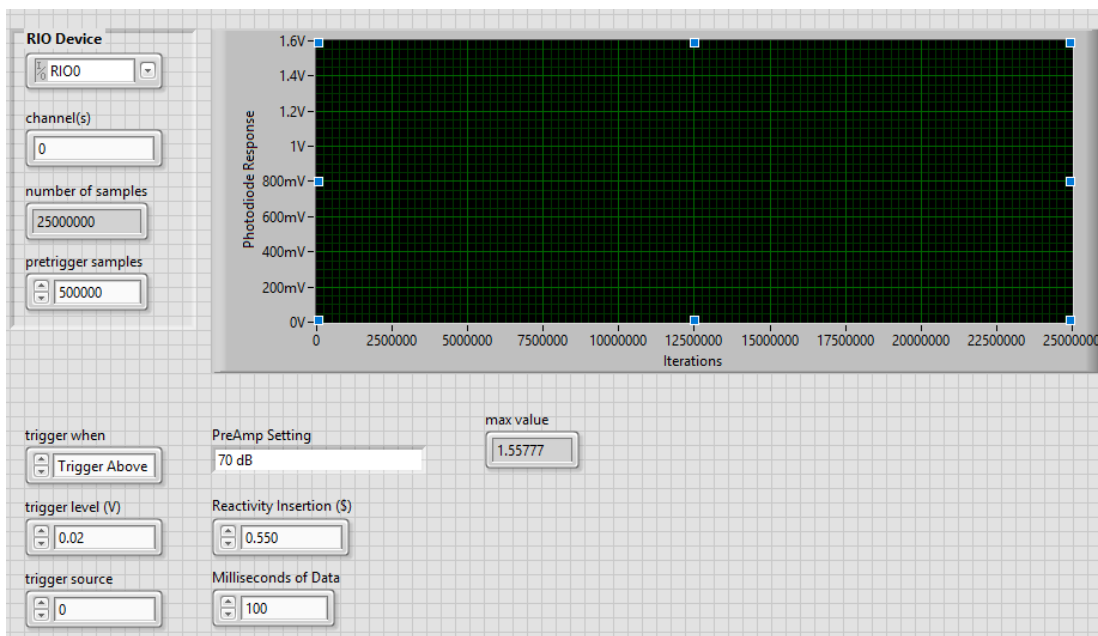


Figure 12-16. Front panel of NI LabVIEW VI used for OSTR Experiments

13 APPENDIX C – SENSITIVITY ANALYSIS

13.1 β/l Ratio

The proposed calculation in (13-3) is dependent on the integral and dollar value of each reactivity insertion. The uncertainty in the β/l ratio is dependent on the integrated area under each curve as well as the dollar value of prompt reactivity insertion. The method of integration proposed is the trapezoidal method, and there showed no discernible difference with a higher order integration scheme due to the number of data points collected at 250 MHz over the course of ~40 milliseconds. The individual uncertainty of each data point corresponds to the amplification gain of the PDA25K, shown in Table 4-4.

$$I = \int_0^\infty P(t)dt = \sum_i^{N-1} \left(\frac{P_{i+1} + P_i}{2} \right) \Delta t \quad (13-1)$$

$$\sigma_I^2 = \left(\frac{\partial I}{\partial P_1} \sigma_{P_1} \right)^2 + \left(\frac{\partial I}{\partial P_2} \sigma_{P_2} \right)^2 + \left(\frac{\partial I}{\partial P_3} \sigma_{P_3} \right)^2 + \dots + \left(\frac{\partial I}{\partial P_{N-1}} \sigma_{P_{N-1}} \right)^2 + \left(\frac{\partial I}{\partial \Delta t} \sigma_{\Delta t} \right)^2 \quad (13-2)$$

The uncertainty in the sample rate ($\sigma_{\Delta t}$) is found in the NI PXIE-5171R product specifications, and combines the oscilloscope's internal clock declared values for jitter (1 percent) and accuracy (4 percent), for a value of $\sigma_{\Delta t} = 4.123e-13$ sec. If the uncertainty in each data point is equivalent, the uncertainty in the integral (summation) of Cherenkov light for N points, equivalent to reactor power, is shown in (13-3) with $\Delta t = 4e-9$ sec (1/(250 MHz)) and σ_P corresponding to Table 4-4.

$$\sigma_I = \left((N\sigma_P\Delta t)^2 + \left(\frac{I}{\Delta t} \sigma_{\Delta t} \right)^2 \right)^{1/2} \quad (13-3)$$

Now, the uncertainty in the β/l ratio may be calculated based on its partial derivatives from (3-35).

$$\frac{\partial \beta/l}{\partial \$_1} = \frac{3I_2(\$_2-1)^2(\$_1-1)^2 - I_2(\$_2-1)^4 - 2I_1(\$_2-1)(\$_1-1)^3}{I_1I_2(\$_1-1)^2((\$_2-1)^2 - (\$_1-1)^2)} \quad (13-4)$$

$$\frac{\partial \beta/l}{\partial \$_2} = \frac{3I_1(\$_1-1)^2(\$_2-1)^2 - I_1(\$_1-1)^4 - 2I_2(\$_1-1)(\$_2-1)^3}{I_1I_2(\$_2-1)^2((\$_2-1)^2 - (\$_1-1)^2)} \quad (13-5)$$

$$\frac{\partial \beta/l}{\partial I_1} = \frac{-2(\$_2-1)^3}{I_1^2(\$_2-1)(\$_1-1)((\$_2-1)^2 - (\$_1-1)^2)} \quad (13-6)$$

$$\frac{\partial \beta/l}{\partial I_2} = \frac{2(\$_1-1)^3}{I_2^2(\$_2-1)(\$_1-1)((\$_2-1)^2 - (\$_1-1)^2)} \quad (13-7)$$

The uncertainty in the β/l ratio may be then calculated using the Taylor error propagation method (13-8).

$$\sigma_{\beta/l} = \left(\left(\frac{\partial \beta/l}{\partial \$_1} \sigma_{\$_1} \right)^2 + \left(\frac{\partial \beta/l}{\partial \$_2} \sigma_{\$_2} \right)^2 + \left(\frac{\partial \beta/l}{\partial I_1} \sigma_{I_1} \right)^2 + \left(\frac{\partial \beta/l}{\partial I_2} \sigma_{I_2} \right)^2 \right)^{1/2} \quad (13-8)$$

Based on rod worth values provided by the OSTR staff, reactivity insertions are performed based on percentage of full rod withdrawal height in increments of 0.1 inch. A distance of 0.1 inch is approximately equal to \$0.003, so this is the value assigned to $\sigma_{\$}$ when computing the uncertainty associated with the β/l ratio.

13.2 Proliferation Resistance

In Section 7.1, the potential for material diversion is assessed based on a case study of the OSTR experiments using the data with the lowest quantified uncertainty acquired with the CRANK system (P-29 and P-30). The lower limit of detection based on the CRANK methodology is dependent on the reactivity insertion values, the instrumentation uncertainty, and the mathematical sensitivity to the expressions used. In the case of material diversion, the instrumentation uncertainty and reactivity insertion uncertainty are previously described in Section 13.1. However, the

mathematical uncertainty with regards to H is yet to be addressed. Through a manipulation of (3-33), it is possible to ascertain the value of H in (13-9).

$$H = \left(\frac{2l}{\beta I(\$-1)} - 1 \right) \frac{1}{(\$-1)^2} \quad (13-9)$$

H is dependent on four independent variables, so the uncertainty in H is calculated through (13-10) with the associated partial derivatives in (13-11) through (13-14) with the Taylor error propagation method. The calculated uncertainty in H is then used to obtain a maximum deviation using $(H + 2\sigma_H)$ to determine a value of the detectable fraction of the β/l ratio in (7-7).

$$\sigma_H = \left(\left(\frac{\partial H}{\partial I_1} \sigma_{I_1} \right)^2 + \left(\frac{\partial H}{\partial I_2} \sigma_{I_2} \right)^2 + \left(\frac{\partial H}{\partial \$_1} \sigma_{\$_1} \right)^2 + \left(\frac{\partial H}{\partial \$_2} \sigma_{\$_2} \right)^2 \right)^{1/2} \quad (13-10)$$

$$\frac{\partial H}{\partial I_1} = \frac{I_2 (\$_1 - 1)(\$_2 - 1) \left[(\$_2 - 1)^2 - (\$_1 - 1)^2 \right]}{\left(I_1 (\$_1 - 1)^3 - I_2 (\$_2 - 1)^3 \right)^2} \quad (13-11)$$

$$\frac{\partial H}{\partial I_2} = \frac{I_1 (\$_1 - 1)(\$_2 - 1) \left[(\$_2 - 1)^2 - (\$_1 - 1)^2 \right]}{\left(I_1 (\$_1 - 1)^3 - I_2 (\$_2 - 1)^3 \right)^2} \quad (13-12)$$

$$\frac{\partial H}{\partial \$_1} = \frac{2I_1^2 (\$_1 - 1)^3 - 3I_1 I_2 (\$_1 - 1)^2 (\$_2 - 1) + I_1 I_2 (\$_2 - 1)^3}{\left(I_1 (\$_1 - 1)^3 - I_2 (\$_2 - 1)^3 \right)^2} \quad (13-13)$$

$$\frac{\partial H}{\partial \$_2} = \frac{2I_2^2 (\$_2 - 1)^3 - 3I_1 I_2 (\$_1 - 1)(\$_2 - 1)^2 + I_1 I_2 (\$_1 - 1)^3}{\left(I_1 (\$_1 - 1)^3 - I_2 (\$_2 - 1)^3 \right)^2} \quad (13-14)$$